Numerical and Experimental Study of Performance Improvement of a Microwave-Excited Microplasma Thruster Designed for Small Spacecraft

Takeshi Takahashi

2011

Abstract

Research and development of small-scale spacecraft (microspacecraft, 10 – 100 kg of mass) have recently attracted increasing attention in space technology. The advantages of microspacecraft can open the door for universities and small companies to utilize space environment. In recent years, a number of microspacecraft developed by universities have been started missions. They are launched as piggybacks of middle or heavy class launch vehicles (such as H-IIA), accompanying with main spacecraft.

Micro- or nanospacecraft whose mass is 10 – 30 kg, being in the similar class of the piggyback satellites, have a lot of mission potentialities when propulsion systems are implemented. We have developed an arcjet-type micro plasma thruster using azimuthally symmetric microwave-excited microplasmasconsisting of a microplasma source and a micronozzle. The thruster developed consisted of a microplasma source 1.5 mm in diameter and 10 mm long with a rod antenna on axis, and a converging-diverging micronozzle 1 mm long with a throat 0.2 mm in diameter. Previously developed microplasma thruster successfully demonstrated plasma generation in a mm-class small space, and measured the thrust of $\sim$ 1 mN, corresponding the specific impulse of $\sim$ 70 s with argon propellant. The thrust performance, especially the specific impulse is relatively low for electric propulsion system, and the advantage over micro chemical propulsion is not sufficient considering the power supply. To improve the performance, further investigation of the microplasma characteristics and micronozzle flow is needed. We focused on the propellant gas and the microwave frequency that affects the thrust performance significantly.

Firstly, plasma and aerodynamic features have been investigated numerically and experimentally for a microplasma thruster of electrothermal type using azimuthally symmetric microwave-excited microplasmas. Numerical analysis was made for the plasma and flow properties by developing a self-consistent two-dimensional model. In experiments, optical emission spectroscopy (OES) was employed with a small amount of additive gases of H_2 and N_2, to measure the plasma electron density and gas temperature. The thrust performance was also measured by using a micro thrust stand with a combination of target and pendulum methods. The electron density, gas temperature, thrust, and specific impulse were measured to be $n_e \approx (3-12)\times 10^{19}$ m^{-3}, $T_g \approx 700-1000$ K, $F_t \approx 0.2-1.4$ mN, and $I_{sp} \approx 50-80$ s, respectively, being consistent with those of numerical analysis.

Then, a microplasma thruster of electrothermal type has been investigated with feed or propellant gases of He and H_2, to achieve higher specific impulse. In the case of He propellant,The electron density, gas temperature, thrust, and specific impulse were measured to be $n_e \approx (2-5)\times 10^{19}$ m^{-3}, $T_g \approx T_{rot} \approx 600-700$ K, $F_t \approx 0.04-0.51$ mN, and $I_{sp} \approx 150-270$ s. Similar plasma characteristics and thrust performance were obtained with H_2 propellant, where the specific impulse I_{sp} ($\leq$ 450 s) was more than 1.5 times higher than that with He, owing to a difference in mass between He and H_2. A comparison with previous studies with Ar propellant indicated that in the presence as well as absence of plasma discharge, the specific impulse was enhanced by more than 3 – 5 times with light-mass propellants He and H_2, as has been known for large-scale propulsion systems.

Finally, an 11-GHz (X-band) microwave-excited microplasma source has been employed instead of 4.0-GHz (S-band) in previous works, and an investigation of the plasma characteristics and the thrust performance has been carried out, for the potentialities of more compact design and higher performance. Since X-band microwave-excited microplasma is a novel frontier for plasma science and technology field, we have focused on the fundamental characteristics of X-band microplasma, as well as an application to microplasma thruster. The newly de-

signed X-band microplasma source succeeded to generate plasma discharge with Ar propellant gas. From the results of OES, the Ar II (Ar^+) spectral lines were observed unlike the S-band microplasma, indicating the presence of electrons that have high enough energy to excite Ar^+ ions. The electron density, gas temperature, thrust and specific impulse of X-band microplasma thruster were measured to be $n_e \approx (4 - 14) \times 10^{19}$ m^{-3}, $T_g \approx 700 - 1100$ K, $F_t \approx 0.2 - 1.8$ mN and $I_{sp} \approx 60 - 90$ s, being significantly higher than those of S-band microplasma, as numerically predicted. Thus, 11-GHz microwaves were confirmed to bring potentialities of supporting more compact design and higher performance at the same time.

Throughout this thesis, we have shown the direction for a performance improvement of microwave-excited microplasma thrusters. Although a further miniaturization is very challenging because of the viscous loss in the micronozzle, a microplasma thruster will be a promising candidate for station-keeping and attitude control of micro- and nanospacecraft.

Acknowledgments

I would like to express my special thanks to everyone who has helped this work during my stay since April 2005, at the Propulsion Engineering Laboratory (Ono Lab.), Department of Aeronautics and Astronautics, Graduate School of Engineering, Kyoto University.

First, I would like to thank my supervisor, Prof. Kouichi Ono sincerely for providing me this opportunity to study as a Ph. D candidate of his laboratory. His insight, knowledge, encouragement and assistance have been very precious for me throughout my undergraduate, master and Ph. D course.

My gratitude also goes to Prof. Kazuo Aoki and Prof. Takaji Inamuro for careful reviewing this thesis and valuable comments and advices, and to Associate Professor Dr. Koji Eriguchi, Assistant Professor Dr. Yoshinori Takao, and Ex-Assistant Professor Dr. Hiroaki Ohta for for elaborated advice and discussion from practical viewpoint.

I would like to thank Dr. Yugo Osano, Mr. Keisuke Nakamura, Mr. Hiroshi Fukumoto, Mr. Masayuki Kamei, Mr. Shoki Irie, Mr. Taro Suzumura, Mr. Daisuke Hamada, Mr. Yugo Ichida, Mr. Yoshinori Nakakubo, Mr. Takumi Saegusa, Mr. Hirotaka Tsuda, Mr. Asahiko Matsuda, Mr. Shunsuke Kitanishi, Mr. Tetsuo Kawanabe and all of current and former members of Propulsion Engineering Laboratory, for encouragement, friendship, valuable discussion and cooperation throughout this work.

This work has been supported in part by a Grant-in-Aid for Scientific Research from the Ministry of Education, Culture, Sports, Science and Technology, Japan.

I would also like to thank all of my friends, especially Mr. Takahiro Seto, Mr.

Taikei Araki, Dr. Ryo Harada, Mr. Takeshi Kuboki, and Mr. Hitoshi Kominami as indispensable fellows throughout my nine-years campus life at Kyoto University, giving a lot of valuable advice and pleasant refreshing.

Finally, I would like to thank my family for all of encouragement, support and understanding.

Contents

Nomenclature

Roman Symbols

A	area
a_0	Bohr radius
$\boldsymbol{B}$	magnetic field
c	speed of light
D	diffusion coefficient
d	diameter
$\boldsymbol{E}$	electric field
$\mathcal{E}$	energy
e	magnitude of electron charge
$\boldsymbol{F}$	force
f	frequency
F_t	thrust
g	acceleration of gravity
I_{sp}	specific impulse
j	imaginary unit
$\boldsymbol{j}$	current density
k_B	Boltzmann constant
L	length
M	atomic weight
m	mass
n	number density
P	power
p	pressure
Q	power density
$\boldsymbol{q}$	heat flux
R	radius, universal gas constant
r	radius
T	temperature

t	time
u	axial velocity
$\boldsymbol{u}, \boldsymbol{v}$	velocity
V	volume
z	axial length

Greek Symbols

α	atomic polarizability
Γ	Flux
γ	specific heat ratio
δ_{ij}	Kronecker delta
ϵ	electric permittivity, emissivity
ϵ_0	electric permittivity of vacuum
ϵ_r	relative electric permittivity
η	viscosity
η_t	thrust efficiency
θ	azimuth
κ	thermal conductivity
λ	wavelength
μ	reduced mass
μ_0	magnetic permeability of vacuum
ν	collision frequency
ρ	mass density
σ	Stefan-Boltzmann constant
τ	stress tensor
ω	angular frequency

Subscripts

a	ambipolar
abs	absorbed
an	antenna
c	characteristic, cutoff
cr	critical
d	dielectric
e	electron, exit
elas	elastic
ex	excitation

G	Gaussian
g	gas, ground state
h	heavy particle
i	ion
in	inlet, input
iz	ionization
L	Lorentzian
n	neutral
p	period, plasma
rad	radiation
s	source
th	throat
V	Voigt
*	metastable state

Chapter 1

Introduction

1.1 Small-scale spacecraft

1.1.1 Microspacecraft and their recent missions

Research and development of small-scale spacecraft (microspacecraft, 10 – 100 kg of mass) have recently attracted increasing attention in space technology. Minituarization of the spacecraft brings us a lot of advantages [1, 2]. First, launch costs will be reduced drastically, since the mass and volume of spacecraft is directly linked to required performance of launch vehicles. Second, simplifying the structure leads to short development periods, and this will be a remarkable benefit for scientific observation and engineering experiments on the orbit with up-to-date components.

Moreover, missions with formation-flight by several microspacecraft are considered, to reduce the mission risk and increase flexibility [3]. The entire mission is divided into several tasks and assigned to each spacecraft making up the fleet. Even if one of the fleet goes down, the remaining will be able to keep up fundamental system of the mission and wait for launch of replacing spacecraft.

These advantages of microspacecraft can open the door for universities and small companies to utilize space environment. In recent years, a number of microspacecraft developed by universities have been started missions (see Table 1.1). They are launched as piggybacks of middle or heavy class launch vehicles (such

as H-IIA), accompanying with main spacecraft. In developing piggyback satellites, the orbit and launch time are determined by the main spacecraft. Also, there are strict requirements to avoid mechanical and electromagnetic interefference to the main spacecraft. However, primarily because of the reasonable launch costs, piggyback-launched microspacecraft are becoming more and more popular as opportunities for space utilization in aerospace research community. Figure 1.1 shows photographic image of the piggyback satellites launched with Ibuki (GOSAT) in January 2009. Hitomi (PRISM) by The University of Tokyo [4] is one of these satellites, successfully operating extensive boom type telescopic camera and amateur-band communication. In May 2010, Shin-en (UNITEC-1) was launched as a piggyback of Akatsuki (PLANET-C) Venus Explorer. It became the first university-made spacecraft exited the gravitational sphere of the earth. Horyu 2 satellite by Kyushu Institute of Technology is planned to be launched in 2011, equipping experimental systems for 300-V high voltage power generation and space debris observation. Moreover, PROITERES satellite by Osaka Institute of Technology [10] is also planned to be launched in 2011. This satellite has micropropulsion system (pulsed plasma thruster; PPT) for active attitude control in orbit (detailed in the next section).

1.1.2 Further miniaturization

To fabricate these microspacecraft, the components must be drastically miniaturized compared with conventional spacecraft. The mission payloads, such as image sensors, processors, radio transmitters have become smaller, lower-power, and higher-performance, receiving great benefits of semiconductor microfabrication technology. Recently, the semiconductor technology is able to fabricate not only electronic devices, but also micro-scale mechanical systems, such as cantilevers, valves, gears, and so on. They are called “micro-electromechanical systems (MEMS)”, being hot and rapidly growing. With the MEMS technology, the problem that mechanical components inhibit the miniaturization will be resolved, and the features of microspacecraft will have a great advance. Researches

Table 1.1: Recently launched and planned university-developed microspacecraft.

Spacecraft name	Operator	Launched year	References
Hitomi (PRISM)	The University of Tokyo	2009	[4]
Kukai (STARS)	Kagawa University	2009	[5]
Raijin (SPRITE-SAT)	Tohoku University	2009	[6]
Kiseki (KKS-1)	Tokyo Metropolitan College of Industrial Technology	2009	
WASEDA-SAT2	Waseda University	2010	
Hayato (KSAT-1)	Kagoshima University	2010	[7]
Negai⋆"	Soka University	2010	[8]
Shin-en (UNITEC-1)	University Space Engineering Consortium	2010	[9]
Horyu 2	Kyushu Institute of Technology	Planned 2011	
PROITERES	Osaka Institute of Technology	Planned 2011	[10]

of further miniaturization of spacecraft, called "nanospacecraft (1 – 10 kg)" and "picospacecraft (< 1 kg)" are now in progress almost worldwide. A concept image of nanospacecraft using MEMS technology is shown in Fig. 1.2. At present, development of power systems and orbit/attitude control systems (gyros, reaction wheels and thrusters) are especially needed to realize these nano- or picospacecraft.

1.2 Electric propulsion systems

Most of these small spacecraft employ spin-stabilization and have no active attitude and orbit control system, such as reaction wheels and thrusters, because of severe mass and volume limitation. A reaction wheel consists of a rotating wheel and a motor, producing rotational torque by accelerating and decelerating of the wheel. Most of conventional spacecraft have three or more reaction wheels, using for everyday three-axis attitude control. Since the rotation speed of reaction wheels is limited, they need to be "unloaded" by using thrusters. Thrusters can also make translational acceleration or deceleration maneuvers to control orbits, and landing and take-off maneuvers. If these active control systems are established, the potentialities of small spacecraft missions are drastically extended. To develop thrusters for small spacecraft, there are several requirements, such as simple and light structure, low power consumption, easy-to-handle (non-toxic) propellant, and high precision thrust control.

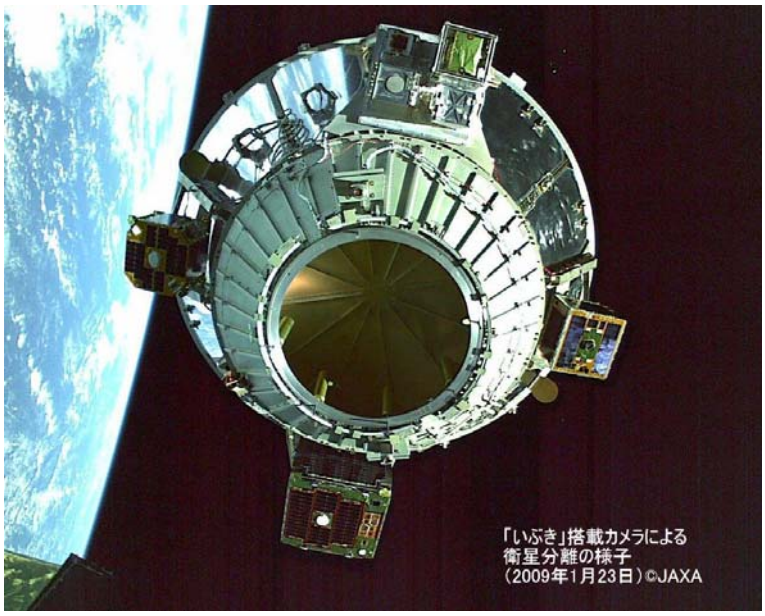

Figure 1.1: Piggyback microspacecraft, launched with Ibuki (GOSAT). Copyright ©2009 Japan Aerospace Exploration Agency.

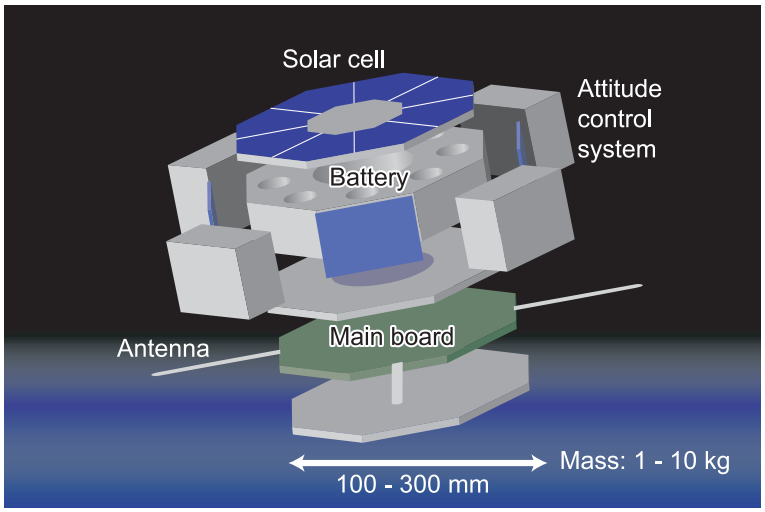

Figure 1.2: Concept image of a nanospacecraft.

Various microthrusters have been proposed for these applications [2, 12–15], including micro electric propulsion systems or micro plasma/ion thrusters [16, 18–29, 31–38] : direct current (DC) microarcjet thruster [16, 18, 19], DC microplasma thruster (MPD) [20, 21], micro Hall thruster [22, 23], micro ion thruster [24–27], and dielectric capillary discharge acceleration [31] using gas fuels; field emission electric propulsion (FEEP) [32] and colloid thruster [33] using liquid fuels; vacuum arc microthruster (VAμT) [34], micro laser-ablation plasma thruster (μ-LPT) [35, 36], micro pulsed plasma thruster (μ-PPT) [37, 38], and ferroelectric plasma thruster (FEPT) [28–30] using solid fuels. Figure 1.3 shows the positioning of chemical, electrothermal, electrostatic/electromagnetic propulsion by two key performance, specific impulse and thrust density. Specific impulse I_{sp} is defined by $F_t/\dot{m}g$, where F_t, m and g are thrust, propellant mass and acceleration of gravity. I_{sp} is an index of fuel efficiency, thus a propulsion system with high I_{sp} is able to obtain the same acceleration using little propellant. Thrust density is defined by F_t/A_e, where A_e is area of nozzle exit. For example, several electric propulsion systems and applications for small spacecraft are detailed in this section.

1.2.1 Resistojets

Resistojets are the simplest type of electric propulsion systems. As shown in Fig. 1.4, propellant gas is stored in gaseous or liquid phase, and heated up by electrically heated solid surface (ohmic heating of resistors), instead of combustion in chemical propulsion. Then, the heated gas flows through the nozzle, being accelerated from subsonic to supersonic aerodynamically, and produces thrust. The largest advantage of resistojets is high reliability owing to the simple structure. Since no combustion or discharge is needed, another advantage is that wide variety of propellant, especially non-toxic and non-flammable materials can be used. Major issues in development are the heat transfer from resistor to propellant and materials endure high temperature. Specific impulse I_{sp} is relatively low for electric propulsion, being 200 – 1000 s [11]. Studies about miniaturization

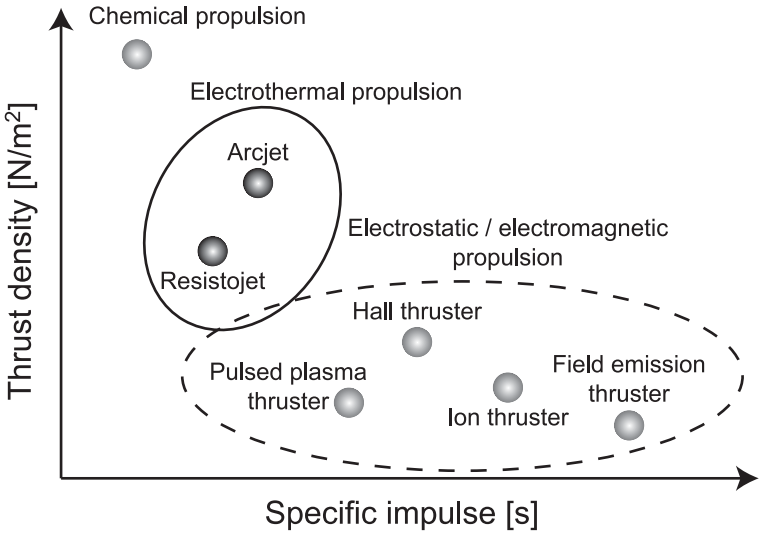

Figure 1.3: Positioning of chemical, electrothermal, electrostatic/electromagnetic propulsion by two key performance, specific impulse and thrust density. This thesis aimed at electrothermal propulsion, having intermediate characteristics.

of resistojets are started in 1990s [39], and MEMS-based type is presented recently [40, 41]. This MEMS-based microresistojet is called "Free-molecule microresistojet (FMMR)", operated at low pressure of 50 to 200 Pa. Since the Knudsen number is on the order of unity, the gas flow in heat exchanger is a molecular flow. The propellant molecules collide with the wall of heat exchanger and gain kinetic energy determined from the wall temperature, then exited from the thruster without another collision. Thus, thermal losses owing to heat conduction and viscous effect afflicting electrothermal thrusters are avoided.

1.2.2 Arcjets

In principle, performance of resistojets is limited by the upper temperature limit of heater materials. When gaseous discharges are used for heating instead of the heater, the temperature of propellant gas can reach much higher and produce better thrust performance. These thrusters are called "arcjets", because large-current arc discharges are generally employed. Figure 1.5 is the schematic of a

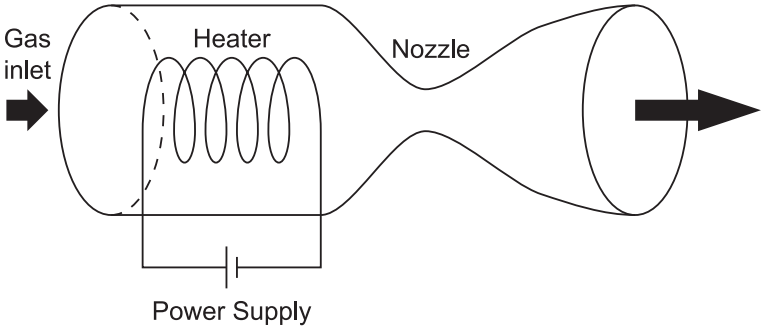

Figure 1.4: Schematic of a resistojet.

core-flow type arcjet thruster. The cathode and anode (thruster body) are placed coaxially, and the arc discharge column is sustained through the constrictor region. Arcjets have reliatively high flexibility for choice of propellants, especially in high-power operation. On the other hand, there are issues about electrode erosion and thruster cooling to be overcome through development of arcjets. Specific impulse is significantly higher than that of resistojets, being typically between 1000 and 2000 s [11]. Microarcjet thrusters are also studied for small spacecraft, mainly using direct current (dc) discharges [16–19]. In refs. [16, 17], a dc microarcjet thruster using nitrogen propellant is presented. An array of Sub-mm scale micronozzles is fabricated and plasma discharge is generated inside the nozzle. A significant improvement of thrust performance is confirmed with hot plasma operation compared with cold gas, being I_{sp} of $\approx$ 70 s.

1.2.3 Ion thrusters

Ion thrusters are known as the main engines of Hayabusa (MUSES-C) asteroid explorer, successfully returned to the earth with a sample from asteroid Itokawa in 2010. They are utilizing the characteristics of plasma, consisting of ions and electrons, more actively than electrothermal thrusters. The propellant gas is typically xenon, because of its small ionization energy. A plasma discharge ionized the propellant gas, then the ions are extracted by electric field between ion source and accelerating grid (electrode). In most of ion thrusters, three grids

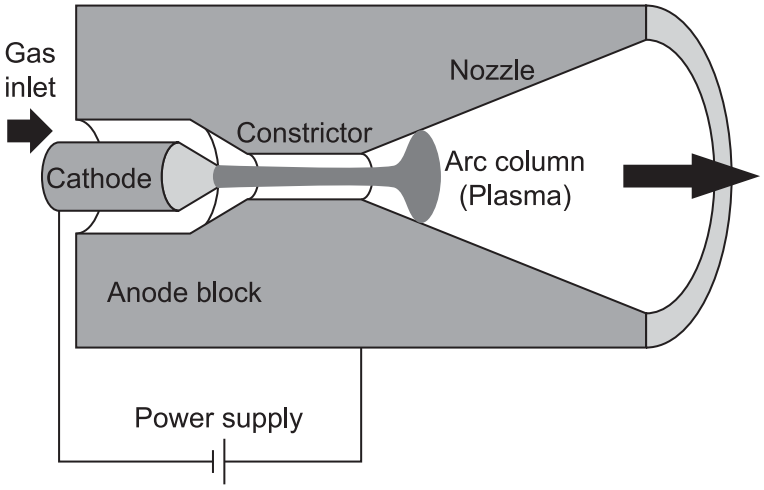

Figure 1.5: Schematic of an arcjet.

are placed at the end of thruster, screen, accelerating, and decelerating grid, respectively. The screen grid contributes focusing of ion beam, and the decelerating grid prevents electrons from flowing backward. The axial velocity of ions reaches 30 km/s typically, corresponding specific impulse of 3000 s. This is one of the greatest advantages of ion thruster. However, the maximum thrust is restricted by space-charge limitation, thus ion thrusters can produce less thrust than many other propulsion systems. Although there are a number of problems in miniaturization of ion thrusters, successful operations of micro ion thrusters are reported [24–27]. Paper [27] presented an 1-cm-diameter micro ion thruster, called "μ1". μ1 employed electron cyclotron resonance (ECR) plasma for the ion source, with low microwave power of <5 W. An ion beam extraction was successfully conducted, with low discharge losses.

1.2.4 Hall thrusters

Hall thrusters are also popular electric propulsion systems along with ion thrusters, utilizing electrostatic and electromagnetic acceleration. A cross-section schematic of a Hall thruster is shown in Fig. 1.7. In Hall thrusters, the discharge chamber is typically annular type and magnets are placed at the center axis and

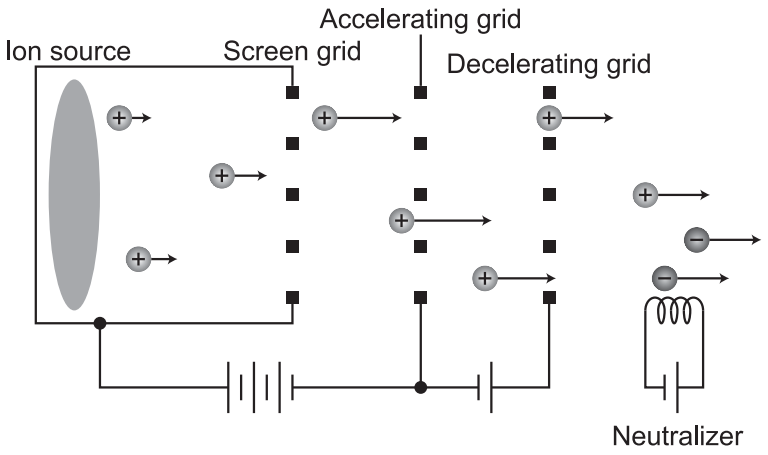

Figure 1.6: Schematic of an ion thruster.

external wall, to produce radial-directional magnetic field $\boldsymbol{B}$. Electrons emitted from the cathode (usually employed a hollow cathode) are attracted by the anode placed upstream and enter the chamber. However, owing to the presence of magnetic field $\boldsymbol{B}$, electrons gyrate along the magnetic field lines (cycrotron motion) and drift azimuthally ($\boldsymbol{E} \times \boldsymbol{B}$ drift). The propellant gas is ionized by collisions with the drifting electrons, and the ions are accelerated by the same electric field without being trapped by the magnetic field because of the large mass of ions. Since the discharge region is quasi-neutral, the extracted ion beam is free from space-charge limitation and Hall thrusters can achieve larger thrust density than ion thrusters. Miniaturization of Hall thrusters is also very challenging because of the need of strong magnetic field in small discharge region. However, a 4-mm diameter micro Hall thruster is succeeded to operate with 10 – 40 W power range [22, 23], being a promising propulsion system for microspacecraft.

1.2.5 Other advanced propulsion systems

In addition, many types of electric propulsion systems are proposed and under experiment, including pulsed plasma thruster (PPT) [37, 38] and ferroelectric plasma thruster (FEPT) using solid propellants [28–30], and field emission elec-

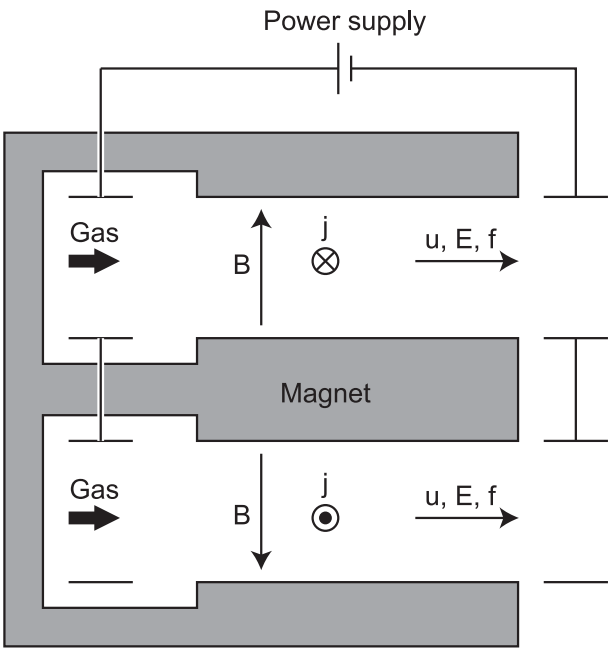

Figure 1.7: Schematic of a Hall thruster.

tric propulsion (FEEP) using liquid propellants [32]. Figure 1.8 shows a schematic of a PPT. Polytetrafluoroethylene (PTFE, Teflon®) is commonly used as the propellant, because its high handleability such as non-flammable and non-toxic. In addition, PPTs have advantages of simple structure and compact propellant storage. When a pulse discharge ignited between two electrodes, the propellant is sublimated and ionized instataneously. The generated plasma is accelerated by self-induced magnetic field and thermally expanded, then produce thrust (or impulse bit). In miniaturization of PPTs, the critical issue to be overcome is the power component such as the capacitor, rather than the thruster head itself. The research is actively in progress now, and recently PROITERES satellite by Osaka Institute of Technology employed micro-PPTs [10]. The launch of PROITERES is scheduled in 2011, this will be the first nanosatellite with active orbital and 3-axis attitude control by electric propulsion system.

Figure 1.9 shows a ferroelectric plasma thruster (FEPT) [28–30]. FEPTs are utilizing the peculiar electric characteristics of certain types of dielectrics, called

"ferroelectric" materials. Ferroelectric materials have a spontaneous and nonlinear electric polarization, that can be reversed by externally applied electric field. The surface of ferroelectric which is not covered with electrode attracts surface charge to compensate the internal charge. When a high-voltage rf power is applied between the two electrodes, the polarization of the ferroelectric is also changed quickly back and forth. The surface charges can not follow the polarization change, thus a local and instantaneous large electric field is generated and the ferroelectric itself is ionized and turned into plasma state. Both the ions and electrons are accelerated downstream by the ponderomotive force [28], thus FEPTs have an advantage of self-neutralization.

In addition, a field emission electric propulsion (FEEP) is presented as one type of the highest specific impulse propulsion systems [32]. Figure 1.10 shows schematic of a typical FEEP thruster. Metals with relatively low melting point, such as cesium and indium, are used for the propellant of FEEP thruster. First, heated and liquefied propellant metal is fed to the orifice by capillary action. At the orifice exit, the applied electric field between the anode (propellant tank or orifice itself) and the cathode ionizes the propellant. The produced ions are accelerated downstream by strong electric field without bombarding the cathode, and this is called "field emission". Since the emitted particles are only ions, the electrons need to be supplied by a neutralizer, as well as ion thrusters and Hall thrusters. Although there is a requirement of very high voltage ($\sim$ 10 kV), the specific impulse reaches 6000 – 10000 s. This high specific impulse will be significantly promising as a propulsion system for attitude control of microspacecraft.

1.3 Target, concept and direction

Micro- or nanospacecraft whose mass is 10 – 30 kg, being in the similar class of the piggyback satellites in Table 1.1, have a lot of mission potentialities when propulsion systems are implemented. Electrostatic and electromagnetic thrusters (ion thrusters, Hall thrusters, PPTs, FEPTs, and FEEPs) have a significant advan-

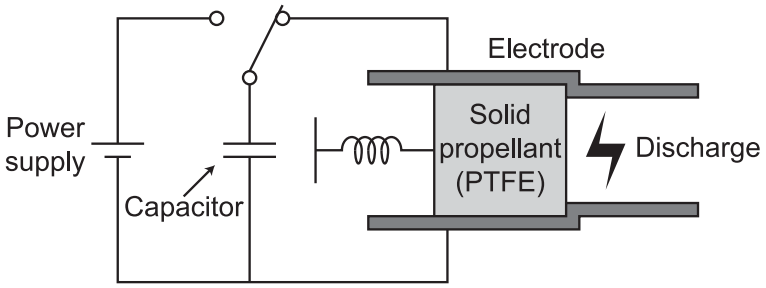

Figure 1.8: Schematic of a pulsed plasma thruster (PPT).

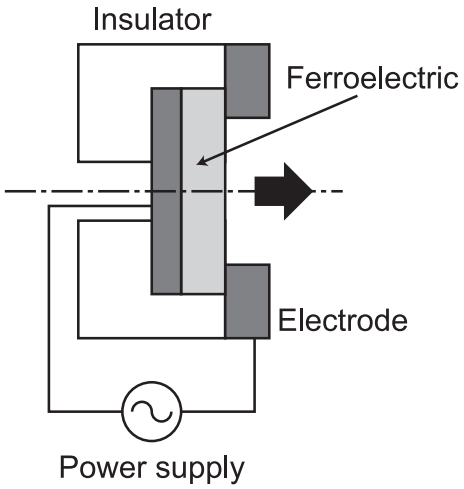

Figure 1.9: Schematic of a ferroelectric plasma thruster (FEPT).

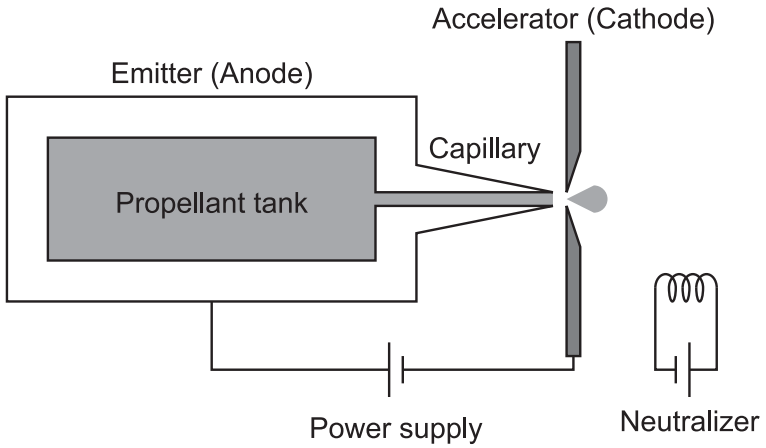

Figure 1.10: Schematic of a field emission electric propulsion (FEEP).

tage of high specific impulse that cannot be achieved by any chemical propulsion. On the other hand, the largest feature of chemical rockets is high thrust density, that is, they can produce large thrust from small nozzle. This advantage enables agile maneuvers such as single-impulse orbit insertion, and even landing and take-off. Electrothermal thrusters (resistojets and arcjets) have intermediate characteristics between electrostatic/electromagnetic thrusters and chemical rockets. Although the specific impulse is lower than electrostatic/electromagnetic thrusters, the thrust is estimated to be large enough for microspacecraft to control their orbits [42]. We have focused on an arcjet type (see section 1.2.2) microplasma thruster, targeting the thrust of 1 mN and specific impulse of 100 s.

In miniaturization of arcjet thrusters, the most significant issue to be resolved is plasma generation in small chamber. As the dimensions reduced similarly, the volume get small rapidly with cubic function of the length, while the surface area with square function. Thus, the effects (both positive and negative) of surface area become more dominant in smaller dimensions. From a viewpoint of arcjet plasma generation, this surface-to-volume ratio effect is a serious problem. The conductive and convective loss of thermal energy to the chamber walls causes lowering of the gas temperature and thrust performance, as well as increasing of the chamber wall temperature and concern of heat resistance. However, there are a plasma generation mechanism utilizing actively such a high surface-to-volume ratio. This is called “surface-wave excited plasma”. Injected microwaves penetrate into the plasma chamber along the plasma-dielectric interfaces even in the overdense mode, and so the electron heating occurs in a thin (a few millimeters deep or less) skin-depth layer; that is, most of the power is absorbed near the interfaces [49–52]. Such mechanism of the power deposition is a great advantage to generate plasmas in a limited space without magnetic-field confinement. Originally, surface-wave excited plasma sources are developed for plasma material processing in large diameter, establishing discharges relatively easily over a wide pressure range by surface waves excited around the dielectric envelope of the antenna on axis.

Taking this advantage of surface-wave excited plasmas, we have developed a microplasma thruster using azimuthally symmetric microwave-excited microplasmas in our laboratory [42–48], consisting of a microplasma source and a micronozzle as shown in Fig. 1.11. The microplasma source is made of a dielectric chamber ~ 1.5 mm in inner diameter and ~ 10 mm long covered with a metal grounded, having a metal rod antenna on axis covered with a dielectric envelope, which produces high temperature plasmas at around atmospheric pressures. The micronozzle concerned is a converging-diverging type (or Laval nozzle) ~ 1 mm in length, having a throat ~ 0.2 mm in diameter, which converts high thermal energy of plasmas into directional kinetic energy of supersonic plasma flows to obtain the thrust. The microwave power employed would be limited to < 10 W, taking into account the electric power generated by solar cell panels installed on the microspacecraft concerned.

Previously developed microplasma thruster successfully demonstrated plasma generation in a mm-class small space, and measured the thrust of ~ 1 mN, corresponding the specific impulse of ~ 70 s with argon propellant. The thrust performance, especially the specific impulse is relatively low for electric propulsion system, and the advantage over micro chemical propulsion is not sufficient considering the power supply. To improve the performance, there is a nesessity for further investigation of the microplasma characteristics and micronozzle flow, to obtain further findings about surface-wave excited microplasmas and microplasma thrusters as an application. We focused on the propellant gas and the microwave frequency that affects the thrust performance significantly.

1.4 Outline of the thesis

In Chap. 2, plasma and aerodynamic features have been investigated numerically and experimentally for a microplasma thruster of electrothermal type using azimuthally symmetric microwave-excited microplasmas. Numerical analysis was made for the plasma and flow properties by developing a self-consistent two-

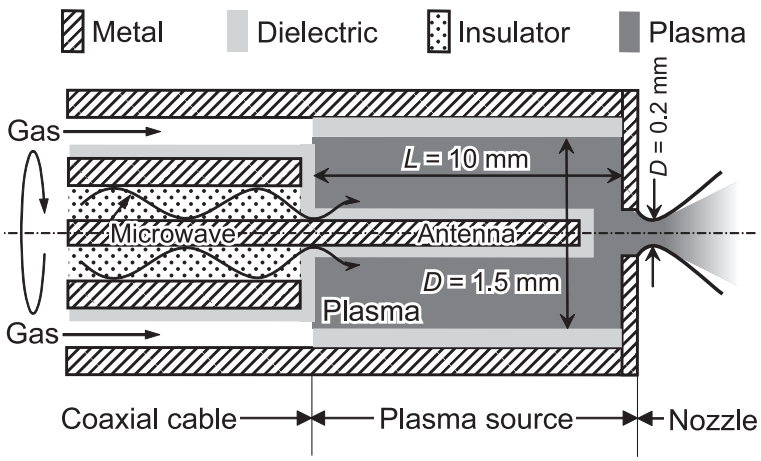

Figure 1.11: Schematic of the microplasma thruster using azimuthally symmetric microwave-excited microplasmas, consisting of a microplasma source with a rod antenna on axis and a converging-diverging (Laval) micronozzle.

dimensional model. In experiments, optical emission spectroscopy (OES) was employed with a small amount of additive gases of H_2 and N_2, to measure the plasma electron density and gas temperature. The thrust performance was also measured by using a micro thrust stand with a combination of target and pendulum methods.

In Chap. 3, a microplasma thruster of electrothermal type has been investigated with feed or propellant gases of He and H_2, to achieve higher specific impulse. Surface wave-excited plasmas were established by 4.0-GHz microwaves at powers of ≤ 6 W. The microplasma generation, micronozzle flow, and thrust performance with He was numerically analyzed by using a previously constructed model detailed in Chap. 2. In experiments, the plasma electron density and gas temperature was measured by OES, and the thrust performance was measured by micro thrust stand. A comparison with previous studies with Ar propellant (Chap. 2) indicated that in the presence as well as absence of plasma discharge, the specific impulse was enhanced by more than 3 – 5 times with light-mass propellants He and H_2, as has been known for large-scale propulsion systems. Thus, it follows that in the microplasma thruster of electrothermal type, the high diffusivity

and thermal conductivity of He and H_2 in the microplasma source of high surface-to-volume ratios do not lead to a deterioration of the thrust performance, primarily owing to a more significant thermal energy gain due to elastic collisions between electrons and heavy particles in He and H_2.

In Chap. 4, an 11-GHz (X-band) microwave-excited microplasma source has been employed instead of 4.0-GHz (S-band) in previous works, and an investigation of the plasma characteristics and the thrust performance has been carried out, for the potentialities of more compact design and higher performance. Since X-band microwave-excited microplasma is a novel frontier for plasma science and technology field, we have focused on the fundamental characteristics of X-band microplasma, as well as an application to microplasma thruster. The newly designed X-band microplasma source succeeded to generate plasma discharge with Ar propellant gas. From the results of OES, the Ar II (Ar^+) spectral lines were observed unlike the S-band microplasma, indicating the presence of electrons that have high enough energy to excite Ar^+ ions. The electron density, gas temperature and thrust performance of X-band microplasma were measured to be significantly higher than those of S-band microplasma, as numerically predicted.

Finally, Chap. 5 concludes the thesis and makes a remark for future work.

Chapter 2

Microplasma generation, micronozzle flow, and thrust performance

2.1 Introductory remarks

This section presents a numerical and experimental study of the micro plasma thruster presently developed, with emphasis being placed on a better understanding of distinguished characteristics of the microwave-excited microplasma and micronozzle flow. A self-consistent numerical model was newly developed over the entire region of interest through microplasma source to micronozzle, taking into account the electromagnetic wave propagation, plasma evolution, and gas/plasma flow evolution from subsonic to supersonic. The working gas of interest in this study was Ar, which is an engineering model for studying plasma and fluid physics in a micro plasma thruster. The numerical results were compared with the plasma density and gas temperature experimentally measured in the plasma source region by optical emission spectroscopy; a comparison was also made with the measurements of thrust performance.

2.2 Numerical analysis

2.2.1 Model

General

The numerical model consisted of an electromagnetic module (EM) for microwave propagation in interacting with plasmas and a fluid module (FM) for plasma flows with two (electron and heavy particle) temperatures. The former employed the finite difference time-domain (FDTD) approximation, being applied to the microplasma source, to analyze the microwave power absorbed in the plasma. The latter employed two-temperature fluid equations, being applied to the entire region through the plasma source to micronozzle, to analyze the plasma and nozzle flow characteristics. Gas-phase reaction processes were taken into account in both regions along with plasma-wall interactions in a limited space, and the analysis of the nozzle flow finally gave the thrust performance achieved. The numerical analysis relied on the azimuthally symmetric coordinate system [two-dimensional (2D) r-z system, $\partial/\partial\theta = 0$] assuming that:

1. the plasma is a two-phase medium consisting of electrons and heavy particles (ions and neutrals), and the temperature of electrons is different from that of heavy particles [$T_e \neq T_h (= T_i = T_n)$].

2. The plasma is macroscopically quasi-neutral, or the electron density equals that of ions ($n_e = n_i$).

3. The atomic processes in the gas phase are electron-impact excitation/de-excitation and ionization/recombination, taking into account metastable as well as ground-state atoms for neutrals.

4. The charged particles (ions and electrons) diffuse toward the walls according to the ambipolar diffusion.

5. The sheath structures are neglected at the plasma-wall interfaces.

6. The gas/plasma flow is laminar, and the convective velocity $\boldsymbol{v}$ is the same for all species (electrons and heavy particles).

7. In the microplasma source, moreover, the microwave energy is absorbed by plasma electrons, which in turn, is transferred to heavy particles through elastic collisions between them.

It should be noted here that this model takes into account the gas/plasma flow self-consistency over the entire region through the microplasma source to the micronozzle (or through subsonic to supersonic), while our previous model neglected the flow in the plasma source region [42, 46, 47].

Electromagnetic model module

The EM module for the microplasma source consists of Maxwell's equations for electromagnetic fields of microwaves and equations for plasma electrons (neglecting the Lorentz force and pressure gradient) [42, 51, 52]:

$$\nabla \times \boldsymbol{E} = -\frac{\partial \boldsymbol{B}}{\partial t}, \tag{2.1}$$

$$\nabla \times \boldsymbol{B} = \mu_0 \left(\boldsymbol{j} + \epsilon_\mathrm{r} \epsilon_0 \frac{\partial \boldsymbol{E}}{\partial t} \right), \tag{2.2}$$

$$m_\mathrm{e} \frac{\partial \boldsymbol{u}_\mathrm{e}}{\partial t} = -e\boldsymbol{E} - m_\mathrm{e} \nu_\mathrm{e} \boldsymbol{u}_\mathrm{e}, \tag{2.3}$$

$$\boldsymbol{j} = -e n_\mathrm{e} \boldsymbol{u}_\mathrm{e}, \tag{2.4}$$

where $\boldsymbol{E}$ and $\boldsymbol{B}$ are the electric and magnetic fields of microwaves, respectively, $\boldsymbol{j}$ the plasma current density induced by microwaves, ϵ_0 the electric permittivity of vacuum, ϵ_r the relative permittivity, μ_0 the magnetic permeability of vacuum, e the magnitude of electron charge, m_e the mass of electron, $\boldsymbol{u}_\mathrm{e}$ the electron mean velocity driven by microwaves, ν_e the effective momentum transfer collision frequency between electrons and heavy particles, and n_e the plasma electron density. Equations (2.3) and (2.4) imply that the plasma is treated as a dielectric material of relative permittivity:

$$\epsilon_\mathrm{r} = \epsilon_\mathrm{p} = 1 - \frac{(\omega/\omega_\mathrm{pe})^{-2}}{1 - j(\nu_\mathrm{e}/\omega)}, \tag{2.5}$$

where j is the imaginary unit, ω the angular frequency of electromagnetic waves, and $\omega_{\mathrm{pe}} = (n_{\mathrm{e}}e^2/m_{\mathrm{e}}\epsilon_0)^{1/2}$ the plasma electron frequency. Note that in the dielectric/insulator region, the current density is set to be zero ($\boldsymbol{j} = 0$ or $\boldsymbol{u}_{\mathrm{e}} = 0$) with the permittivity ϵ_{r} of materials. The power absorption $\boldsymbol{j} \cdot \boldsymbol{E}$ in the plasma is taken to arise only from the classical Ohmic heating of electrons. Assuming the azimuthal symmetry of the configuration, only the transverse magnetic (TM) waves exist in the plasma chamber with $\boldsymbol{E} = (E_r, 0, E_z)$ and $\boldsymbol{B} = (0, B_\theta, 0)$.

The transverse electromagnetic (TEM) waves are injected into the system at the excitation plane (1.2 mm upstream of the end of the coaxial cable), and the total power injected into the chamber is monitored thereat by using

$$P_{\mathrm{in}} = \frac{1}{\mu_0}\int_A (\boldsymbol{E} \times \boldsymbol{B})\mathrm{d}A, \tag{2.6}$$

where A is the cross section concerned. Mur's first-order absorbing boundary condition,

$$\frac{\partial E_r}{\partial x} - \frac{1}{c}\frac{\partial E_r}{\partial t} = 0, \tag{2.7}$$

is applied to the field component E_r at the left end of the coaxial cable (0.8 mm further upstream of the excitation plane), so that the electromagnetic waves propagating from the chamber to the excitation plane leave the simulation area without any artificial reflection. Here, c denotes the speed of electromagnetic waves in the insulator of the cable. Since all metallic parts are treated as perfectly conducting materials, the electric field components tangential to metal surfaces are set to be zero. The axisymmetry of the problem further implies that $E_r = 0$ and $\partial E_z/\partial r = 0$ on axis (at $r = 0$). The total absorbed power in the plasma is calculated as

$$P_{\mathrm{abs}} = \int_V Q_{\mathrm{abs}} dV = \int_V \left(\frac{1}{t_{\mathrm{p}}}\int_{t_{\mathrm{p}}} \boldsymbol{j} \cdot \boldsymbol{E} dt\right) dV, \tag{2.8}$$

where t_{p} is the period of the electromagnetic waves, Q_{abs} the time-averaged power density absorbed, and the averaged power density absorbed per unit volume is obtained from $\bar{Q}_{\mathrm{abs}} = P_{\mathrm{abs}}/V$ with the plasma volume V.

Fluid model module

The FM module for the entire region through the microplasma source to micronozzle consists of two-temperature Navier-Stokes equations and the equation of state for a two-phase medium consisting of electrons and heavy particles (ions and neutrals) [42]:

$$\frac{\partial}{\partial t}\rho + \nabla \cdot (\rho \boldsymbol{v}) = 0, \tag{2.9}$$

$$\frac{\partial}{\partial t}(\rho \boldsymbol{v}) + \nabla \cdot (\rho \boldsymbol{v}\boldsymbol{v}) = -\nabla p + \nabla \boldsymbol{\tau}, \tag{2.10}$$

$$\frac{\partial}{\partial t} n_\mathrm{e} + \nabla \cdot (n_\mathrm{e} \boldsymbol{v}) = \nabla \cdot (D_\mathrm{a} \nabla n_\mathrm{e}) + \dot{n}_\mathrm{e}, \tag{2.11}$$

$$\frac{\partial}{\partial t} n_* + \nabla \cdot (n_* \boldsymbol{v}) = \nabla \cdot (D_* \nabla n_*) + \dot{n}_*, \tag{2.12}$$

$$\frac{\partial}{\partial t}\left(\frac{3}{2} n_\mathrm{e} k_\mathrm{B} T_\mathrm{e}\right) + \nabla \cdot \left(\frac{5}{2} n_\mathrm{e} k_\mathrm{B} T_\mathrm{e} \boldsymbol{v}\right) = (\boldsymbol{v} \cdot \nabla) p_\mathrm{e} - \nabla \cdot \boldsymbol{q}_\mathrm{e} + Q_\mathrm{abs} - Q_\mathrm{elas} - Q_\mathrm{iz,ex} - Q_\mathrm{rad}, \tag{2.13}$$

$$\frac{\partial}{\partial t}\left(\frac{3}{2} n_\mathrm{h} k_\mathrm{B} T_\mathrm{h}\right) + \nabla \cdot \left(\frac{5}{2} n_\mathrm{h} k_\mathrm{B} T_\mathrm{h} \boldsymbol{v}\right) = (\boldsymbol{v} \cdot \nabla) p_\mathrm{h} + \boldsymbol{\tau} : \nabla \boldsymbol{v} - \nabla \cdot \boldsymbol{q}_\mathrm{h} + Q_\mathrm{elas}, \tag{2.14}$$

$$p = p_\mathrm{e} + p_\mathrm{h} = n_\mathrm{e} k_\mathrm{B} T_\mathrm{e} + n_\mathrm{h} k_\mathrm{B} T_\mathrm{h} = n_\mathrm{e} k_\mathrm{B} (T_\mathrm{e} + T_\mathrm{h}) + n_\mathrm{n} k_\mathrm{B} T_\mathrm{h}. \tag{2.15}$$

Equation (2.9) gives the overall mass continuity, where $\boldsymbol{v}$ is the convective velocity, and the total mass density is expressed as $\rho = m_\mathrm{e} n_\mathrm{e} + m_\mathrm{h} n_\mathrm{h} \approx m_\mathrm{h} n_\mathrm{h}$ with the mass $m_\mathrm{h} (= m_\mathrm{i} = m_\mathrm{n})$ and density $n_\mathrm{h} (= n_\mathrm{i} + n_\mathrm{n} \approx n_\mathrm{e} + n_\mathrm{n})$ of heavy particles. Equation (2.10) gives the overall momentum conservation, where p is the pressure and $\boldsymbol{\tau}$ is the stress tensor expressed as

$$\tau_{ij} = \eta\left(\frac{\partial v_i}{\partial x_j} + \frac{\partial v_j}{\partial x_i}\right) - \frac{2}{3}\eta \delta_{ij} \frac{\partial v_k}{\partial x_k}, \tag{2.16}$$

with the viscosity η and Kronecker delta δ_{ij}. Equation (2.11) gives the conservation of electrons, with the ambipolar diffusion coefficient D_a and the source term $\dot{n}_\mathrm{e}$ for production/destruction of plasma electrons. Equation (2.12) gives the conservation of Ar^* metastables, where n_* is the density of Ar^* atoms (the neutral density is $n_\mathrm{n} = n_\mathrm{g} + n_*$ with the density n_g of ground-state Ar atoms), D_* the diffusivity of Ar^* in Ar, and $\dot{n}_*$ the source term for production/destruction of Ar^*.

Table 2.1: Inelastic electron collision processes used in the simulation (H_j is the excitation/de-excitation energy of the reaction j).

No.	Process	Reaction	H_j (eV)	Ref.
R1	Ground state ionization	$Ar + e \rightarrow Ar^+ + 2e$	15.7	[53, 54]
R2	Ground state excitation	$Ar + e \rightarrow Ar^* + e$	11.6	[53–55]
R3	Step-wise ionization	$Ar^* + e \rightarrow Ar^+ + 2e$	4.1	[56]
R4	Three-body recombination	$Ar^+ + 2e \rightarrow Ar + e$	−15.7	—
R5	Superelastic collision	$Ar^* + e \rightarrow Ar + e$	−11.6	—
R6	Two-body recombination	$Ar^+ + e \rightarrow Ar^* + (h\nu)$	−4.1	—

Equations (2.13) and (2.14) give the energy conservation of electrons and heavy particles, respectively, where k_B is the Boltzmann constant, p_s the pressure, $\boldsymbol{q}_s$ the heat flux defined as

$$\boldsymbol{q}_s = -\kappa_s \nabla T_s, \tag{2.17}$$

with the thermal conductivity κ_s, and Q_{abs} the absorbed power density of microwaves in the plasma source region ($Q_{abs} = 0$ in the nozzle). Here, the subscript $s = e, h$ indicates electrons or heavy particles. Moreover, Q_{elas} denotes the energy exchange due to elastic collision between electrons and heavy particles, $Q_{iz,ex}$ the energy exchange due to the excitation/de-excitation and ionization/recombination as listed in Table 2.1, and Q_{rad} the radiative energy loss. The electron viscous dissipation is neglected because of its small effect as compared with other terms in the equation. Finally, Eq. (2.15) gives the equation of state.

In these equations, most of the transport coefficients (η, D_a, κ_s) and the energy exchange terms (Q_{elas}, Q_{rad}) were taken to be the same as before [42, 52], and the diffusivity D_* was taken from Ref. [55]. In the terms concerned with nonelastic collision processes ($\dot{n}_e, \dot{n}_*, Q_{iz,ex}$), the ionization and excitation rates (for reactions R1 – R3 in Table 2.1) were taken from Refs. [53–56], and the rate coefficients for the reverse processes (R4 – R6) were determined from the so-called principle of detailed balance [57]. The rate coefficients of forward reactions (R1 – R3) are shown in Fig. 2.1 as a function of electron temperature T_e.

The boundary conditions employed are:

1. the feed gases enter the plasma source region at its left end through an annu-

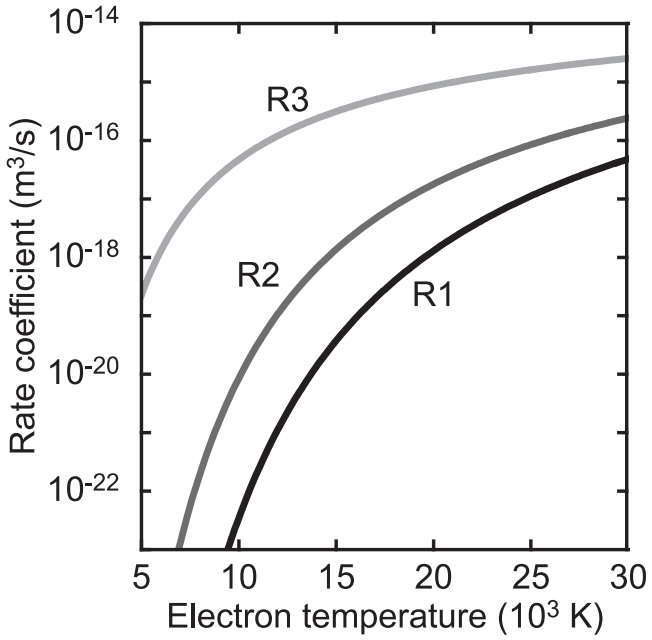

Figure 2.1: Rate coefficients for electron collision processes in Ar (see Table 2.1) as a function of electron temperature T_e.

lar spacing thereat, where the radial velocity is set to be zero, and the axial velocity is taken to be the thermal velocity at room temperature.

2. At the nozzle exit, all the flow properties are extrapolated from the interior, although some portion of the exit flow near the nozzle wall is subsonic; in practice, the effect of ambient pressure is assumed to be very small as long as it is sufficiently low, which is normally satisfied in space.

3. The axisymmetry of the problem implies that the radial velocity and the radial derivatives of the other flow properties (density, temperature, pressure, axial velocity, etc.) are set to be zero on axis (at $r = 0$).

4. On the walls of the plasma source and nozzle, the non-slip conditions are imposed for flow velocity, and the pressure gradient normal to the walls is set to be zero. Moreover, the walls are assumed to be non-catalytic, so that the metastable density gradient normal to the walls is also taken to be zero.

5. The electron flux and electron energy flux at the plasma-wall interfaces are assumed to be given by [52]

$$\Gamma_{e\perp} = (-D_a \nabla n_e)_\perp = 0.61 n_e \left(\frac{k_B T_e}{m_i}\right)^{1/2}, \tag{2.18}$$

$$q_{e\perp} = (-\kappa_e \nabla T_e)_\perp = (\mathcal{E}_e + \mathcal{E}_i)\Gamma_{e\perp}, \tag{2.19}$$

where $\Gamma_{e\perp}$ and $Q_{e\perp}$ are the respective components of $\mathbf{\Gamma}_e$ and $\boldsymbol{q}_e$ normal to the interfaces at the sheath-presheath boundaries; $\mathcal{E}_e = 2k_B T_e$ and $\mathcal{E}_i = 0.5k_B T_e[1 + \ln(m_i/2\pi m_e)]$ are the average energy lost at the boundaries per electron and ion, respectively ($\mathcal{E}_i = 5.2k_B T_e$ for Ar).

6. The heavy particle temperature at the interfaces is taken to be isothermal with a wall temperature $T_w = 500$ K for the plasma source region. On the other hand, the radiative boundary condition

$$\kappa_h \left.\frac{\partial T_h}{\partial n}\right|_w = \epsilon \sigma T_w^4 \tag{2.20}$$

is employed for the nozzle region, where $\epsilon = 1.0$ and $\sigma = 5.67 \times 10^{-8}$ W m^{-2} K^{-4} are the emissivity and the Stefan-Boltzmann constant, respectively, and $\partial/\partial n$ is the derivative normal to the walls.

2.2.2 Numerical procedures

In the EM module for the microplasma source, Eqs. (2.1) – (2.4) were solved by using the finite-difference time-domain approximation with a time increment Δt_{FDTD}. The FDTD unit cell and computational grids of the EM module were similar to those used before [42, 51, 52], together with the corresponding difference equations and boundary conditions. The spatial steps were taken to be $\Delta r = \Delta z = 0.01$ mm in the source region, where the simulation area was divided into 1350 cells in the axial direction and 240 cells in the radial direction at regular intervals using rectangular cells.

In the FM module for the entire region through the microplasma source to micronozzle, Eqs. (2.9) – (2.15) were all discretized in a finite difference manner,

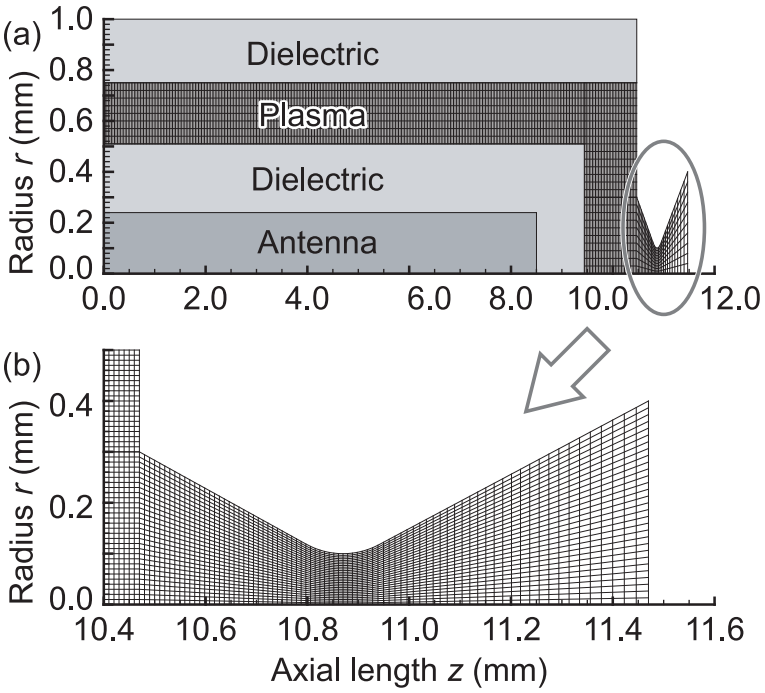

Figure 2.2: (a) Cross-sectional view and computational grids for the microplasma source and micronozzle regions, and (b) an enlarged view of the nozzle region.

and the discrete equations were solved by using an implicit LUSGS (Lower-Upper Symmetric Gauss-Seidel) scheme with a time increment $\Delta t_{\mathrm{Fluid}}$ [58]. The fluid unit cell and computational grids of the FM module in the plasma source region were taken to be the same as those of the EM module, being rectangular as mentioned above; on the other hand, the grids of the FM module in the nozzle region were curvilinear, being the same as those used before [42]; in practice, the simulation area of the nozzle was divided into 81 cells in the axial direction with the grid spacing being finer near the throat and 30 cells in the radial direction at regular intervals, as shown in Fig. 2.2.

It is expected that the high-frequency perturbations of electromagnetic waves are separated from the ambipolar electric fields governed by relatively slow plasma and fluid evolution, because the characteristic timescale for the latter is much longer than that for the former. Thus, a self-consistent solution was ob-

tained by applying the different timescale integration to the two modules of EM and FM, as in [52]:

1. first, the microwave input power $P_{\rm in}$ and the gas injection flow rate are give to the system, together with the electron $n_{\rm e}(r,z)$, metastable $n_*(r,z)$, and neutral $n_{\rm n}(r,z)$ densities, the flow velocity $\boldsymbol{v}(r,z)$, and the electron $T_{\rm e}(r,z)$ and heavy particle $T_{\rm h}(r,z)$ temperatures; then, the electromagnetic fields of microwaves injected are calculated in the EM module, with a time increment $\Delta t_{\rm FDTD}$ $(= 4.5\times10^{-14}{\rm s})$ for a time span $T_{\rm FDTD}$ of typically several microwave periods.

2. The absorbed power density $Q_{\rm abs}(r,z)$ in the plasma source region is calculated at the end of the EM calculation, which is an input to the FM module.

3. Then, the plasma and fluid evolution is traced by the FM module in the entire region through the plasma source to nozzle with a time increment $\Delta t_{\rm Fluid}(= 1.5\times10^{-11}{\rm s})$ for a time span $T_{\rm Fluid}(\gg T_{\rm FDTD})$, to give the distribution of the plasma and fluid parameters in both the plasma source and nozzle.

4. At the end of the FM calculation, the instantaneous distribution of the plasma and fluid parameters are given to the EM module.

These procedures are repeated until the plasma and fluid properties converge in the entire region of plasma source and nozzle, to finally also give the thrust performance.

2.2.3 Numerical results

Figures 2.3(a) – 2.3(h) show the spatial distribution of the electron density $n_{\rm e}$, electron temperature $T_{\rm e}$, heavy particle temperature $T_{\rm h}$, absorbed power density $Q_{\rm abs}$, pressure p, axial flow velocity u, Ar ground-state density $n_{\rm g}$, and Ar metastable state density n_* in the microplasma source, respectively, calculated for an input power $P_{\rm in}$ = 6.0 W of f = 4 GHz microwaves, Ar mass flow rate $\dot{m}$ = 1.5

mg/s (flow rate of 50 sccm), and quartz chamber and envelope ($\epsilon_{\rm d} = 3.8$). Here, the diameter and length of the antenna are $d_{\rm an} = 0.48$ mm and $L_{\rm an} = 8.5$ mm, respectively; the inner diameter, outer diameter, and length of the dielectric envelope covering the antenna are $d_{d,\rm in} = d_{\rm an} = 0.48$ mm, $d_{d,\rm out} = 0.96$ mm, and $L_d = 9.5$ mm, respectively; the inner diameter, outer diameter, and length of the dielectric chamber of the microplasma source are $d_{s,\rm in} = 1.44$ mm, $d_{s,\rm out} = 3.0$ mm, and $L_s = 10.5$ mm, respectively. The absorbed power calculated in the plasma is $P_{\rm abs} = 5.0$ W in total, corresponding to the average power density $\bar{Q}_{\rm abs} = 6.3 \times 10^8$ W/m^3. Note that the microwave power not absorbed in the plasma is reflected and/or passing through the source-nozzle boundaries, to leave the simulation area. The plasma density $n_{\rm e}$ exhibits its maximum near the end of the dielectric envelope of the antenna ($n_{\rm e} \approx 1.4 \times 10^{20}$ m^{-3}), being consistent with the distribution of the absorbed power density $Q_{\rm abs}$. On the other hand, the heavy particle temperature $T_{\rm h}$ exhibits its maximum in a space between the end of the dielectric envelope and the end wall of the dielectric plasma source chamber ($T_{\rm h} \approx 880$ K), where the micronozzle is located to achieve the aerodynamic acceleration of high temperature plasmas. Such distribution of the gas temperature is preferred for a thruster of electrothermal type using a Laval nozzle (or a converging-diverging nozzle), because the plasma thermal energy should be converted into directional kinetic energy of the supersonic flow without any undesirable energy loss in the plasma source region before entering the nozzle. In addition, the pressure calculated was almost uniform in the plasma source ($p \approx 34$ kPa), and the flow velocity was increased in the axial direction toward the end of the source region (up to $u \approx 40$ m/s).

Also shown in Figs. 2.3(i) and 2.3(j) are snapshots of the distribution of the radial E_r and axial E_z electric fields of microwaves. The corresponding extended views of the electric fields in the dielectric as well as in the plasma are also shown in Figs. 2.4(a) and 2.4(b). These results indicate that the strength of E_r is more than ten times smaller than that of E_z in the plasma, while the former is about ten times larger than the latter in the dielectric. Moreover, the peak position of the

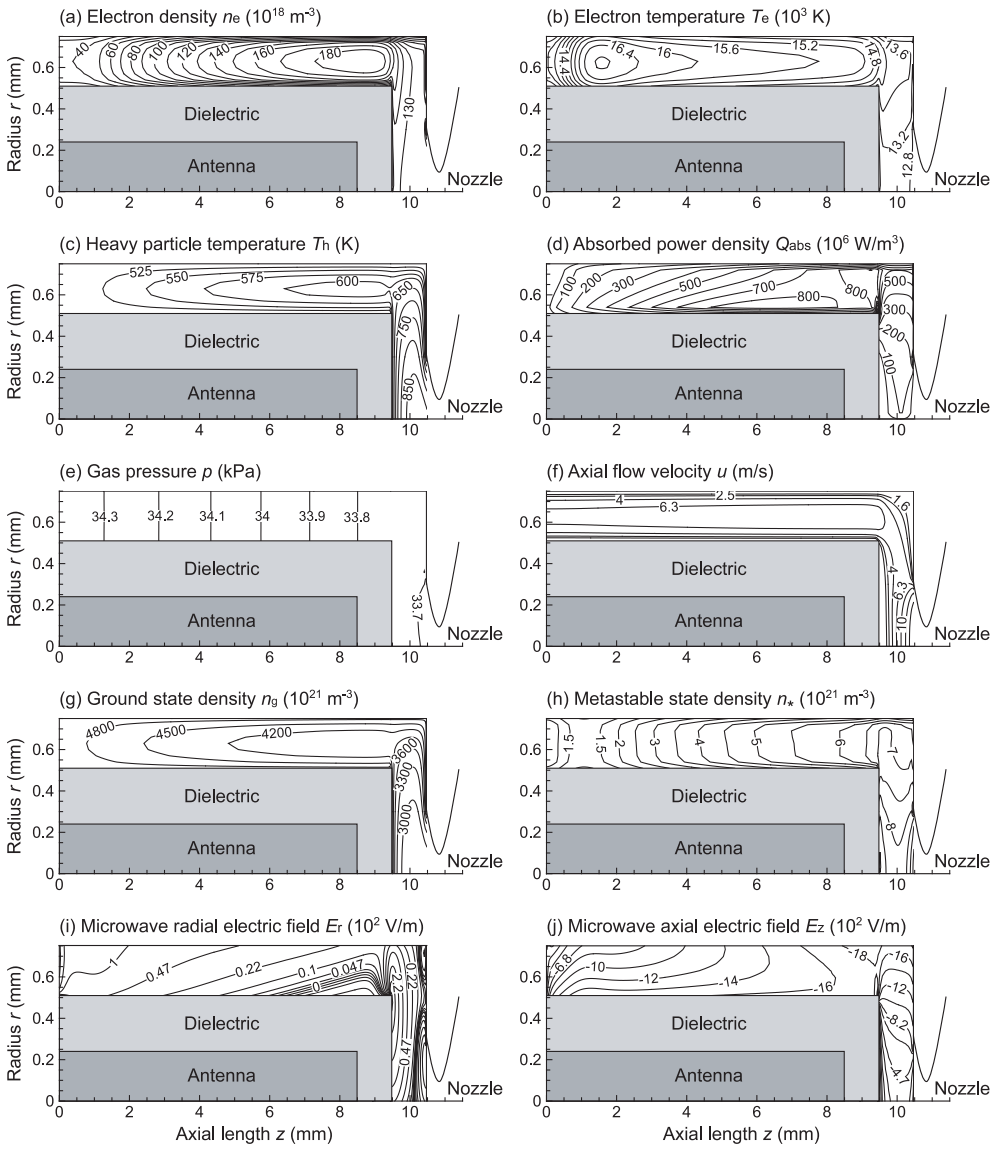

Figure 2.3: Distribution of the (a) electron density n_e, (b) electron temperature T_e, (c) heavy particle temperature T_h, (d) absorbed power density Q_{abs}, (e) gas pressure p, (f) axial flow velocity u, (g) Ar ground-state density n_g, and (h) Ar metastable-state density n_* in the microplasma source, calculated for an input power $P_{in} = 6.0$ W of $f = 4$ GHz microwaves, Ar mass flow rate $\dot{m} = 1.5$ mg/s (flow rate of 50 sccm), and quartz chamber and envelope ($\epsilon_d = 3.8$). The microwave power absorbed in the plasma was calculated as $P_{abs} = 5.0$ W. Also shown is a snapshot of the distribution of the (i) radial E_r and (j) axial E_z electric fields of the microwaves in the microplasma region.

absorbed power density $Q_{\rm abs}$ corresponds to that of E_z (not E_r), implying that the axial E_z is the major component of microwave electric fields that contributes to $Q_{\rm abs}$ and thus to $P_{\rm abs}$. It should be noted here that the present two-dimensional numerical analysis, which takes into account the spatially nonuniform plasma distribution in the microplasma source, gives a high absorption efficiency $P_{\rm abs}/P_{\rm in} > 80$ % even for microwaves of low frequencies ($f = 4$ GHz). This is in contrast to the results of our previous numerical study assuming the spatially uniform plasma distribution in the source [42], being ascribed to the localized absorption of microwaves or inhomogeneous heating of electrons in the interaction of electromagnetic waves with nonuniform plasmas. In practice, the strength of E_z in the plasma is largest near the plasma-dielectric interfaces, further increasing with increasing axial distance downstream toward the end of the antenna or dielectric envelope, as can be seen in Figs. 2.3(j) and 2.4(b). Numerical results also indicated that the microwave power absorbed does not rely significantly on microwave frequency f and relative permittivity $\epsilon_{\rm d}$ of dielectrics, but rely significantly on the configuration of the microplasma source (e.g., chamber length and diameter, antenna length and diameter); however, at high frequencies ($f > 20$ GHz) and permittivities ($\epsilon_{\rm d} > 10$), the distribution of $Q_{\rm abs}$ (and also E_r and E_z) was found to be more localized at the plasma-dielectric interfaces, because the surface waves tend to be established thereat [42].

Figures 2.5(a) – 2.5(h) show the distribution of the electron density $n_{\rm e}$, electron temperature $T_{\rm e}$, heavy particle temperature $T_{\rm h}$, Mach number Ma, pressure p, axial flow velocity u, Ar ground-state density $n_{\rm g}$, and Ar metastable-state density n_* in the micronozzle, respectively, obtained in the same numerical simulation as Figs. 2.3 and 2.4. Here, the Mach number is given by $Ma = |\boldsymbol{v}|(\gamma k_{\rm B} T_{\rm h}/m_{\rm h})^{-1/2}$, where $\gamma = 5/3$ is the specific heat ratio for monoatomic gases. The temperature $T_{\rm h}$, Mach number Ma, pressure p, and axial velocity u exhibit a characteristic of the subsonic-supersonic flow in the converging-diverging nozzle: Ma and u increase with increasing axial distance, with $Ma = 1$ being at around the throat, while $T_{\rm h}$ and p decrease downstream along the nozzle axis. However, the con-

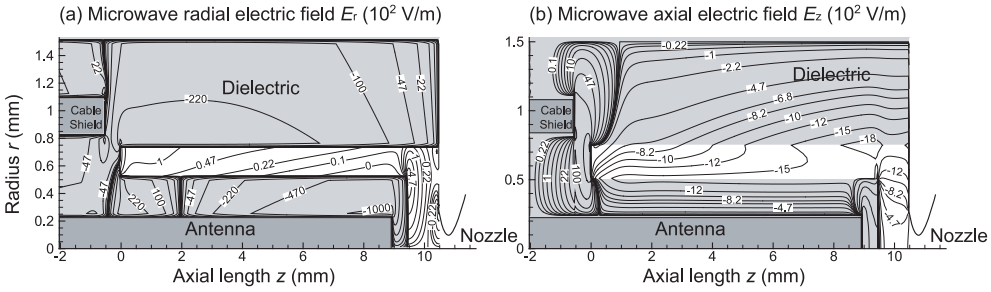

Figure 2.4: Extended view of a snapshot of the distribution of the (a) radial E_r and (b) axial E_z electric fields of microwaves in the microplasma source, corresponding to Figs. 2.3(i) and 2.3(j). The figure includes the region of coaxial cable for microwave injection and the region of dielectric material containing the plasma. Note that the excitation plane for microwave injection in the numerical analysis is at $z = -1.2$ mm, and the boundary for Mur's first-order absorbing condition is at $z = -2$ mm.

tour of Ma and u indicates that the boundary layer associated with viscosity is relatively thick in the micronozzle flow, especially in the divergent or supersonic portion of the nozzle [42]; in practice, the flow is supersonic around the nozzle axis therein, while subsonic near the walls over roughly half of the nozzle cross section. Note that the decrease of the temperature T_h along the axis is not so significant as compared to that of p, Ma, and u, owing to heating due to viscous dissipation in thick boundary layers. It is further noted that the plasma density n_e decreases downstream along the nozzle axis, which is similar to the behavior of the pressure p and mass density ρ ($\approx n_\mathrm{g}$); on the other hand, the electron temperature T_e exhibits no significant change along the axis, owing to the energy gained by plasma electrons through inelastic processes of electron-impact de-excitation and electron-ion recombination during expansion.

Figures 2.6 and 2.7 shows the contour of plasma and flow properties in the microplasma source and micronozzle, respectively, for a reduced Ar mass flow rate of $\dot{m} = 0.45$ mg/s (flow rate of 15 sccm), calculated with the other parameters being the same as in Figs. 2.3 – 2.5. A comparison of the temperature T_h, Mach number Ma, and flow velocity u in the micronozzle between Figs. 2.5 and 2.7

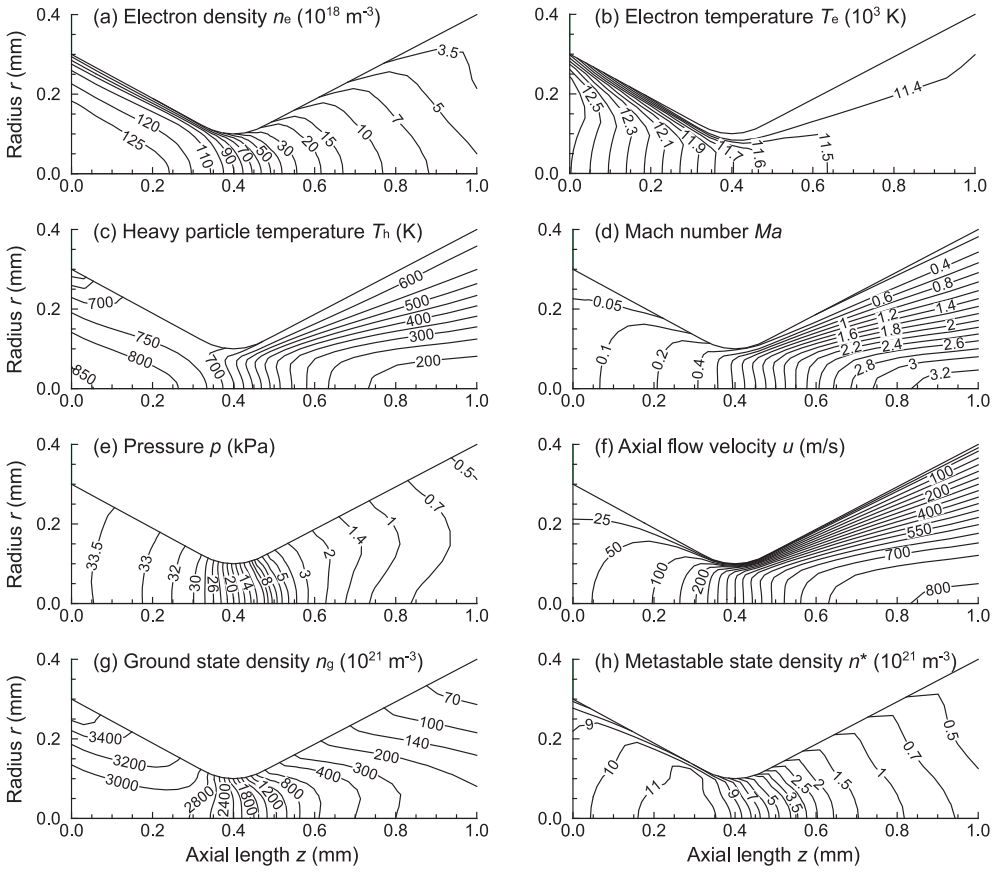

Figure 2.5: Distribution of the (a) electron density n_e, (b) electron temperature T_e, (c) heavy particle temperature T_h, (d) Mach number Ma, (e) pressure p, (f) axial flow velocity u, (g) Ar ground-state density n_g, and (h) Ar metastable-state density n_* in the micronozzle, obtained in the same numerical simulation as Figs. 2.3 and 2.4. The nozzle shown has an inlet, throat, and exit diameter of d_{in} = 0.6 mm, d_{th} = 0.2 mm, and d_{ex} = 0.8 mm, respectively, with a diverging angle of $\theta = 26.6^\circ$ and a total length of 1 mm.

indicate that although significant boundary layers occur at both flow rates, the layer tends to be thicker at 0.45 mg/s than at 1.5 mg/s in the divergent portion of the nozzle. In practice, the minimum T_h and the maximum Ma and u are obseved inside the micronozzle, not at the nozzle exit, at low 0.45 mg/s. Thus, it follows that at lower gas flow rates, the thicker boundary layers impede the flow expansion in the micronozzle, where the nozzle flow is heavily underexpanded to decelerate the supersonic flow downstream along the axis in the diverging portion of the nozzle. The thicker boundary layers at lower flow rates are attributed to higher T_h thereat [see Figs. 2.5(c) and 2.7(c)]; in effect, the viscosity is a function of temperature T_h, increasing with increasing T_h, which in turn leads to higher viscous dissipation and thus to further increased T_h. The higher T_h at lower flow rates in the micronozzle originate from higher T_h achieved around the end of the antenna in the microplasma source region, as can be seen in Figs. 2.3(c) and 2.6(c), where lower pressure p or density n_g with similar values of the absorbed power density Q_{abs} would result in higher T_h.

Such boundary layer effects were also observed at high input and thus absorbed powers (high P_{in} and thus P_{abs} or Q_{abs}), where the micronozzle flow is heavily affected by viscous dissipation in boundary layers owing to the high temperature T_h of heavy particles. It should be concluded that the gas/plasma flow in the microplasma source and micronozzle is often heavily affected by the effects of boundary layers at the wall; especially in the micronozzle, the thickness of boundary layers tends to be comparable to the nozzle radius, and the viscous dissipation in boundary layers often affects the flow properties, aerodynamic acceleration of the flow, and thus thrust performance.

2.3 Experiment

Figure 2.8 shows a schematic of the experimental setup [44, 45, 47]. The microplasma source chamber was made of a quartz tube L_s = 10.5 mm long, $d_{s,in}$ = 1.5 mm in inner diameter, and $d_{s,out}$ = 3.0 mm in outer diameter. The cen-

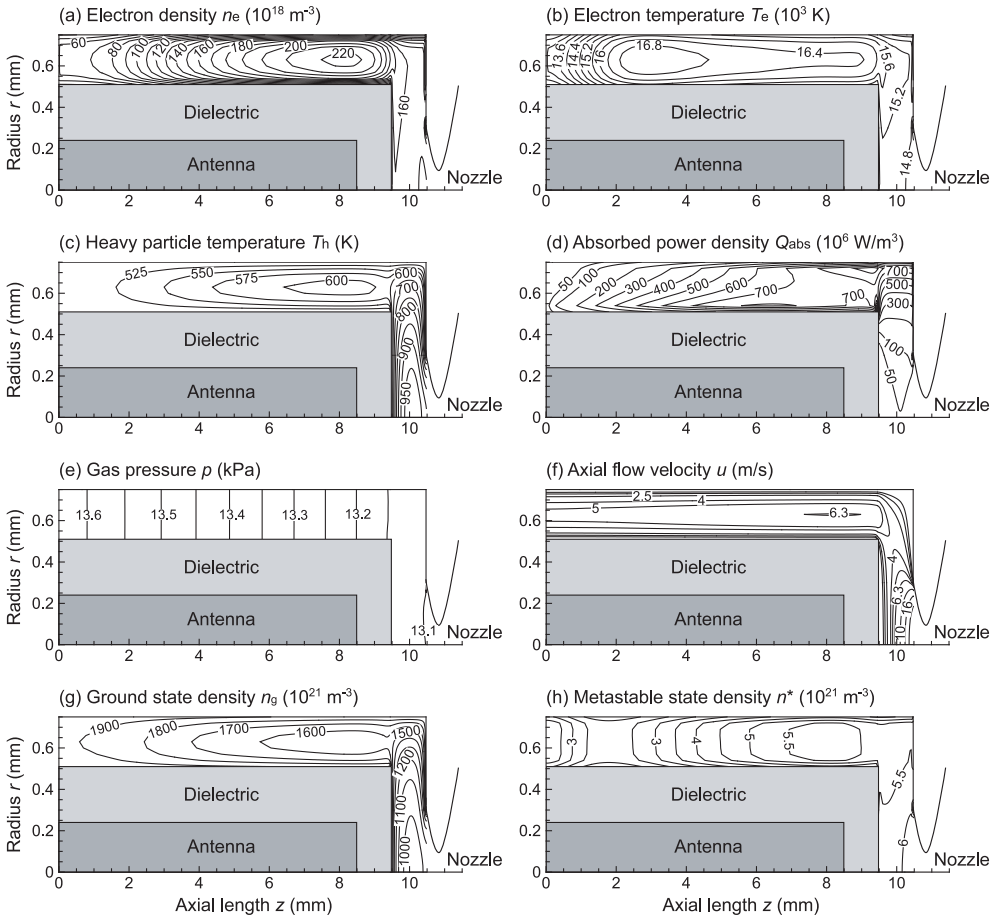

Figure 2.6: Distribution of the (a) electron density n_e, (b) electron temperature T_e, (c) heavy particle temperature T_h, (d) absorbed power density Q_{abs}, (e) gas pressure p, (f) axial flow velocity u, (g) Ar ground-state density n_g, and (h) Ar metastable-state density n_* in the microplasma source for an Ar mass flow rate $\dot{m}$ = 0.45 mg/s (or a flow rate of 15 sccm), calculated with the other parameters being the same as Figs. 2.3 – 2.5. The microwave power absorbed in the plasma was calculated as P_{abs} = 5.0 W.

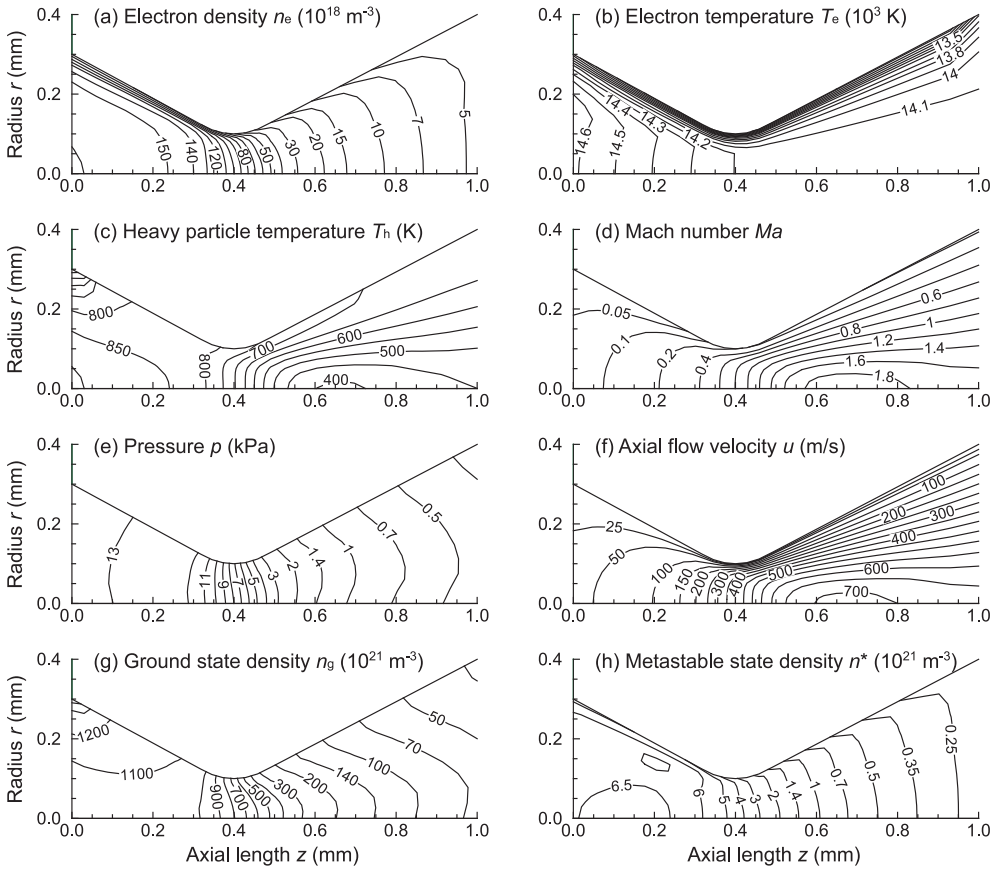

Figure 2.7: Distribution of the (a) electron density n_e, (b) electron temperature T_e, (c) heavy particle temperature T_h, (d) Mach number Ma, (e) pressure p, (f) axial flow velocity u, (g) Ar ground-state density n_g, and (h) Ar metastable-state density n_* in the micronozzle, obtained in the same numerical simulation as Fig. 2.6.

ter conductor of a semi-rigid coaxial cable (RG-405/U), protruding 10 mm beyond the insulator and outer conductor, was covered with a dielectric envelope, which was then inserted in the source chamber as a microwave antenna L_{an} = 8.5 mm long and d_{an} = 0.5 mm in diameter. The dielectric envelope of quartz covering the antenna was L_d = 9.5 mm long, $d_{d,in}$ = 0.5 mm in inner diameter, and $d_{d,out}$ = 1.0 mm in outer diameter. The plasma source chamber and antenna were inserted into a stainless-steel housing to cover the microplasma source with a metal grounded, where an annular spacing was retained for feeding the fuel gas. The microplasma source thus configured was located in a vacuum chamber pumped down by a dry and turbomolecular pump.

Microwave signals of f = 4 GHz from a signal generator (Agilent 8648D) were amplified through a four-stage semiconductor amplifier to powers of nominally $P_{in} < 10$ W, and then fed into the microplasma source through the semi-rigid coaxial cable. The working gas was Ar in this study, being supplied through a mass flow controller; in some cases, a small amount (< 5 %) of N_2 and H_2 was added for plasma diagnostics. The feed gas pressure p_0 in the microplasma source was measured by a pressure gauge set upstream of the source chamber. Here, the reflection of microwaves was suppressed by adjusting the length of the coaxial cable and antenna.

Figure 2.9 (a) shows a microscope image of the micronozzle fabricated in a 1-mm-thick quartz plate by using a micromachining process with a diamond drill [45, 47]. The nozzle shown has an inlet, throat, and exit diameter of d_{in} = 0.6, d_{th} = 0.2, and d_{ex} = 0.8 mm, respectively, being similar to the nozzle configuration of Figs. 2.5 and 2.7; the micronozzle was attached to one end of the microplasma source chamber, as shown in Fig. 2.8. Plasma discharges gave an elongated plume of supersonic plasma jet freely expanded downstream of the nozzle exit into vacuum, as can be seen in a photograph image shown in Fig. 2.9(b) (f = 4 GHz, P_{in} = 6 W, $\epsilon_d \approx 3.8$, Ar 50 sccm, p_0 = 31 kPa); the length of the plasma jet plume was observed to increase with increasing microwave input power P_{in} and gas flow rate. In addition, the jet plume was observed to have a system of shocks therein

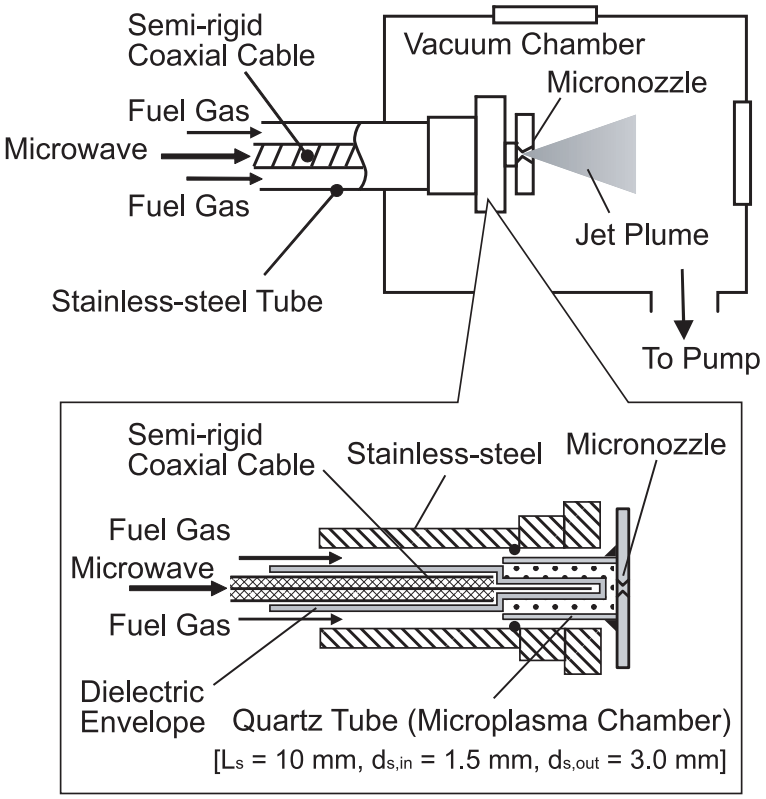

Figure 2.8: Experimental setup, together with an enlarged view of the microwave-excited microplasma source having a configuration and size similar to those shown in Figs. 2.3, 2.4, and 2.6. Here, the dielectric envelope was also made of quartz. Optical emission spectroscopy was employed in the side-view direction, through a small hole of the stainless-steel housing around the end of the antenna or dielectric envelope, just upstream of the micronozzle inlet [45].

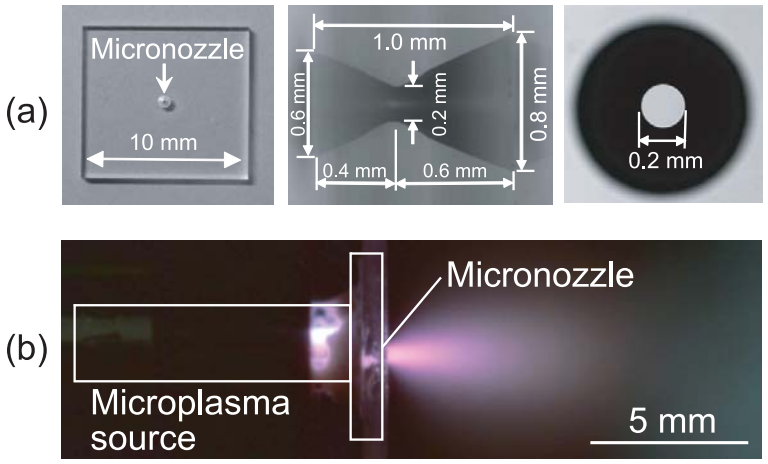

Figure 2.9: (a) Microscope image of the micronozzle fabricated in a 1-mm-thick quartz plate, which has an inlet, throat, and exit diameter similar to the configuration shown in Figs. 2.5 and 2.7. (b) Photograph image of the supersonic Ar plasma jet plume freely expanded into vacuum through the nozzle, taken under operating conditions of $f = 4$ GHz, $P_{\rm in} = 6$ W, $\epsilon_{\rm d} \approx 3.8$, Ar 50 sccm (= 1.5 mg/s), and $p_0 = 31$ kPa.

(barrel shock at the sides and Mach disk shock normal to the centerline), indicating a supersonic free-jet expansion through an orifice or nozzle into vacuum [59].

The gas flow rate (or mass flow rate $\dot{m}$) and the source pressure p_0 measured with and without plasma discharge were approximately related by the quasi-one dimensional nozzle flow equation for an isentropic flow of perfect gases in a converging-diverging nozzle [60, 61],

$$\dot{m} = \rho u A = p_0 A^* \left[\frac{\gamma}{RT_0} \left(\frac{2}{\gamma+1} \right)^{(\gamma+1)/(\gamma-1)} \right]^{1/2}, \tag{2.21}$$

as shown in Fig. 2.10. The equation assumes the so-called choked flow, or the sonic velocity at the throat followed by further increase in velocity under supersonic flow conditions in the divergent portion of the nozzle. Here, ρ is the mass density, u the flow velocity, A the cross section of the nozzle, A^* that of the throat, γ the specific heat ratio ($\gamma = 5/3$ for Ar), R the universal gas constant ($R = k_B/m_h$), and T_0 the gas/plasma temperature in the microplasma source. The temperature T_0 was taken to be the room temperature in cold gas operation, and the gas/rotational

temperature spectroscopically measured in plasma discharge (as will be shown below in Sec. 2.4).

To characterize the microplasma concerned, the optical emission from the plasma was observed in the side-view direction through a 1-mm-diam small hole of the stainless-steel housing around the end of the antenna or dielectric envelope (just upstream of the micronozzle inlet) [45]. The spectrometer employed consisted of a 50-cm focal length spectrograph/monochromator (Acton SpectraPro 2500i) with a grating of 2400 lines/mm, charge-coupled device (CCD) detector (Princeton PI-MAX1K; 1024 × 1024 pixels, 13.3 mm × 13.3 mm), and photomultiplier (Hamamatsu R2949); a set of lenses were used to collect the emission from the plasma and focused it onto the entrance slit of the spectrometer. The spectral resolution, determined using a low-pressure Ar discharge lamp, was 0.025 nm with an entrance slit width of 5 μm. In addition, a Langmuir probe was located in the plasma jet plume downstream of the nozzle exit, to measure the plasma electron density therein [44], where the probe was cylindrical with a tungsten wire 0.05 mm in diameter and 0.5 mm long.

2.4 Plasma characteristics

The gas/rotational temperature was measured by adding a small amount of N_2 and analyzing the optical emission spectrum of the N_2 2nd positive (0,2) band (N_2 $C^3\Pi_u, v' = 0 \rightarrow B^3\Pi_g, v'' = 2$) at 380.4 nm. Figure 2.11 (a) shows a typical vibronic spectrum of the 380.4-nm N_2 band experimentally observed under the same conditions as in Fig. 2.9 (b) (f = 4 GHz, $P_{\rm in}$ = 6 W, $\epsilon_{\rm d} \approx 3.8$, Ar 50 sccm, p_0 = 31 kPa), together with the spectrum theoretically calculated assuming the temperature $T_{\rm g} \approx T_{\rm rot}$ = 890 K.

The plasma electron density was measured by adding a small amount of H_2 and analyzing the Stark broadening of the H Balmer-β (H_β) spectral line at 486.1 nm. It is generally appreciated that the H_β line broadening consists of the instrumentation $\Delta\lambda_{\rm instrum}$, Doppler $\Delta\lambda_{\rm Doppler}$ (depending on $T_{\rm g}$), pressure $\Delta\lambda_{\rm pressure}$

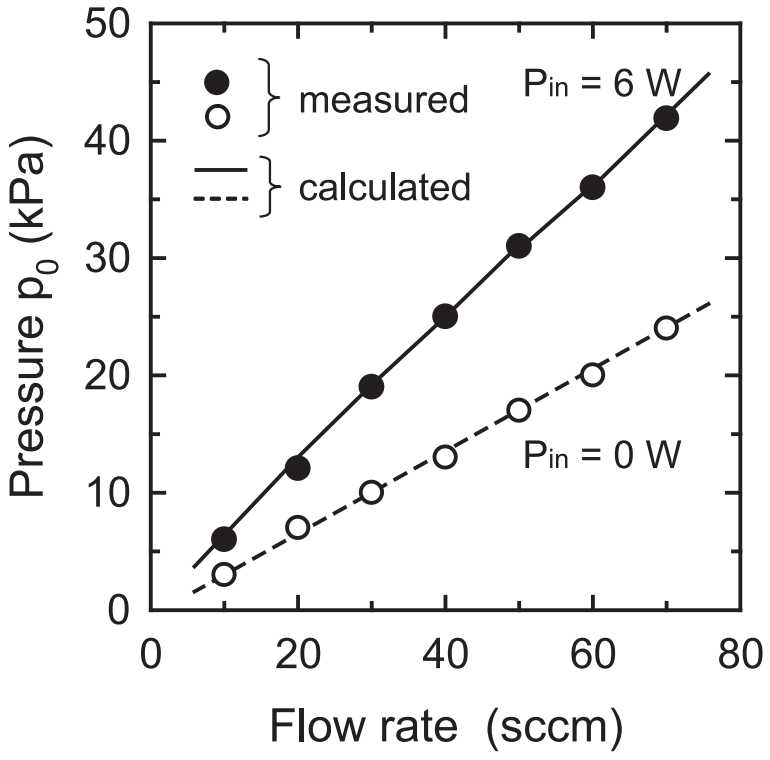

Figure 2.10: Source pressure p_0 measured as a function of gas flow rate (or mass flow rate $\dot{m}$) with and without plasma discharge (f = 4 GHz, P_{in} = 6 W, $\epsilon_d \approx 3.8$). Also shown are the curves calculated based on the quasi-one dimensional nozzle flow equation for an isentropic flow of perfect gases in a converging-diverging nozzle, assuming the so-called choked flow condition at the throat. Here, the gas/plasma temperature T_0 in the microplasma source was taken to be the room temperature in cold gas operation, and the gas/rotational temperature spectroscopically measured in plasma discharge (as will be shown in Fig. 2.12).

(depending on T_g and p_0 or gas density n_g), and Stark broadening $\Delta\lambda_{Stark}$ (depending on n_e and T_e), where $\Delta\lambda_{instrum}$, $\Delta\lambda_{Doppler}$, $\Delta\lambda_{pressure}$, and $\Delta\lambda_{Stark}$ denote the respective full widths at half maximum (FWHMs) [62–65]; the former two are given by the Gaussian profile and the latter two by the Lorentzian profile, which are then approximated by the Voigt function in total,

$$V(\lambda;\sigma,\gamma) = \int_{-\infty}^{\infty} G(\lambda';\sigma)L(\lambda-\lambda';\gamma)d\lambda', \tag{2.22}$$

where λ is the wavelength from the line center, $G(\lambda;\sigma)$ the centered Gaussian component with an FWHM of $\Delta\lambda_G = 2\sigma(2\ln 2)^{1/2}$, and $L(\lambda;\gamma)$ the centered Lorentzian component with an FWHM of $\Delta\lambda_L = 2\gamma$. The FWHM of the Gaussian component of the Voigt profile is given by

$$\Delta\lambda_G = (\Delta\lambda_{instrum}^2 + \Delta\lambda_{Doppler}^2)^{1/2}, \tag{2.23}$$

and that of the Lorentzian component by

$$\Delta\lambda_L = \Delta\lambda_{pressure} + \Delta\lambda_{Stark}. \tag{2.24}$$

In the present experiments, the Van der Waals broadening was only taken into account for the pressure broadening, because the resonance broadening due to collisions between identical species could be neglected owing to a small amount of H_2 addition.

The instrumental broadening was estimated to be $\Delta\lambda_{instrum} \approx 0.025$ nm, as mentioned above in Sec. 2.3. The Doppler, pressure, and Stark broadening was analyzed as in [65]. Briefly, the respective FWHMs in nm are given by

$$\Delta\lambda_{Doppler} = 7.16\times10^{-7}\lambda\sqrt{\frac{T_H}{M}}, \tag{2.25}$$

$$\Delta\lambda_{pressure} \approx \Delta\lambda_{Van\,der\,Waals} \approx 4.09\times10^{-12}\lambda^2(\alpha\langle R\rangle)^{2/5}\left(\frac{T_g}{\mu}\right)^{3/10} n_{Ar}, \tag{2.26}$$

$$\Delta\lambda_{Stark} = 2.5\times10^{-10}a_{n'n}(n_e,T_e)n_e^{2/3}, \tag{2.27}$$

where λ is the wavelength of the emission line in nm, T_H the temperature of emitters in K, M the atomic weight of the emitter or H atom in atomic mass unit (amu);

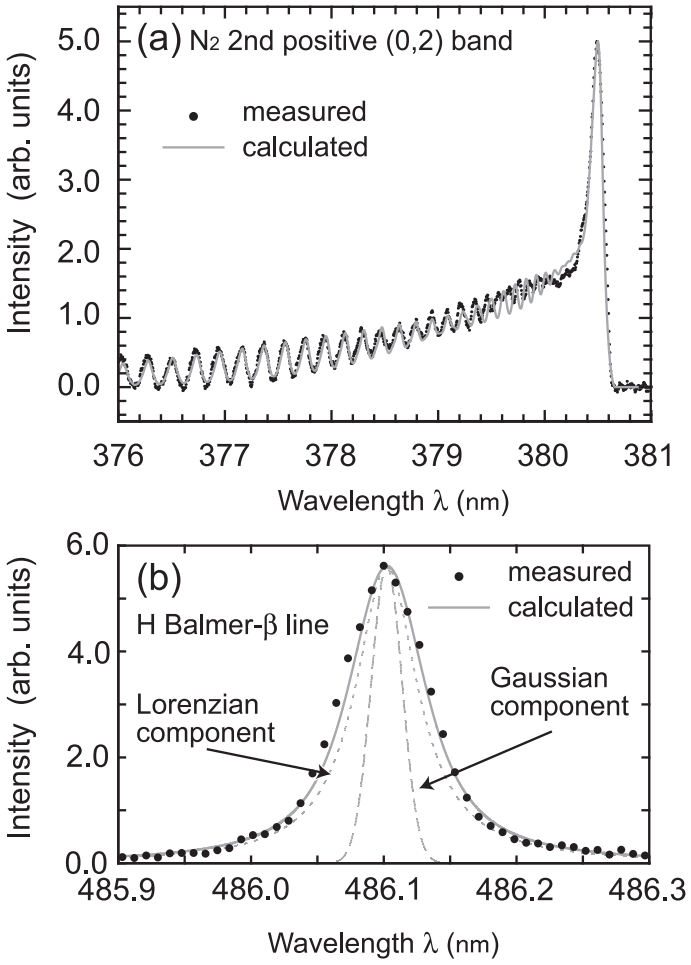

Figure 2.11: (a) Vibronic spectrum of the N_2 2nd positive (0, 2) band at 380.4 nm, together with the spectrum theoretically calculated assuming the gas or rotational temperature $T_g \approx T_{rot} = 890$ K. (b) Spectrum profile of the H Balmer-β line at 486.1 nm, together with the fitting Voigt function curve that gives an FWHM of $\Delta\lambda_V = 0.071$ nm. Also shown in (b) are the Gaussian and Lorentzian components of the Voigt profile with an FWHM of $\Delta\lambda_G \approx 0.027$ nm and $\Delta\lambda_L \approx 0.061$ nm, respectively, which gives the plasma electron density $n_e \approx 9.9 \times 10^{19}$ m^{-3}. These optical emissions were observed in the side-view direction through a small hole around the end of the microwave antenna or dielectric envelope (just upstream of the micronozzle inlet), under the same conditions as in Fig. 2.9(b) [$f = 4$ GHz, $P_{in} = 6$ W, $\epsilon_d \approx 3.8$, Ar 50 sccm (= 1.5 mg/s), and $p_0 = 31$ kPa].

moreover, α the mean atomic polarizability of neutral perturbers or Ar atoms in cm^3, $\langle R \rangle$ the parameter in cm^2 determined from atomic energy levels of the emitter, T_g the gas temperature in K, μ the emitter-perturber reduced mass in amu, and n_{Ar} the neutral Ar gas density in cm^{-3}; and $a_{n'n}$ is the parameter for the transition $n' - n$ of the emitter depending on n_e and T_e, and n_e the electron density in cm^{-3}. We took $\alpha \approx 11.08 a_0^3$ from Ref. [66], $\langle R \rangle \approx 600 a_0^2$ from Ref. [65], and $a_{n'n} \approx 0.08$ from Refs. [63, 67, 68] in this study, where a_0 is the Bohr radius in cm.

Figure 2.11(b) shows a typical profile of the H_β line spectrum at 486.1 nm experimentally observed under the same conditions as in Figs. 2.9(b) and 2.11(a), together with the best fitted curve of the Voigt function Eq. (2.22) that gives an FWHM of $\Delta\lambda_V \approx 0.071$ nm, where the fitting was performed according to the Marquardt-Levenberg method. In practice, $\Delta\lambda_G$ was calculated from Eq. (2.23) assuming the temperature $T_H \approx T_g \approx T_{rot}$ measured above, and $\Delta\lambda_L$ was obtained from the best fit between the experimental spectrum and the Voigt profile calculated; then, the Stark contribution $\Delta\lambda_{Stark}$ was found from Eq. (2.24), assuming the density $n_{Ar} \approx n_g \approx p_0/k_B T_g$. In the figure, $\Delta\lambda_G \approx 0.027$ nm ($\Delta\lambda_{instrum} \approx 0.025$ nm and $\Delta\lambda_{Doppler} \approx 0.010$ nm) gave $\Delta\lambda_L \approx 0.061$ nm ($\Delta\lambda_{pressure} \approx 0.010$ nm), which in turn gave $\Delta\lambda_{Stark} \approx 0.051$ nm and thus $n_e \approx 9.9 \times 10^{19}$ m^{-3}, assuming $T_g \approx 890$ K and $p_0 \approx 30$ kPa. It should be noted that the accuracy of the electron density determined from the Stark broadening relies on the spectral resolution of the measurement system and also on the assumption of analysis of the spectral line broadening; in practice, the present accuracy was estimated to be about ±20% at $P_{in} = 6$ W, primarily owing to the resolution $\Delta\lambda_{instrum}$ of the spectrometer system employed.

Figure 2.12 shows the plasma electron density n_e and gas/rotational temperature $T_g \approx T_{rot}$ measured as a function of Ar gas flow rate for different microwave powers P_{in} ($f = 4$ GHz, $\epsilon_d \approx 3.8$), where changing the flow rate led to a change in pressure p_0 or gas density n_g in the microplasma source as shown in Fig. 2.10. The electron density was in the range $n_e \approx (8 - 16) \times 10^{19}$ m^{-3}, being consistent with the Langmuir probe measurements in the supersonic plasma free jet

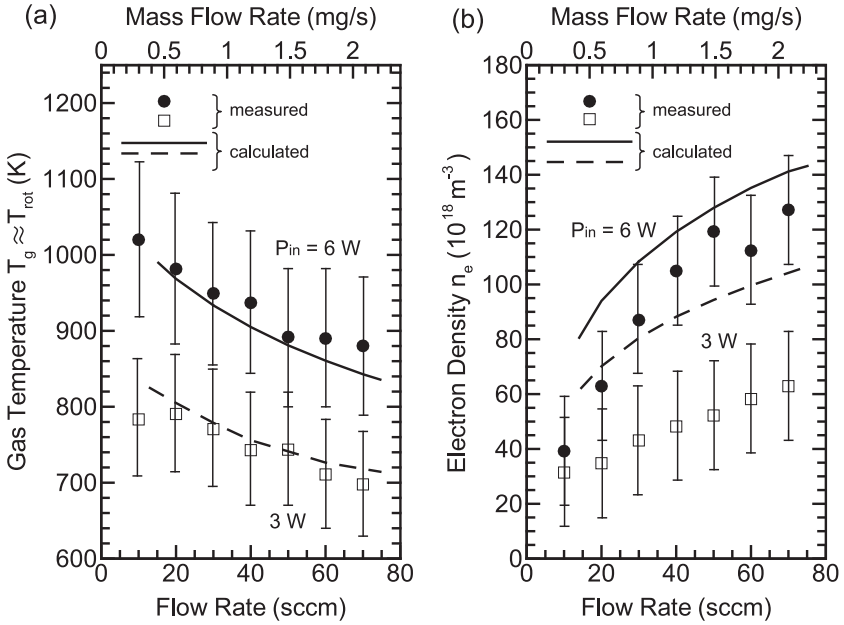

Figure 2.12: (a) Plasma electron density n_e and (b) gas temperature $T_g \approx T_{rot}$ measured as a function of Ar gas flow rate for different microwave powers P_{in}, where changing the flow rate led to a change in pressure p_0 in the microplasma source as shown in Fig. 2.10. These data were taken under conditions of f = 4 GHz and $\epsilon_d \approx 3.8$, with a small amount (0.2 sccm) of additive gases of H_2 and N_2. Also shown in the figure are the curves of n_e and $T_g(= T_h)$ numerically simulated as in Figs. 2.3 and 2.6, where the data are those line-averaged in the radial direction between the end of the antenna or dielectric envelope and the inlet of the micronozzle.

downstream of the nozzle [44]; moreover, the gas temperature was in the range $T_g \approx T_{rot} \approx 700 - 1000$ K. The temperature $T_g \approx T_{rot}$ was observed to increase with increasing P_{in}, and to decrease with increasing flow rate (or with increasing p_0 or n_g in the plasma source). On the other hand, the density n_e was observed to increase with increasing P_{in} and flow rate. Also shown in the figure are the curves of n_e and T_g $(= T_h)$ numerically simulated as in Figs. 2.3 and 2.6, where the data are those line-averaged in the radial direction between the end of the microwave antenna or dielectric envelope and the inlet of the nozzle, indicating that the experiments were in agreement with the numerical analysis.

2.5 Thrust performance

The thrust performance is calculated as [61, 69]

$$F_{\mathrm{t}} = 2\pi \int_0^{r_{\mathrm{ex}}} (\rho u^2 + p) r dr, \tag{2.28}$$

$$I_{\mathrm{sp}} = F_{\mathrm{t}} \left(2\pi g \int_0^{r_{\mathrm{ex}}} \rho u r dr \right)^{-1} = \frac{F_{\mathrm{t}}}{\dot{m} g}, \tag{2.29}$$

based on the numerical analysis in Sec. 2.2, where F_{t} is the thrust (or the reaction force to propel spacecraft) and I_{sp} is the specific impulse (or the fuel efficiency of thrusters). In these equations, r_{ex} denotes the exit radius of the nozzle, ρ the mass density, u the exhaust flow velocity in the axial direction, p the pressure, $\dot{m}$ the mass flow rate, and g the gravitational constant. Note that F_{t} consists of the momentum and pressure thrust. The pressure thrust is usually neglected owing to its less contribution to the total thrust; however, reducing the size of the nozzle results in under-expanded gas/plasma flows inside the nozzle owing to highly viscous flows therein, as mentioned earlier in Sec. 2.2.3, so that the pressure thrust should be taken into account in the present micro plasma thruster [42, 45].

The experimental setup for thrust measurement has been detailed elsewhere [45], which was newly developed for micro thrusters of $F_{\mathrm{t}} \leq 1$ mN, consisting of a pendulum-type stand for cold-gas operation and a target-type stand for both cold-gas and plasma-discharge operations. In the former, the thruster itself was hung; on the other hand, in the latter, a small concave cylindrical target block was hung downstream of the nozzle exit with the thruster fixed tightly, and the gas/plasma plume ejected from the thruster struck the target mounted at one end of the pendulum with some weights being at the other end for balance. Here, the target employed was a small Faraday cup-like one made of Teflon, to suppress the effects of reflected particles of the jet plume striking the target. A small displacement of $\Delta X < 0.1$ mm in oeration was measured by using a laser displacement gauge having a resolution of $\Delta x < 0.1\,\mu$m. It should be noted that the accuracy of the present thrust measurement was estimated to be about $\pm 10\%$, relying primarily on mechanical issues of the measurement system such as effects of friction of

the knife edge on the rotational axis and effects of the reflected jet plume particles on the target.

Figure 2.13 shows the thrust performance (thrust F_t, specific impulse I_{sp}) measured and calculated as a function of Ar gas flow rate for different microwave input powers P_{in}, where $P_{in} = 0$ W corresponds to the cold-gas operation without plasma discharge. The measurements showed that the thrust performance was enhanced with the discharge on and with increasing P_{in}, and that the thrust and specific impulse were typically $F_t \approx 1.4$ mN and $I_{sp} \approx 80$ s, respectively, with the thrust efficiency $\eta_t \approx 8.7$ % at $P_{in} = 6$ W and a flow rate of 60 sccm (1.8 mg/s). In practice, a good agreement was obtained between the experiments and numerical analysis, giving $F_t \approx 0.2 - 1.4$ mN, $I_{sp} \approx 50 - 80$ s, and $\eta_t \approx 2 - 12$ % at $P_{in} \leq 6$ W and gas flow rates of 10 – 60 sccm.

2.6 Conclusions

A micro plasma thruster has been developed of electrothermal type using azimuthally symmetric microwave-excited microplasmas, which consisted of a microplasma source and micronozzle. The plasma source was made of a dielectric chamber 1.5 mm in diameter and 10 mm long covered with a metal grounded, having a metal rod antenna on axis covered with a dielectric envelope, to produce high temperature plasmas at around atmospheric pressures. The nozzle was a converging-diverging type (Laval nozzle) 1 mm long with a throat 0.2 mm in diameter, converting high thermal energy of plasmas into directional kinetic energy of supersonic plasma flows to obtain the thrust required. The feed or propellant gas employed was Ar at pressures of 10 – 50 kPa with flow rates of 10 – 70 sccm, and the surface wave-excited plasmas were established by 4.0 GHz microwaves at input powers of $P_{in} \leq 6$ W. Numerical analysis was made for the plasma and flow properties in the microplasma source and micronozzle by developing a self-consistent numerical model, where a two-temperature fluid model was applied to the entire region through the plasma source to nozzle; in the for-

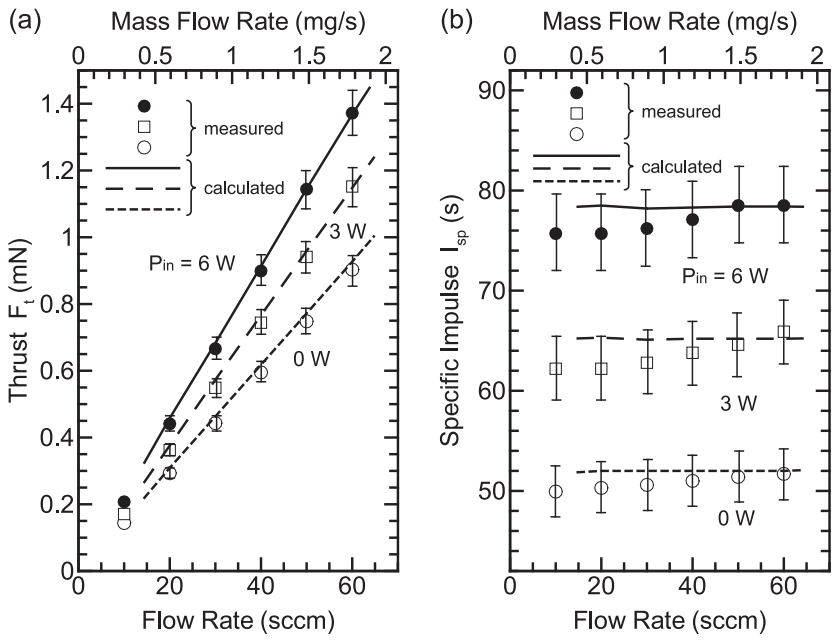

Figure 2.13: Thrust performance [(a) thrust F_t and (b) specific impulse I_{sp}] measured as a function of Ar gas flow rate for different microwave powers P_{in} under the same conditions as in Fig. 2.12 (f = 4 GHz, $\epsilon_d \approx 3.8$). Here, P_{in} = 0 W corresponds to the cold-gas operation without plasma discharge. Also shown in the figure are the curves of F_t and I_{sp} calculated from the numerical analysis as in Figs. 2.5 and 2.7.

mer, the electromagnetic model based on the FDTD approximation was also employed for analysis of microwaves interacting with plasmas. Numerical results revealed the spatially nonuniform distribution of plasma and flow parameters in the microplasma source: the absorbed power density, plasma density, and gas temperature are maximum at around the end of the microwave antenna or dielectric envelope (just upstream of the inlet of the micronozzle), which is preferred for a thruster of electrothermal type using the converging-diverging nozzle. The numerical results also indicated that the supersonic flow in the micronozzle is heavily affected by viscous dissipation in thick boundary layers, and that the deceleration of supersonic flow occurs at low gas flow rates and high input powers.

Optical emission spectroscopy was employed with a small amount of additive gases of H_2 and N_2, to measure the plasma electron density and gas temperature in the microplasma source at around the end of the antenna or dielectric envelope. The analysis of the Stark broadening of H Balmer H_β spectral line and the vibronic spectrum of N_2 2nd positive (0, 2) band indicated that the electron density was in the range $n_e \approx (3 - 12) \times 10^{19}$ m^{-3} and the gas or rotational temperature was in the range $T_g \approx T_{rot} \approx 700 - 1000$ K; in practice, n_e was found to increase with increasing microwave power and flow rate (or increasing pressure or gas density in the plasma source), while T_g increased with increasing power and decreased with increasing flow rate. The thrust performance was also measured by developing a micro thrust stand with a combination of target and pendulum methods, giving a thrust in the range $F_t \approx 0.2 - 1.4$ mN, a specific impulse in the range $I_{sp} \approx 50 - 80$ s, and a thrust efficiency in the range $\eta_t \approx 2 - 12$ %. The thrust performance was found to increase with the discharge on and with increasing microwave power. These experimental results were consistent with those of numerical analysis, depending on microwave power and gas flow rate. The micro plasma thruster presently developed would be applicable to attitude-control and station-keeping maneuver for microspacecraft of < 10 kg.

Chapter 3

Light-mass propellants

3.1 Introductory remarks

Previously, we carried out a comprehensive numerical and experimental investigation of the microplasma generation, micnozzle flow, and thrust performance with working or propellant gas of argon (Ar) [70]. Then, a thrust of > 1 mN was demonstrated with 4.0-GHz microwaves of several W, while the specific impulse remained relatively low (< 100 s), and so the advantage was not sufficient over micro chemical propulsion. This chapter presents a study of the microwave-excited microplasma thruster with hydrogen (H_2) and helium (He) as a propellant. In practice, H_2 and He are often employed for plasma thrusters of electrothermal type because of their light masses, which give a high specific impulse in conventional large-scale propulsion systems [71–73]. However, there have been few studies of the micropropulsion system with such light-mass propellants, since their high diffusivity and thermal conductivity might lead to significant thermal energy losses and so to no improvement of the thrust performance. The next section describes the numerical model and results for the microplasma generation and micronozzle flow with working gas of He. The model is concerned with the entire region through the microplasma source to micronozzle, to analyze the electromagnetic wave propagation, plasma evolution, gas/plasma flow evolution (from subsonic to supersonic), and thrust performance. Then, Sec. 3.3 gives the experimental setup and results with H_2 as well as He, where the plasma density and

gas temperature were measured in the plasma source region by optical emission spectroscopy, along with the thrust performance (thrust and specific impulse). A comparison between numerical and experimental results is made for He, and a difference in microplasma generation, micronozzle flow, and thrust performance is discussed between light (H_2, He) and heavy (Ar) propellant gases. Finally, Sec. 3.4 summarizes conclusions of this chapter.

3.2 Numerical analysis

3.2.1 Model

The numerical model presently employed has been detailed in our previous paper [70]. The model consisted of an electromagnetic module (EM) for microwave propagation in interacting with plasmas and a fluid module (FM) for plasma flows with two (electron and heavy particle) temperatures. The former employed the finite difference time-domain (FDTD) approximation, being applied to the microplasma source region, to analyze the microwave power absorbed in the plasma. The latter employed two-temperature fluid equations, being applied to the entire region through the microplasma source to micronozzle (or through subsonic to supersonic), to analyze the plasma and nozzle flow characteristics. Gas-phase reaction processes were taken into account in both regions along with plasma-wall interactions in a limited space, and the analysis of the nozzle flow finally gave the thrust performance achieved. The numerical analysis relied on the azimuthally symmetric coordinate system [two-dimensional (2D) r-z system, $\partial/\partial\theta = 0$] assuming that: (i) the plasma is a two-phase medium consisting of electrons and heavy particles (ions and neutrals), and the temperature of electrons is different from that of heavy particles [$T_e \neq T_h (= T_i = T_n)$]. (ii) The plasma is macroscopically quasi-neutral, or the electron density equals that of ions ($n_e = n_i$). (iii) The atomic processes in the gas phase are electron-impact excitation/de-excitation and ionization/recombination, taking into account metastables as well as ground-state atoms. (iv) The charged particles (ions and electrons) diffuse toward the walls

according to the ambipolar diffusion. (v) The sheath structures are neglected at the plasma-wall interfaces. (vi) The gas/plasma flow is laminar, and the convective velocity $\boldsymbol{v}$ is the same for all species (electrons and heavy particles). (vii) In the microplasma source, moreover, the microwave energy is absorbed by plasma electrons, which in turn, is transferred to heavy particles through elastic collisions between them.

The EM module for the microplasma source consists of Maxwell's equations for electromagnetic fields of microwaves and equations for plasma electrons (neglecting the Lorentz force and pressure gradient):

$$\nabla \times \boldsymbol{E} = -\frac{\partial \boldsymbol{B}}{\partial t}, \tag{3.1}$$

$$\nabla \times \boldsymbol{B} = \mu_0 \left(\boldsymbol{j} + \epsilon_\mathrm{r} \epsilon_0 \frac{\partial \boldsymbol{E}}{\partial t} \right), \tag{3.2}$$

$$m_\mathrm{e} \frac{\partial \boldsymbol{u}_\mathrm{e}}{\partial t} = -e\boldsymbol{E} - m_\mathrm{e} \nu_\mathrm{e} \boldsymbol{u}_\mathrm{e}, \tag{3.3}$$

$$\boldsymbol{j} = -e n_\mathrm{e} \boldsymbol{u}_\mathrm{e}, \tag{3.4}$$

where $\boldsymbol{E}$ and $\boldsymbol{B}$ are the electric and magnetic fields of microwaves, respectively, $\boldsymbol{j}$ the plasma current density induced by microwaves, ϵ_0 the electric permittivity of vacuum, ϵ_r the relative permittivity, μ_0 the magnetic permeability of vacuum, e the magnitude of electron charge, m_e the mass of electron, $\boldsymbol{u}_\mathrm{e}$ the electron mean velocity driven by microwaves, ν_e the effective momentum transfer collision frequency between electrons and heavy particles, and n_e the plasma electron density. Assuming the azimuthal symmetry of the configuration, only the transverse magnetic waves exist in the plasma chamber with $\boldsymbol{E} = (E_r, 0, E_z)$ and $\boldsymbol{B} = (0, B_\theta, 0)$.

The transverse electromagnetic waves are injected into the system at the excitation plane (1.2 mm upstream of the end of the coaxial cable), and the total power injected into the chamber is monitored thereat by using

$$P_\mathrm{in} = \frac{1}{\mu_0} \int_A (\boldsymbol{E} \times \boldsymbol{B}) dA, \tag{3.5}$$

where A is the cross section concerned. The boundary conditions for the EM equations are the same as those in Ref. [70], including Mur's first-order absorbing

boundary condition applied to the field component E_r at the left end of the coaxial cable (0.8 mm further upstream of the excitation plane). In addition, the total absorbed power in the plasma is calculated as

$$P_{\mathrm{abs}} = \int_V Q_{\mathrm{abs}} dV = \int_V \left(\frac{1}{t_{\mathrm{p}}} \int_{t_{\mathrm{p}}} \boldsymbol{j} \cdot \boldsymbol{E} dt \right) dV, \tag{3.6}$$

assuming that the power absorption $\boldsymbol{j} \cdot \boldsymbol{E}$ in the plasma arises only from the classical Ohmic heating of electrons, where t_{p} is the period of the electromagnetic waves and Q_{abs} is the time-averaged power density absorbed. The spatially averaged power density absorbed per unit volume is then obtained from $\bar{Q}_{\mathrm{abs}} = P_{\mathrm{abs}}/V$ with the plasma volume V.

The FM module for the microplasma source and micronozzle consists of two-temperature Navier-Stokes equations and the equation of state for a two-phase medium consisting of electrons and heavy particles (ions and neutrals):

$$\frac{\partial}{\partial t}\rho + \nabla \cdot (\rho \boldsymbol{v}) = 0, \tag{3.7}$$

$$\frac{\partial}{\partial t}(\rho \boldsymbol{v}) + \nabla \cdot (\rho \boldsymbol{v}\boldsymbol{v}) = -\nabla p + \nabla \boldsymbol{\tau}, \tag{3.8}$$

$$\frac{\partial}{\partial t} n_{\mathrm{e}} + \nabla \cdot (n_{\mathrm{e}} \boldsymbol{v}) = \nabla \cdot (D_{\mathrm{a}} \nabla n_{\mathrm{e}}) + \dot{n_{\mathrm{e}}}, \tag{3.9}$$

$$\frac{\partial}{\partial t} n_{*} + \nabla \cdot (n_{*} \boldsymbol{v}) = \nabla \cdot (D_{*} \nabla n_{*}) + \dot{n_{*}}, \tag{3.10}$$

$$\frac{\partial}{\partial t}\left(\frac{3}{2} n_{\mathrm{e}} k_{\mathrm{B}} T_{\mathrm{e}}\right) + \nabla \cdot \left(\frac{5}{2} n_{\mathrm{e}} k_{\mathrm{B}} T_{\mathrm{e}} \boldsymbol{v}\right) = (\boldsymbol{v} \cdot \nabla) p_{\mathrm{e}} - \nabla \cdot \boldsymbol{q}_{\mathrm{e}} + Q_{\mathrm{abs}} - Q_{\mathrm{elas}} - Q_{\mathrm{iz,ex}} - Q_{\mathrm{rad}}, \tag{3.11}$$

$$\frac{\partial}{\partial t}\left(\frac{3}{2} n_{\mathrm{h}} k_{\mathrm{B}} T_{\mathrm{h}}\right) + \nabla \cdot \left(\frac{5}{2} n_{\mathrm{h}} k_{\mathrm{B}} T_{\mathrm{h}} \boldsymbol{v}\right) = (\boldsymbol{v} \cdot \nabla) p_{\mathrm{h}} + \boldsymbol{\tau} : \nabla \boldsymbol{v} - \nabla \cdot \boldsymbol{q}_{\mathrm{h}} + Q_{\mathrm{elas}}, \tag{3.12}$$

$$p = p_{\mathrm{e}} + p_{\mathrm{h}} = n_{\mathrm{e}} k_{\mathrm{B}} T_{\mathrm{e}} + n_{\mathrm{h}} k_{\mathrm{B}} T_{\mathrm{h}} = n_{\mathrm{e}} k_{\mathrm{B}} (T_{\mathrm{e}} + T_{\mathrm{h}}) + n_{\mathrm{n}} k_{\mathrm{B}} T_{\mathrm{h}}. \tag{3.13}$$

Equation (3.7) gives the overall mass continuity, where $\boldsymbol{v}$ is the convective velocity, and the total mass density is expressed as $\rho = m_{\mathrm{e}} n_{\mathrm{e}} + m_{\mathrm{h}} n_{\mathrm{h}} \approx m_{\mathrm{h}} n_{\mathrm{h}}$ with the mass m_{h} ($= m_{\mathrm{i}} = m_{\mathrm{n}}$) and density n_{h} ($= n_{\mathrm{i}} + n_{\mathrm{n}} \approx n_{\mathrm{e}} + n_{\mathrm{n}}$) of heavy particles. Equation (3.8) gives the overall momentum conservation, where p is the pressure, and $\boldsymbol{\tau}$ is the stress tensor expressed as $\tau_{ij} = \eta\left(\frac{\partial v_i}{\partial x_j} + \frac{\partial v_j}{\partial x_i}\right) - \frac{2}{3}\eta \delta_{ij} \frac{\partial v_k}{\partial x_k}$ with the viscosity η and Kronecker delta δ_{ij}. Equation (3.9) gives the conservation of electrons,

Table 3.1: Inelastic electron collision processes used in the simulation (H_j is the excitation/de-excitation energy of the reaction j).

No.	Process	Reaction	H_j (eV)	Ref.
R1	Ground state ionization	$He + e \rightarrow He^+ + 2e$	24.6	[79–81]
R2	Ground state excitation	$He + e \rightarrow He^* + e$	19.8	[79–81]
R3	Step-wise ionization	$He^* + e \rightarrow He^+ + 2e$	4.8	[82–84]
R4	Three-body recombination	$He^+ + 2e \rightarrow He + e$	−24.6	—
R5	Superelastic collision	$He^* + e \rightarrow He + e$	−19.8	—
R6	Two-body recombination	$He^+ + e \rightarrow He^* + (h\nu)$	−4.8	—

where D_a is the ambipolar diffusion coefficient and $\dot{n}_\mathrm{e}$ is the source term for production/destruction of plasma electrons. Equation (3.10) gives the conservation of He^* metastables, where n_* is the density of He^* atoms (the neutral density is $n_\mathrm{n} = n_\mathrm{g} + n_*$ with the density n_g of ground-state He atoms), D_* the diffusivity of He^* in He, and $\dot{n}_*$ the source term for production/destruction of He^*. Equations (3.11) and (3.12) give the energy conservation of electrons and heavy particles, respectively, where k_B is the Boltzmann constant, p_s is the pressure, q_s is the heat flux defined as $\boldsymbol{q}_s = -\kappa_s \nabla T_s$ with the thermal conductivity κ_s, and Q_abs is the absorbed power density of microwaves in the plasma source region ($Q_\mathrm{abs} = 0$ in the nozzle). Here, the subscript $s = \mathrm{e}, \mathrm{h}$ indicates electrons or heavy particles. Moreover, Q_elas denotes the energy exchange due to elastic collision between electrons and heavy particles, $Q_\mathrm{iz,ex}$ is the energy exchange due to the excitation/de-excitation and ionization/recombination as listed in Table 3.1, and Q_rad is the radiative energy loss. The electron viscous dissipation is neglected because of its small effect as compared with other terms in the equation. Finally, Eq. (3.13) gives the equation of state.

In these FM equations, the transport coefficients (η, D_a, D_*, κ_s) were taken from Refs. [74–76], and the energy exchange term (Q_elas) due to elastic collisions was from Refs. [77, 78]. In the terms concerned with inelastic collision processes ($\dot{n}_\mathrm{e}, \dot{n}_*, Q_\mathrm{iz,ex}, Q_\mathrm{rad}$), the ionization and excitation rates (for reactions R1 – R3 in Table 3.1) were taken from Refs. [78–84], and the rate coefficients for the reverse processes (R4 – R6) were determined from the so-called principle of detailed bal-

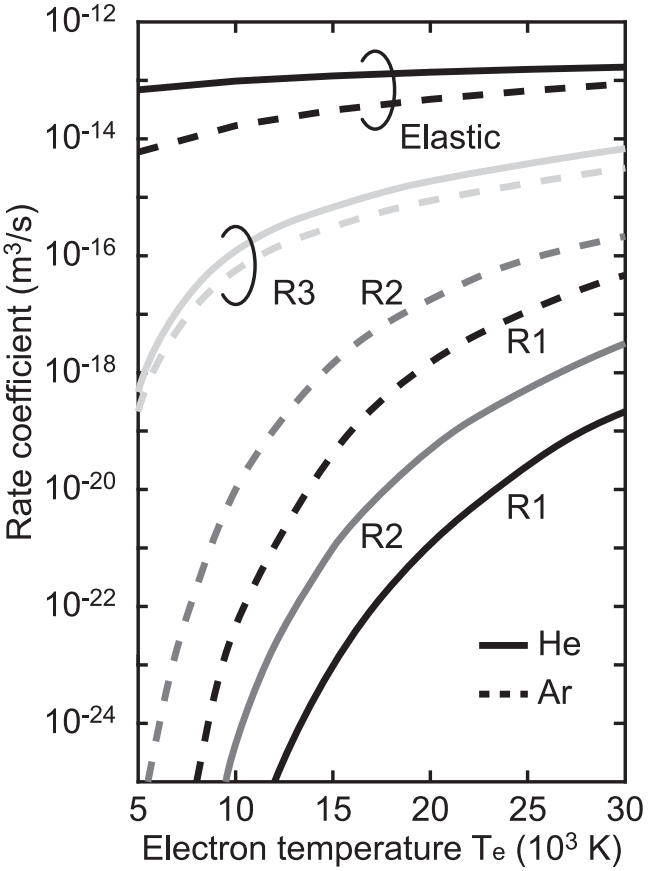

Figure 3.1: Rate coefficients for elastic and inelastic electron collision processes in He (solid lines, see Table 3.1) as a function of electron temperature T_e, together with those in Ar (dashed lines).

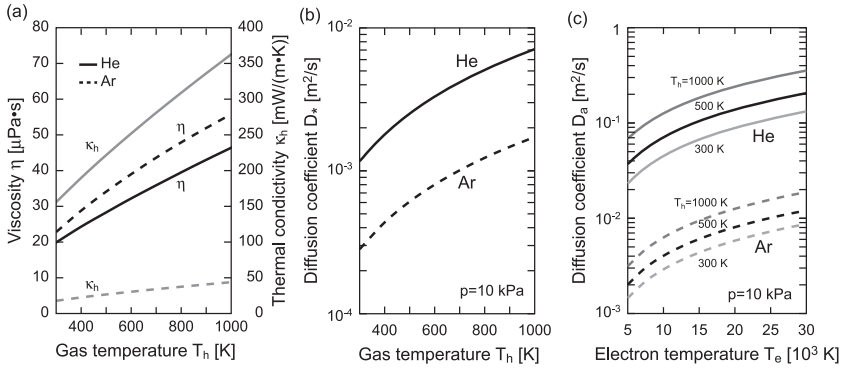

Figure 3.2: Transport coefficients for He (solid lines) as a function of (a), (b) gas or heavy particle temperature T_h and (c) electron temperature T_e, together with those for Ar (dashed lines): (a) viscosity η and thermal conductivity κ_h, (b) diffusion coefficient D_* for metastables, and (c) ambipolar diffusion coefficient D_a for ions and electrons, where $p = n_\mathrm{g} k_\mathrm{B} T_\mathrm{h}$ denotes the gas pressure.

ance. The rate coefficients for elastic momentum-transfer and forward reactions (R1 – R3) in He are shown in Fig. 3.1 as a function of electron temperature T_e, together with those in Ar. It is noted here that the rate coefficient for electron impact ionization of metastable He^* atoms (R3) appears to be large in Refs. [79–81], in view of the cross section for electron impact ionization of metastable He^* and Ar^* atoms in Refs. [82–84]; thus, we took the rate coefficient for metastable ionization (R3) in He that is five times smaller than that given in Refs. [79–81]. The ionization (R1) and excitation (R2) rate coefficients for He are two – three orders of magnitude smaller than those for Ar, while the elastic momentum-transfer rate coefficient is larger than that for Ar. These differences would lead to a significantly lower plasma and metastable densities in He plasma, compared with those in Ar plasma, while the plasma electron temperature would remain almost unchanged. The transport coefficients are also shown in Fig. 3.2 as a function of gas or heavy particle temperature T_h and electron temperature T_e (see Ref. [70] for the source of the data on Ar in Figs. 3.1 and 3.2). The thermal conductivity and diffusion coefficient for He are $\sim$ ten times higher than those for Ar, while the viscosity for He is relatively similar to that for Ar. Thus, the thermal loss and the loss of

plasma prticles (ions, electrons, metastables) to chamber walls are expected to be more significant in He plasma, while the viscous dissipation in boundary layers is expected to remain relatively unchanged. The boundary conditions for the FM equations are the same as those in Ref. [70]. The heavy particle temperature T_h at the interfaces was assumed to be isothermal with a wall temperature T_w = 500 K in the plasma source region, and the radiative wall condition was employed for T_h in the nozzle region.

The numerical procedures have also been detailed in our previous paper [70]. Briefly, in the EM module for the microplasma source, Eqs. (2.1) – (2.4) were solved by using the FDTD approximation. In the FM module for the microplasma source and micronozzle, Eqs. (2.9) – (2.15) were all discretized in a finite difference manner, and the discrete equations were solved by using an implicit lower-upper symmetric Gauss-Seidel scheme (LU-SGS) [58] . A self-consistent solution was obtained by applying the different timescale integration to the two modules of EM and FM, where the procedures were repeated until the plasma and fluid properties converged in the entire region of plasma source and nozzle to finally also give the thrust performance.

3.2.2 Numerical results

Figures 3.3(a) – 3.3(h) show the spatial distribution of the electron density n_e, electron temperature T_e, heavy particle temperature T_h, absorbed power density Q_{abs}, pressure p, axial flow velocity u, He gas or ground-state density n_g ($\rho \approx m_h n_g$), and He* metastable-state density n_* in the microplasma source, respectively, calculated for an input power P_{in} = 6.0 W of f = 4 GHz microwaves, He mass flow rate $\dot{m}$ = 0.15 mg/s (flow rate of 50 sccm), and quartz chamber and envelope ($\epsilon_r = \epsilon_d$ = 3.8). The absorbed power calculated in the plasma is P_{abs} = 4.5 W in total, corresponding to the average power density $\bar{Q}_{abs} = 5.7 \times 10^8$ W/m^3. The plasma electron density n_e and temperature T_e exhibit their maxima near the end of the dielectric envelope of the antenna ($n_e \approx 1.8 \times 10^{19}$ m^{-3}, $T_e \approx 2.0 \times 10^4$ K), which is consistent with the distribution of the absorbed power density Q_{abs}.

On the other hand, the heavy particle temperature T_h exhibits its maximum in a space between the end of the dielectric envelope and the end wall of the dielectric plasma source chamber ($T_h \approx 650$ K), where the micronozzle is located to achieve the aerodynamic acceleration of high temperature plasmas through supersonic expansion into vacuum. In addition, the pressure calculated is almost uniform in the plasma source ($p \approx 10$ kPa), and the flow velocity is increased in the axial direction toward the end of the source region (up to $u \approx 60$ m/s).

A comparison with numerical results for Ar [70] indicates that the electron n_e and metastable n_* densities in He plasma are one – two orders of magnitude lower than those in Ar plasma, because of smaller ionization and excitation rate coefficients and larger diffusion coefficients for He. The electron temperature T_e and absorbed power density Q_{abs} are locally a little higher in He than in Ar plasmas; however, in contrast to Ar, T_e in He is substantially decreased towards the end of the source chamber or the nozzle inlet, owing to more significant energy loss due to elastic and inelastic collisions between electrons and heavy particles in He. The heavy particle temperature T_h in He plasma is only a little lower than that in Ar plasma ($T_h \approx 890$ K in Ar [70]); this is attributed primarily to a more significant thermal energy gain due to elastic collisions between electrons and heavy particles in He as compared to that in Ar, which tends to offset a more significant thermal energy loss due to the higher thermal conductivity in He. Moreover, the flow velocity u in He plasma is two – five times larger than that in Ar plasma, and correspondingly, the pressure p and gas density n_g are significantly lower in He than in Ar, because u in the plasma source region is governed by the choking ($Ma = u/a = 1$) at the nozzle throat; in effect, the sonic speed $a = (\gamma k_B T_h/m_h)^{1/2}$ of He is higher than that of Ar, where $\gamma = 5/3$ denotes the specific heat ratio for monoatomic gases.

Also shown in Figs. 3.3(i) and 3.3(j) are snapshots of the distribution of the radial E_r and axial E_z electric fields of microwaves. The corresponding extended views of the electric fields in the dielectric as well as in the plasma are also shown in Figs. 3.4(a) and 3.4(b). These results are similar in part to those for Ar [70], in-

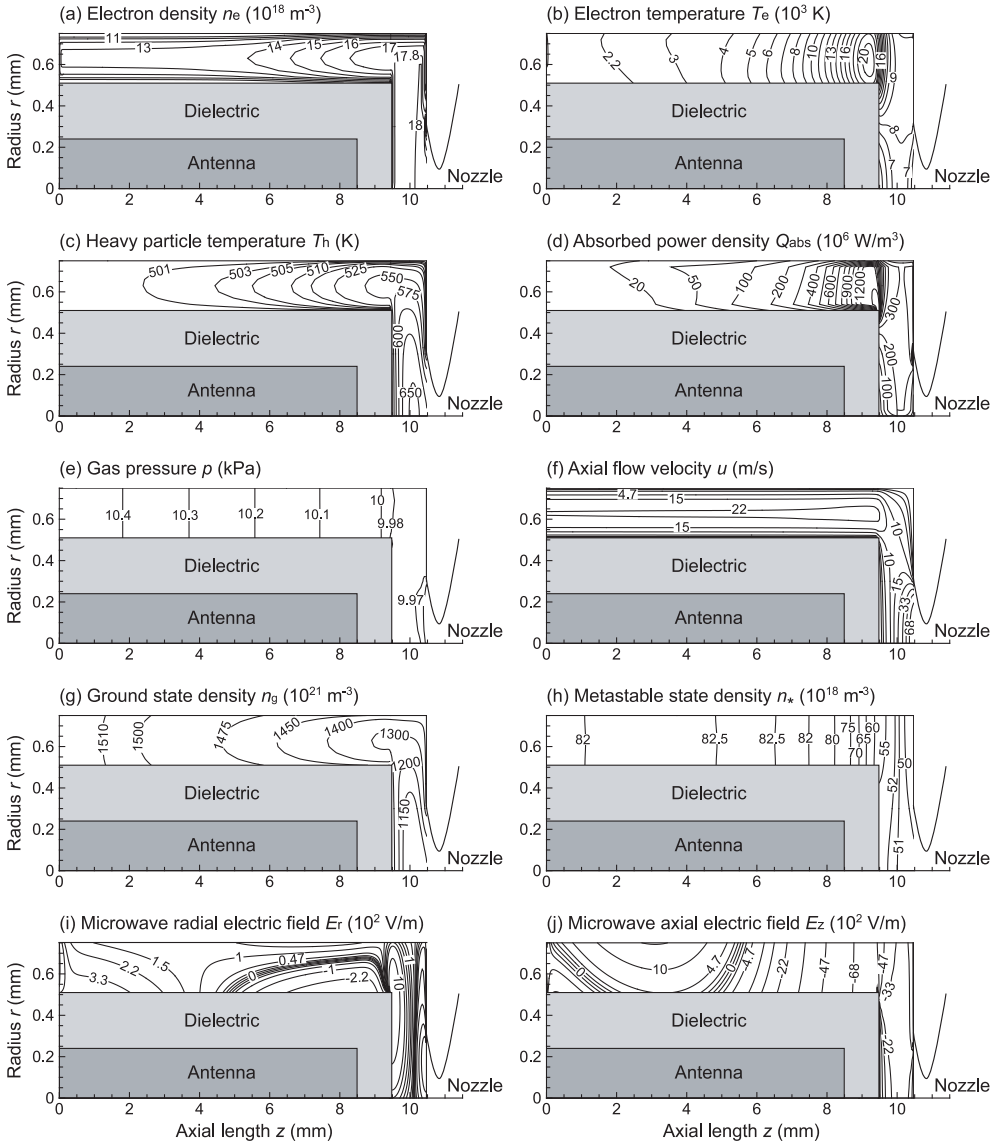

Figure 3.3: Distribution of the (a) electron density n_e, (b) electron temperature T_e, (c) heavy particle temperature T_h, (d) absorbed power density Q_{abs}, (e) gas pressure p, (f) axial flow velocity u, (g) He gas or ground-state density n_g, and (h) He* metastable-state density n_* in the microplasma source, calculated for an input power P_{in} = 6.0 W of f = 4 GHz microwaves, He mass flow rate $\dot{m}$ = 0.15 mg/s (flow rate of 50 sccm), and quartz chamber and envelope (ϵ_d = 3.8). The microwave power absorbed in the plasma was calculated as P_{abs} = 4.5 W. Also shown is a snapshot of the distribution of the (i) radial E_r and (j) axial E_z electric fields of microwaves in the microplasma region.

dicating that the strength of E_r is more than ten times smaller than that of E_z in the plasma, while the former is about ten times larger than the latter in the dielectric. Moreover, the peak position of the absorbed power density $Q_{\rm abs}$ in the plasma corresponds to that of E_z (not E_r), implying that the axial E_z is the major component of microwave electric fields that contributes to $Q_{\rm abs}$ and thus to $P_{\rm abs}$. The present numerical analysis gives a high absorption efficiency $P_{\rm abs}/P_{\rm in} \approx 75$ % in He (> 80 % in Ar [70]), which is ascribed to the localized absorption of microwaves or inhomogeneous heating of electrons in the interaction of electromagnetic waves with nonuniform plasmas. However, it should be noted here that the present results for He show no significant characteristic of surface wave-excited plasmas as can be seen in the case of Ar [70], where the strength E_z in the plasma is largest near the plasma-dielectric interfaces, further increasing with increasing axial distance downstream toward the end of the antenna or dielectric envelope. This is attributed to the lower plasma electron densities $n_{\rm e}$ in He, which do not satisfy the conditions for surface waves [54]; in practice, the surface wave is assumed to propagate in a thin skin depth layer of thickness $\delta = c/\omega_{\rm pe}$ along the plasma-dielectric interfaces for densities $n_{\rm e} > n_{\rm cr}$. Here, c denotes the speed of light in vacuum, $\omega_{\rm pe} = (n_{\rm e}e^2/m_{\rm e}\epsilon_0)^{1/2}$ the plasma electron frequency, $n_{\rm cr} = (1 + \epsilon_{\rm d})n_{\rm c}$ the critical density for surface waves, and $n_{\rm c} = \epsilon_0 m_{\rm e}\omega^2/e^2$ the cutoff density for electromagnetic waves of frequency $f = \omega/2\pi$. In the case of He with typically $n_{\rm e} = 2 \times 10^{19}$ m^{-3} ($n_{\rm e} = 2 \times 10^{20}$ m^{-3} in Ar [70]), the frequency $f = 4$ GHz and dielectric constant $\epsilon_{\rm d} = 3.8$ give $n_{\rm cr} = 9.1 \times 10^{17}$ m^{-3} and $\delta = 1.2$ mm ($\delta = 0.38$ mm in Ar); thus, in He, $\delta > R_{\rm c}$ while $n_{\rm e} > n_{\rm cr}$, where $R_{\rm c} = (d_{\rm d,out} - d_{\rm d,in})/2 = 0.24$ mm is the characteristic radial length of the plasma presently concerned.

Figures 3.5(a) – 3.5(h) show the distribution of the electron density $n_{\rm e}$, electron temperature $T_{\rm e}$, heavy particle temperature $T_{\rm h}$, Mach number $Ma = |\boldsymbol{v}|/a$, pressure p, axial flow velocity u, He gas or ground-state density $n_{\rm g}$ ($\rho \approx m_{\rm h}n_{\rm g}$), and He* metastable-state density n_* in the micronozzle, respectively, obtained in the same numerical simulation as Figs. 3.3 and 3.4. The temperature $T_{\rm h}$, Mach number Ma, pressure p, flow velocity u, and gas $n_{\rm g}$ and metastable n_* densities exhibit

a characteristic of the subsonic-supersonic flow or aerodynamic acceleration of flow in the converging-diverging nozzle: Ma and u increase with increasing axial distance, with $Ma = 1$ being at around the throat, while T_h, p, n_g, and n_* decrease downstream along the nozzle axis. However, the contour of T_h, Ma, and u indicates that the boundary layer associated with viscosity is relatively thick in the micronozzle, especially in the divergent or supersonic portion of the nozzle [61]. In practice, the flow velocity u is lower and the temperature T_h is higher closer to the nozzle walls in the diverging portion; moreover, the flow therein is supersonic ($Ma > 1$) around the nozzle axis, while subsonic ($Ma < 1$) near the walls over roughly half of the nozzle cross section. Note that the decrease of the temperature T_h along the nozzle axis is not so significant as compared to the change of Ma, p, u, n_g, and n_*, owing to heating due to viscous dissipation in thick boundary layers. It is further noted that the plasma density n_e decreases downstream along the nozzle axis, which is similar to the behavior of the pressure p and gas n_g and metastable n_* densities; on the other hand, the electron temperature T_e exhibits a substantial decrease along the axis, which is more significant as compared to the behavior of the temperature T_h.

A comparison with numerical results for Ar [70] indicates that the flow velocity u in the nozzle is more than two times larger in He than that in Ar, owing to the higher sonic speed of He, although the aerodynamic acceleration of the flow in He is not so strong as compared to that in Ar, owing to lower pressures p or gas densities n_g in the plasma source region in He. Moreover, the decrease of the electron temperature T_e downstream along the nozzle axis in He is significantly large as compared to that in Ar, primarily because of more significant energy loss due to elastic and inelastic collisions between electrons and heavy particles in He.

Figures 3.6 and 3.7 show the contour of plasma and flow properties in the microplasma source and micronozzle, respectively, for a reduced He mass flow rate of $\dot{m} = 0.059$ mg/s (flow rate of 20 sccm), calculated with the other parameters being the same as in Figs. 3.3 – 3.5. A comparison between Figs. 3.3 and 3.6 indicates that in the plasma source region, reducing the flow rate leads to a decrease

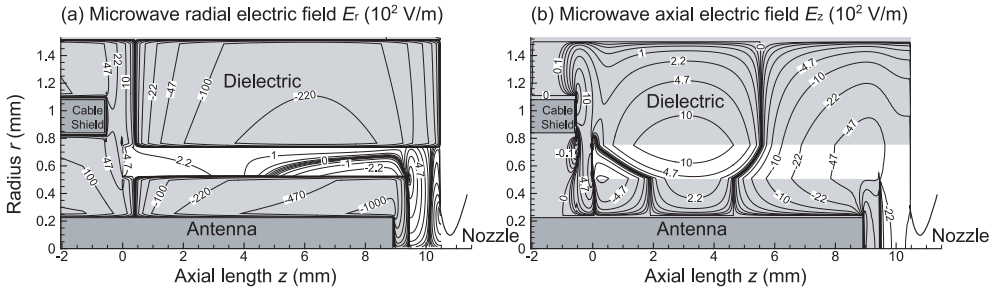

Figure 3.4: Extended view of a snapshot of the distribution of the (a) radial E_r and (b) axial E_z electric fields of microwaves in the microplasma source, corresponding to Figs. 3.3(i) and 3.3(j). The figure includes the region of coaxial cable for microwave injection and the region of dielectric materials containing the plasma. Note that the excitation plane for microwave injection in the numerical analysis is at $z = -1.2$ mm, and the boundary for Mur's first-order absorbing condition is at $z = -2$ mm.

in pressure p, flow velocity u, and gas n_g and metastable n_* densities, while the electron density n_e, temperature T_e, heavy particle temperature T_h, and absorbed power density Q_{abs} remain almost unchanged. A comparison between Figs. 3.5 and 3.7 indicates that at reduced flow rates, the aerodynamic acceleration of the flow in the nozzle is significantly reduced owing to lower pressures p or gas densities n_g in the plasma source region. These effects of reducing the flow rate are more significant for He, as can be seen from a comparison with numerical results for Ar [70], because the sonic speed of He is much higher than that of Ar. In practice, the micronozzle flow of He in Fig. 3.7 remains almost subsonic, or the Mach number is $Ma < 1$, over almost the entire region of the nozzle, where a transition from subsonic to supersonic flow on axis occurs a little downstream of the throat (not at the nozzle throat) with the minimum T_h and the maximum Ma and u being inside the nozzle (not at the nozzle exit). Thus, it follows that viscous boundary layers next to the nozzle walls [69] impede the flow expansion in the micronozzle more significantly at reduced flow rates in He, where the nozzle flow is heavily underexpanded to decelerate the supersonic flow downstream along the axis in the diverging portion of the nozzle.

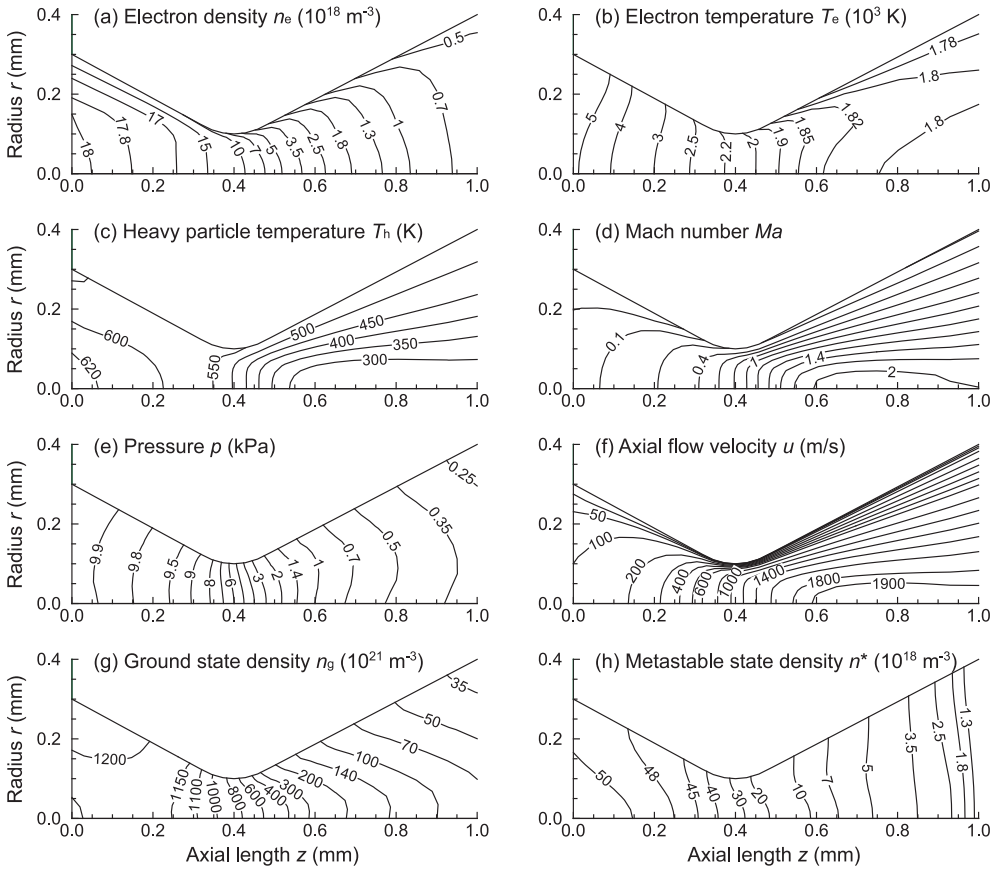

Figure 3.5: Distribution of the (a) electron density n_e, (b) electron temperature T_e, (c) heavy particle temperature T_h, (d) Mach number Ma, (e) pressure p, (f) axial flow velocity u, (g) He gas or ground-state density n_g, and (h) He* metastable-state density n_* in the micronozzle, obtained in the same numerical simulation as Figs. 3.3 and 3.4. The nozzle shown has an inlet, throat, and exit diameter of d_{in} = 0.6 mm, d_{th} = 0.2 mm, and d_{ex} = 0.8 mm, respectively, with a diverging angle of $\theta = 26.6^\circ$ and a total length of 1 mm.

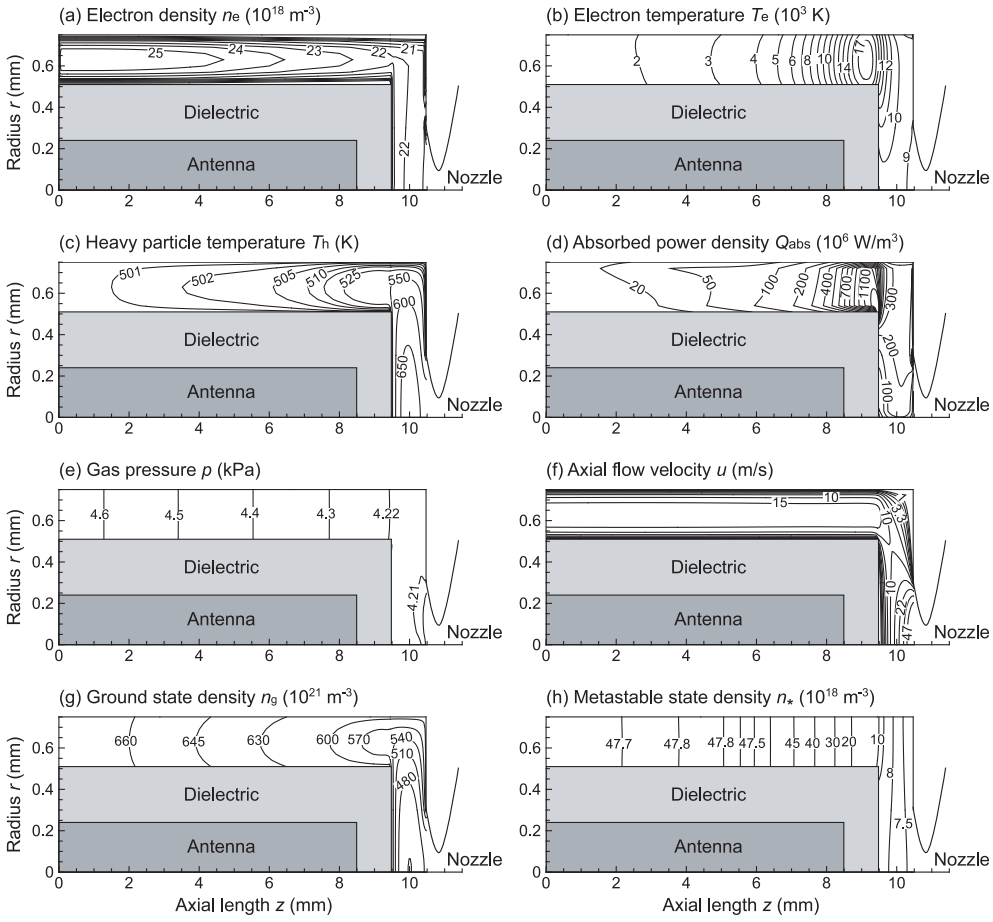

Figure 3.6: Distribution of the (a) electron density n_e, (b) electron temperature T_e, (c) heavy particle temperature T_h, (d) absorbed power density Q_{abs}, (e) gas pressure p, (f) axial flow velocity u, (g) He gas or ground-state density n_g, and (h) He* metastable-state density n_* in the microplasma source for a He mass flow rate $\dot{m}$ = 0.059 mg/s (or a flow rate of 20 sccm), calculated with the other parameters being the same as Figs. 3.3 – 3.5. The microwave power absorbed in the plasma was calculated as P_{abs} = 4.4 W.

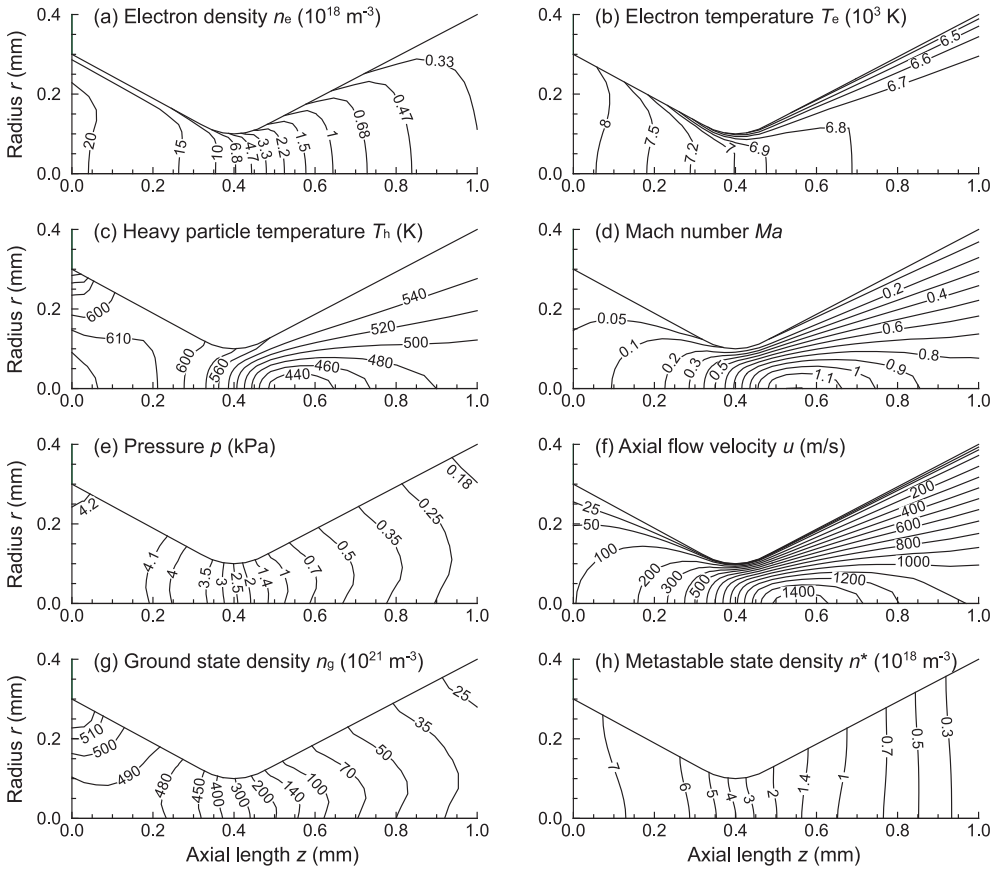

Figure 3.7: Distribution of the (a) electron density n_e, (b) electron temperature T_e, (c) heavy particle temperature T_h, (d) Mach number Ma, (e) pressure p, (f) axial flow velocity u, (g) He gas or ground-state density n_g, and (h) He* metastable-state density n_* in the micronozzle, obtained in the same numerical simulation as Fig. 3.6.

3.3 Experiment

3.3.1 Experimental setup

The experimental setup has been detailed in our previous paper [70]. The microplasma source chamber was made of a quartz tube (ϵ_d = 3.8) L_s = 10.5 mm long, $d_{s,in}$ = 1.5 mm in inner diameter, and $d_{s,out}$ = 3.0 mm in outer diameter, which was similar to the configuration of the microplasma source shown in Figs. 3.3, 3.4, and 3.6. The center conductor of a semi-rigid coaxial cable, protruding 10 mm beyond the insulator and outer conductor, was covered with a dielectric envelope, which was then inserted in the source chamber as a microwave antenna L_{an} = 8.5 mm long and d_{an} = 0.5 mm in diameter. The dielectric envelope of quartz (ϵ_d = 3.8) covering the antenna was L_d = 9.5 mm long, $d_{d,in}$ = 0.5 mm in inner diameter, and $d_{d,out}$ = 1.0 mm in outer diameter. The plasma source chamber and antenna were inserted into a stainless-steel housing to cover the microplasma source with a metal grounded, where an annular spacing was retained for feeding the propellant gas. The microplasma source thus configured was located in a vacuum chamber pumped down by a dry and turbomolecular pump.

Microwave signals of f = 4 GHz from a signal generator were amplified through a four-stage semiconductor amplifier to powers of nominally $P_{in} < 10$ W, and then fed into the microplasma source through the semi-rigid coaxial cable, where a miniature three-stub tuner was used to suppress the reflection of microwaves. The propellant or working gas was He and H_2 in this study, being supplied through a mass flow controller; in some cases, a small amount (< 1 %) of N_2 and H_2 was added for plasma diagnostics. The gas pressure p_0 (= $p \approx n_g k_B T_h$) in the microplasma source was measured by a pressure gauge set upstream of the source chamber. The micronozzle of converging-diverging type was fabricated in a 1-mm-thick quartz plate, having an inlet, throat, and exit diameter of d_{in} = 0.6, d_{th} = 0.2, and d_{ex} = 0.8 mm, respectively, which was similar to the nozzle configuration shown in Figs. 3.5 and 3.7; the micronozzle was attached to the end of the microplasma source chamber. It is noted here that the gas flow rate (or

mass flow rate $\dot{m}$) and the source pressure p_0 measured with and without plasma discharge were approximately related by the quasi-one-dimensional nozzle flow equation for an isentropic flow of perfect gas [60, 61, 69, 70], assuming the source temperature T_0 ($\approx T_\mathrm{h}$) to be the room temperature in cold gas operation and the gas temperature spectroscopically measured in plasma discharge.

To characterize the microplasma concerned, the optical emission from the plasma was observed in the side-view direction through a 1-mm-diam small hole of the stainless-steel housing at around the end of the antenna or dielectric envelope (just upstream of the micronozzle inlet) [70]. A 50-cm focal length spectrograph/monochromator was employed in these experiments, with a grating of 2400 lines/mm and charge-coupled device (CCD) detector, where a set of lenses was used to collect the emission from the plasma and focus it on the entrance slit of the spectrometer. The spectral resolution, determined using a low-pressure Ar discharge lamp, was 0.025 nm with an entrance slit width of 5 μm.

3.3.2 Plasma characteristics

The analysis of optical emissions from the plasma has been detailed in our previous paper [70]. The plasma electron density was measured by analyzing the Stark broadening of the H Balmer-β (H_β) spectral line at 486.1 nm, where a small amount (< 1 %) of H_2 was added in the case of He. The H_β line broadening is generally appreciated to consist of the instrumentation $\Delta\lambda_\mathrm{instrum}$, Doppler $\Delta\lambda_\mathrm{Doppler}$ (depending on gas temperature T_g), pressure $\Delta\lambda_\mathrm{pressure}$ (depending on T_g and p_0 or gas density n_g), and Stark $\Delta\lambda_\mathrm{Stark}$ broadening (depending on n_e and T_e) [62, 63, 65, 70]; the former two are given by the Gaussian profile and the latter two by the Lorenzian profile, which are then approximated by the Voigt function in total with a full width at half maximum (FWHM) of $\Delta\lambda_\mathrm{V}$ (typically, $\Delta\lambda_\mathrm{V} \approx 0.05 - 0.06$ nm in the present experiments). The accuracy of the electron density determined from the Stark broadening relies on the spectral resolution of the measurement system and also on the assumption of analysis of the spectral line broadening; in practice, the present accuracy was estimated to be about $\pm$ 20 %, primarily owing to the

resolution $\Delta\lambda_{\mathrm{instrum}} \approx 0.025$ nm of the spectrometer system employed. Moreover, the gas/rotational temperature was measured by adding a small amount (< 1 %) of N_2 and analyzing the vibronic spectrum of the N_2 2nd positive (0,2) band at 380.4 nm.

Figures 3.8 and 3.9 show the plasma electron density n_e and gas/rotational temperature $T_g \approx T_{rot}$ measured as a function of He and H_2 gas flow rates, respectively, for different microwave input powers P_{in}, where changing the flow rate led to a change in pressure p_0 or gas density n_g in the microplasma source as in Ref. [70]. The electron density was in the range $n_e \approx (2-5) \times 10^{19}$ m^{-3}, and the gas temperature was in the range $T_g \approx T_{rot} \approx 600-700$ K in He discharges of Fig. 3.8, where n_e was about five times lower and T_g was a little lower than those in Ar discharges [70]. The temperature $T_g \approx T_{rot}$ was observed to increase with increasing P_{in} and to decrease with increasing flow rate (or with increasing p_0 or n_g in the plasma source). On the other hand, the density n_e was observed to increase with increasing P_{in} and to remain almost unchanged by varying the flow rate. Also shown in Fig. 3.8 are the curves of n_e and T_g (= T_h) numerically simulated as in Figs. 3.3 and 3.6, indicating that the experiments were in agreement with the numerical analysis, where the numerical data were line-averaged in the radial direction between the end of the microwave antenna or dielectric envelope and the inlet of the nozzle. Similar plasma characteristics were observed in H_2 discharges of Fig. 3.9, where the discharge could not be established under marginal conditions for sustaining the discharge (at high flow rates of > 15 sccm at P_{in} = 6 W and > 2.5 sccm at P_{in} = 3 W).

3.3.3 Thrust performance

The experimental setup for thrust measurement has been detailed elsewhere [45], which consisted of a pendulum-type stand for cold-gas operation and a target-type stand for both cold-gas and plasma-discharge operations. In the former, the thruster itself was hung; on the other hand, in the latter, a small concave cylindrical target block was hung downstream of the nozzle exit with the thruster

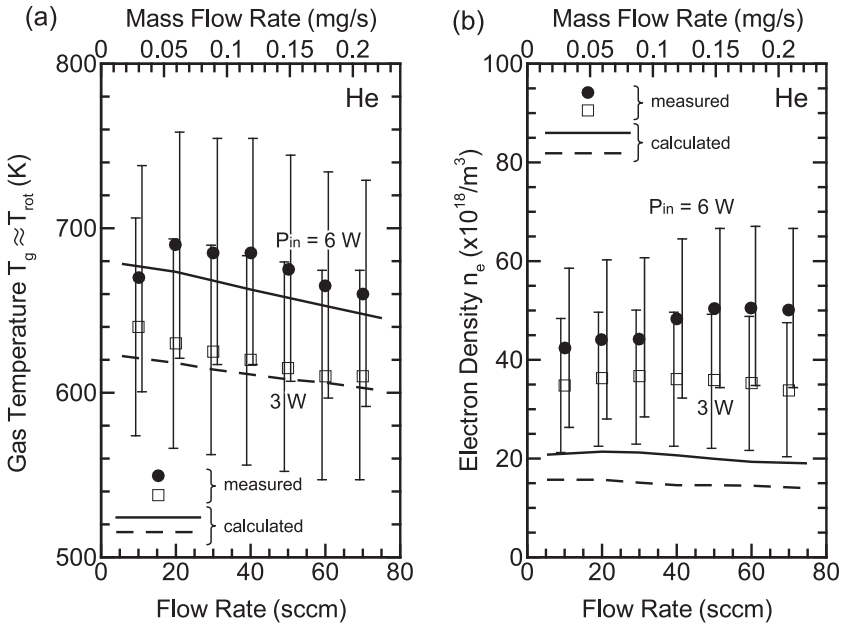

Figure 3.8: (a) Plasma electron density n_e and (b) gas temperature $T_g \approx T_{rot}$ measured as a function of He gas flow rate for different microwave powers P_{in}, where changing the flow rate led to a change in pressure p_0 in the microplasma source. These data were taken under conditions of $f = 4$ GHz and $\epsilon_d \approx 3.8$, with a small amount (0.05 sccm) of additive gases of N_2 in (a) and H_2 in (b). Also shown in the figure are the curves of n_e and T_g (= T_h) numerically simulated as in Figs. 3.3 and 3.6, where the data are those line-averaged in the radial direction between the end of the antenna or dielectric envelope and the inlet of the micronozzle.

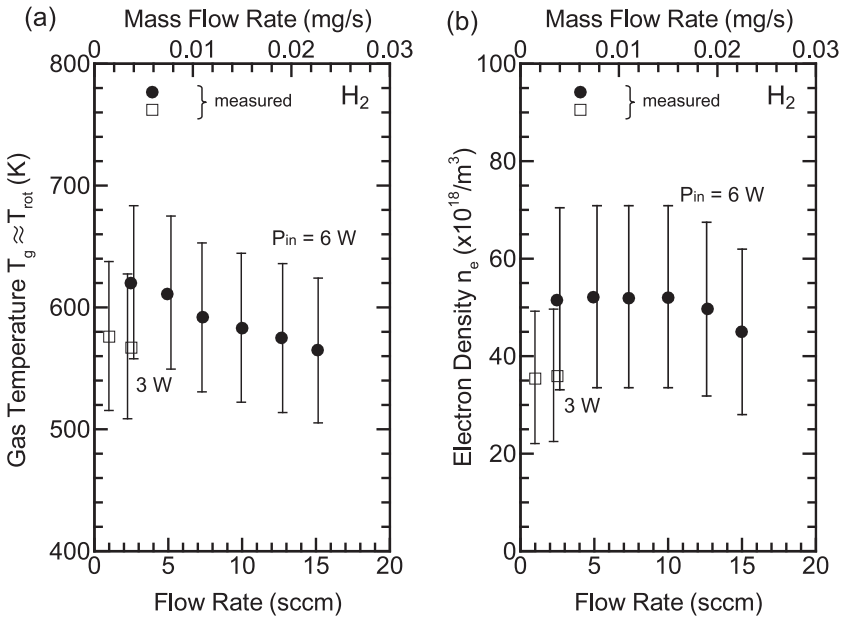

Figure 3.9: (a) Plasma electron density n_e and (b) gas temperature $T_g \approx T_{rot}$ measured as a function of H_2 gas flow rate for different microwave powers P_{in}, where changing the flow rate led to a change in pressure p_0 in the microplasma source. These data were taken under conditions of $f = 4$ GHz and $\epsilon_d \approx 3.8$, with a small amount (0.05 sccm) of additive gas of N_2 in (a).

being fixed tightly, and the gas/plasma plume ejected from the thruster struck the target mounted at one end of the pendulum with some weights being at the other end for balance. Here, the target employed was a small Faraday cup-like one made of poly-tetrafluoroethylene (PTFE), to suppress the effects of reflected particles of the jet plume striking the target. A small displacement of $\Delta X < 0.1$ mm in operation was measured by using a laser displacement gauge having a resolution of $\Delta x < 0.1\,\mu$m. The accuracy of the present thrust measurement was estimated to be about ± 10%, relying primarily on mechanical issues of the measurement system such as effects of friction of the knife edge on the rotational axis and effects of the reflected jet plume particles on the target.

Figures 3.10 and 3.11 show the thrust performance (thrust F_t, specific impulse I_{sp}) measured as a function of He and H_2 gas flow rates, respectively, for different microwave input powers P_{in}, where $P_{in} = 0$ W corresponds to the cold-gas operation without plasma discharge. The measurements showed that the thrust performance was enhanced with the discharge on and with increasing P_{in}; the thrust and specific impulse were typically $F_t \approx 0.51$ mN and $I_{sp} \approx 250$ s, respectively, with the thrust efficiency $\eta_t \approx 10.1\%$ at $P_{in} = 6$ W and a He flow rate of 70 sccm (0.21 mg/s). Also shown in He discharges of Fig. 3.10 are the curves of F_t and I_{sp} calculated based on the numerical analysis in Sec. 3.2 as in Ref. [70], indicating that the experiments were in agreement with the numerical analysis, where the thrust F_t was taken to consist of the momentum and pressure ones, and the temperature T_h was taken to be the room temperature in cold gas operation. It is further noted that the numerical efficiency was in the range $\eta_t \approx 2 - 12\%$ at $P_{in} \approx 3 - 6$ W and He flow rates of 10 – 70 sccm. Similar thrust performance was obtained in H_2 discharges of Fig. 3.11, where the specific impulse I_{sp} was more than 1.5 times higher than that in He, owing to a difference in mass between H_2 and He [61, 69].

Figure 3.12 shows a summary of the thrust performance (I_{sp} versus F_t) measured for different microwave powers P_{in} and flow rates with three different propellant gases, where the data for He and H_2 were taken from the preceding Figs.

3.10 and 3.11, respectively, and the data for Ar were taken from Fig. 14 of our previous paper [70]. It should be noted here that the specific impulse I_{sp} was higher with light-mass He and H_2 than with Ar, while the thrust F_t was larger with Ar than with He and H_2, and that the thrust performance was enhanced with the discharge on and with increasing P_{in} for all these different gases. Thus, it follows that in the microplasma thruster of electrothermal type, the high diffusivity and thermal conductivity of light-mass propellants do not lead to a deterioration of the thrust performance, although the surface-to-volume ratio is high for microplasma sources; in effect, in the present microplasma thruster, the specific impulse I_{sp} was found to be significantly enhanced with light-mass propellants of He and H_2 as compared to that with Ar, as has been known for large-scale propulsion systems [69]. This is attributed primarily to a more significant thermal energy gain due to elastic collisions between electrons and heavy particles in He and H_2 as compared to that in Ar, which tends to offset a more significant thermal energy loss due to the high diffusivity and thermal conductivity of light-mass He and H_2 in the microplasma source of high surface-to-volume ratios.

3.4 Conclusions

Microplasma thruster of electrothermal type has been investigated with feed or propellant gases of He and H_2. The thruster consisted of an azimuthally symmetric microwave-excited microplasma source and a converging-diverging micronozzle. The plasma source was made of a dielectric chamber 1.5 mm in diameter and 10 mm long covered with a metal grounded, having a metal rod antenna on axis covered with a dielectric envelope, which produced high temperature plasmas at around atmospheric pressures. The surface wave-excited plasmas were established by 4.0-GHz microwaves at powers of $P_{in} \leq 6$ W, with the source pressure in the range 2 – 13 kPa at flow rates of 5 – 70 sccm. The nozzle was also made of a dielectric, being 1 mm long with a throat 0.2 mm in diameter, which converted high thermal energy of plasmas into directional kinetic energy of super-

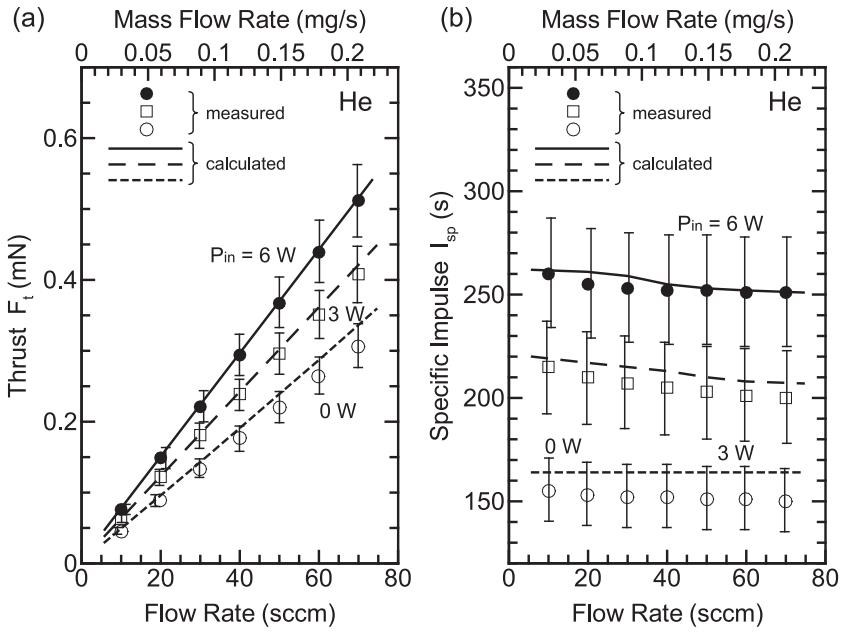

Figure 3.10: Thrust performance [(a) thrust F_t and (b) specific impulse I_{sp}] measured as a function of He gas flow rate for different microwave powers P_{in} under the same conditions as in Fig. 3.8 (f = 4 GHz, $\epsilon_d \approx 3.8$). Here, P_{in} = 0 W corresponds to the cold-gas operation without plasma discharge. Also shown in the figure are the curves of F_t and I_{sp} calculated from the numerical analysis as in Figs. 3.5 and 3.7.

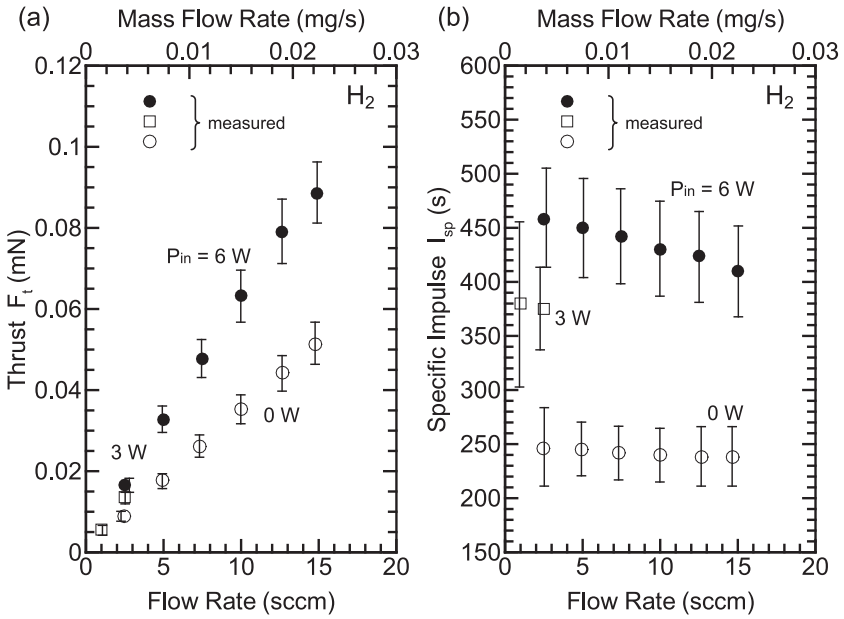

Figure 3.11: Thrust performance [(a) thrust F_t and (b) specific impulse I_{sp}] measured as a function of H_2 gas flow rate for different microwave powers P_{in} under the same conditions as in Fig. 3.9 (f = 4 GHz, $\epsilon_d \approx 3.8$). Here, P_{in} = 0 W corresponds to the cold-gas operation without plasma discharge.

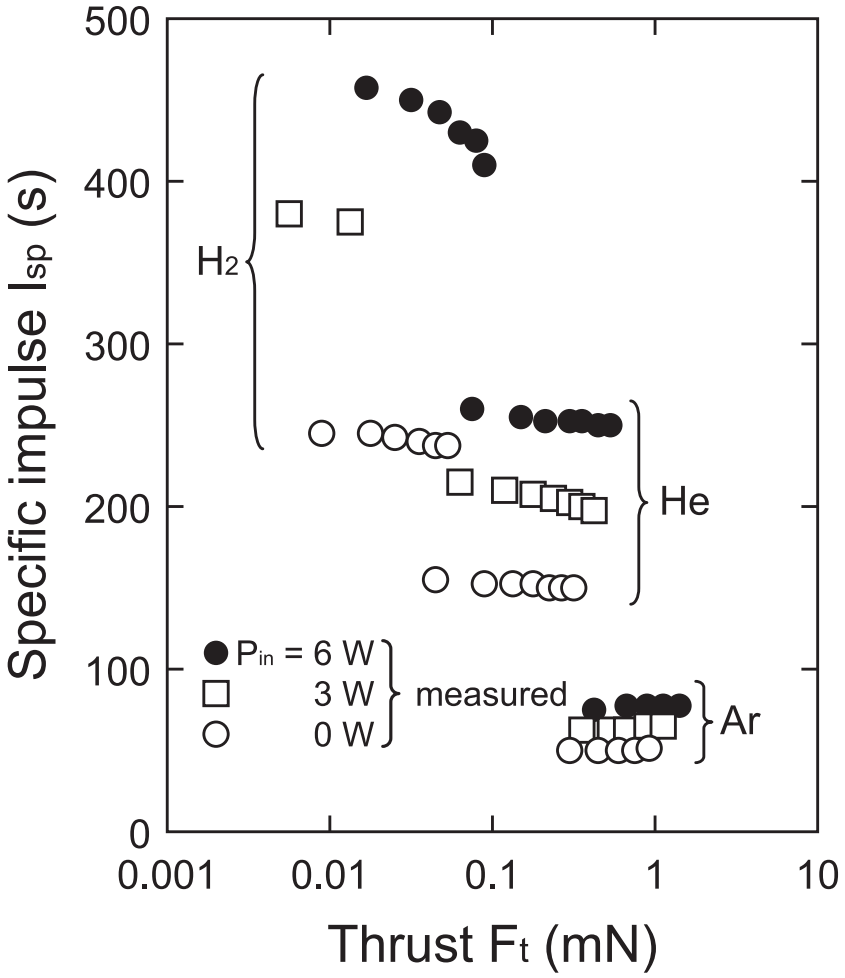

Figure 3.12: Thrust F_t versus specific impulse I_{sp} measured for different microwave powers P_{in} and gas flow rates with three different propellant gas. The data for He and H_2 were taken from the preceding Figs. 3.10 and 3.11, respectively, and the data for Ar were from Fig. 14 of our previous paper [70].

sonic plasma flows to obtain the thrust. The microplasma generation, micronozzle flow, and thrust performance with He was numerically analyzed by using a two-dimensional fluid model over the entire region through the mocroplasma source to the micronozzle, coupled with an electromagnetic model for microwaves interacting with plasmas in the source region. The numerical results indicated that in the micronozzle, viscous boundary layers next to the nozzle walls impede the flow expansion, especially at reduced flow rates, where the supersonic flow is heavily decelerated to subsonic downstream along the axis in the diverging portion of the nozzle.

In experiments, the plasma electron density and gas temperature in the microplasma source at around the top of the microwave antenna, or just upstream of the micronozzle inlet, were measured by optical emission spectroscopy with a small amount of additive gases of H_2 and N_2. In the case of He propellant, the Stark broadening of H Balmer-β line and the vibronic spectrum of N_2 2nd positive (0, 2) band indicated that the electron density was in the range $n_e \approx (2-5) \times 10^{19}$ m^{-3} and the gas or rotational temperature was in the range $T_g \approx T_{rot} \approx 600 - 700$ K. The thrust performance was also measured by using a target-type microthrust stand, giving a thrust in the range $F_t \approx 0.04 - 0.51$ mN, a specific impulse in the range $I_{sp} \approx 150 - 270$ s, and a thrust efficiency in the range $\eta_t \approx 2 - 12\%$. The plasma density, temperature, and thrust performance was enhanced with increasing microwave input power, and the experimental results were consistent with those of numerical analysis. Similar plasma characteristics and thrust performance were obtained with H_2 propellant, where the specific impulse I_{sp} (≤ 450 s) was more than 1.5 times higher than that with He, owing to a difference in mass between He and H_2.

A comparison with previous numerical and experimental studies with Ar propellant [70] indicated that the plasma electron density n_e was about three times lower in He and H_2 than in Ar; however, the gas temperature $T_g \approx T_{rot}$ was remained a little lower in He and H_2, and the specific impulse I_{sp} was found to be enhanced by about 3 – 5 times with light-mass He and H_2, as has been known for

large-scale propulsion systems [69]. Moreover, the axial flow velocity u calculated was more than two times larger in He than that in Ar in the microplasma source as well as micronozzle regions owing to the higher sonic speed a of He, because u is governed primarily by the choking ($Ma = u/a = 1$) at the nozzle throat. Thus, in contrast to general assumptions, it follows that in the microplasma thruster of electrothermal type, the high surface-to-volume ratio of microplasma sources and the high diffusivity and thermal conductivity of light-mass propellants do not lead to a deterioration of the thrust performance. This is attributed primarily to a more significant thermal energy gain due to elastic collisions between electrons and heavy particles in He and H_2 as compared to that in Ar, which tends to offset a more significant thermal energy loss due to the high diffusivity and thermal conductivity of He and H_2 in the microplasma source of high surface-to-volume ratios.

Chapter 4

X-band microwave excitation

4.1 Introductory remarks

Microplasmas are attracting attention for research field, from both viewpoint of fundamentals and applications [85]. Recently, experimental and numerical investigations of microplasma sources are carried out actively [86–91], and expand application to various fields, such as material deposition [92–94] and space propulsion [95]. In this work, we used X-band (11-GHz) microwave source instead of S-band (4-GHz) in previous works, and investigated the plasma characteristics and the thrust performance experimentally and numerically, for the potentialities of more compact design and higher performance. For larger scale plasma, X-band microwaves are used for electron cyclotron resonance (ECR) sources to obtain higher plasma electron density and more intense ion beam including multiply ionized ions [96, 97].

4.2 Experimental setup

Figure 4.1 shows a cross-sectional view of the microplasma thruster presently developed, which consists of an azimuthally symmetric surface wave-excited plasma source and a conical micronozzle for exhausting the plasma. The microplasma source consists of a dielectric chamber, 1.5 – 2.0 mm in inner diameter and 4.0 – 10 mm long, and a metal around the chamber. Microwaves are gen-

erated by a signal generator, and amplified through a semiconductor amplifier. Then they propagate through a three-stub tuner and coaxial cable which is connected to the left end of the plasma chamber, and penetrate into the chamber, where the propellant is ionized and heated up by surface waves. The high thermal energy is converted into directional kinetic energy through the nozzle which has a converging and diverging section, to obtain the thrust. The diameter of the nozzle inlet, throat, exit is 0.6 mm, 0.2 mm, 0.8 mm, respectively. To characterize the microplasma concerned, the optical emission from the plasma was observed in the side-view direction around the end of the antenna or dielectric envelope (just upstream of the micronozzle inlet). A 50-cm focal length spectrograph/monochromator was employed in these experiments, having a grating of 2400 lines/mm and charge-coupled device (CCD) detector. The spectral resolution, determined using a low-pressure Ar discharge lamp, was 0.025 nm with an entrance slit width of 5 μm. The experimental setup for thrust measurement has been detailed elsewhere [45]. We used a target-type thrust stand; a small concave cylindrical target block was hung downstream of the nozzle exit with the thruster fixed tightly, and the gas/plasma plume ejected from the thruster struck the target mounted at one end of the pendulum with some weights being at the other end for balance. Here, the target employed was a small Faraday cup-like one made of poly-tetrafluoroethylene (PTFE), to suppress the effects of reflected particles of the jet plume striking the target [98]. A displacement was measured by using a laser displacement gauge having a resolution of $\Delta x < 0.1\,\mu$m. The experimental model used in this work is shown in Fig. 4.1 (c), optimizing the dimensions for 11-GHz microwaves, and resolving the problems about heat and mechanical strength of our previous model (Fig. 4.1 (b)). Also, similar design improved model for 4.0-GHz microwaves was prepared for control experiment, to investigate pure effects of higher frequency microwaves. The design improvement is described in Sec. 4.3. We use argon for the propellant.

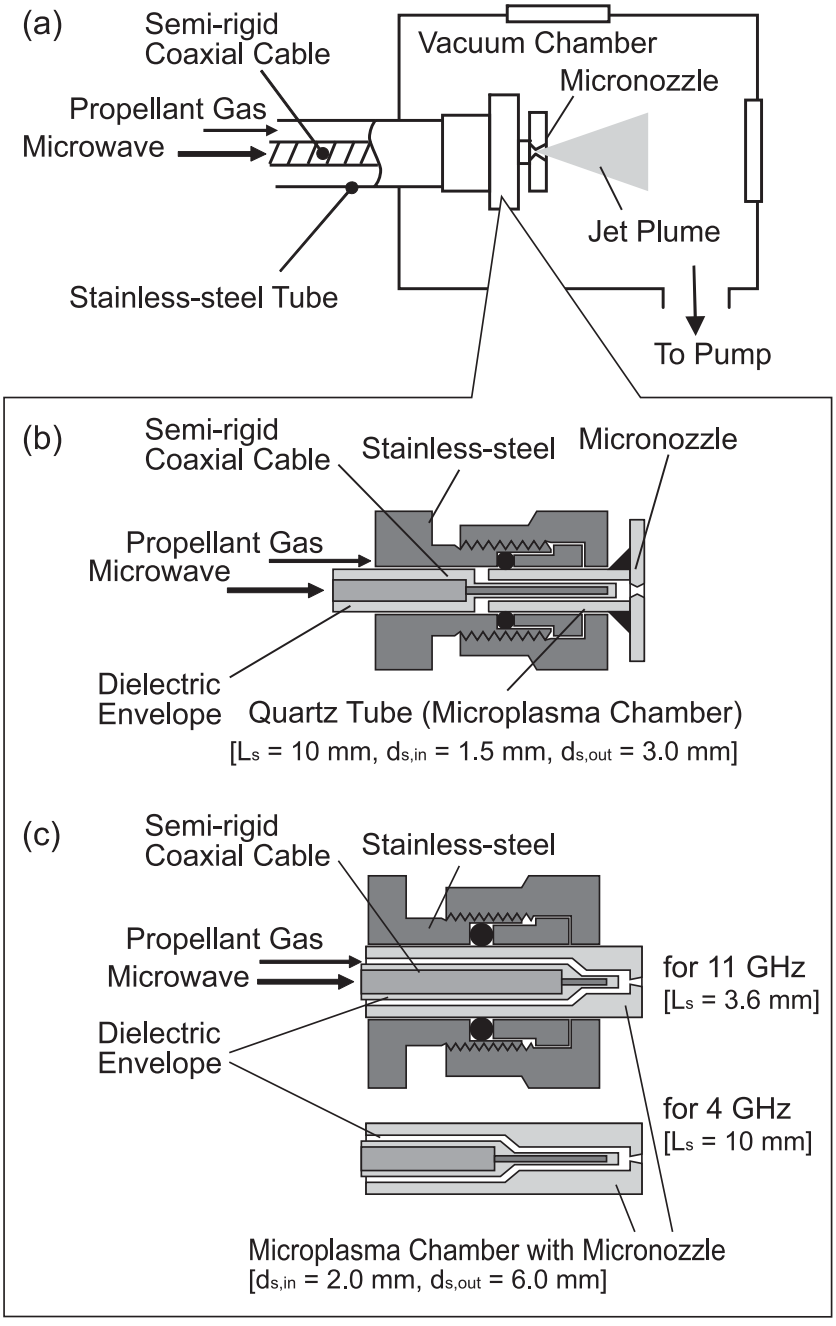

Figure 4.1: (a) Cross-sectional view of a microplasma thruster, and (b)(c) its radially enlarged view (b) shows the previous model, and (c) shows the improved model in this work for 11-GHz and 4-GHz microwaves.

4.3 Design improvement

The previous model succeeded to generate plasma and obtain sufficient thrust performance for nanosatellites. Stable plasma generation at the microwave power range of 2.0 – 8.0 W with argon propellant was achieved. The thrust and the specific impulse were $\approx$ 1 mN and $\approx$ 80 s, respectively. However, it became clear that the previous model had some serious problems for continuous operation and installing to a satellite. First, the quartz cover for microwave antenna was too thin and could be often broken by shock and vibration, mainly at the joint section. It caused a difficulty to handle the thruster parts while assembling and adjusting the thruster module. The rubber O-rings were used for supporting the microplasma chamber and the antenna cover to the experimental apparatus without a leak of propellant gas. Especially, the former one was located only across the chamber wall from the plasma discharge area and damaged easily by heat. The vacuum-sealing adhesives joining the microplasma chamber and the micronozzle had also insufficient heat resistance. Continuous operation time of the thruster is severely limited, less than 15 minutes at a microwave power of 6.0 W. Moreover, the previous model could not generate plasma discharge normally with 11-GHz higher-frequency microwaves. The discharge occurred at the root of the antenna, not at the top of the antenna (upstream of the nozzle inlet). Thus, we carried out a design of improved model optimized for 11-GHz, as well as resolving the structural and thermal problems.

From a numerical simulation, the plasma characteristics and thrust performance were significantly affected by the length of plasma chamber. As shown in Fig. 4.2, the average absorbed power density $\bar{Q}_{\mathrm{abs}}$ for 11-GHz microwave discharge were the highest with 4-mm-long plasma chamber, corresponding with the highest gas (heavy particle) temperature T_{h} and the specific impulse I_{sp}. As the length of plasma chamber is assumed to be equal to the length of antenna, this result can be explained by a basic quarter-wavelength antenna theory. The wavelength of 11-GHz microwaves in quartz ($\epsilon_{\mathrm{r}} = 3.8$) is 14.4 mm, thus the optimum

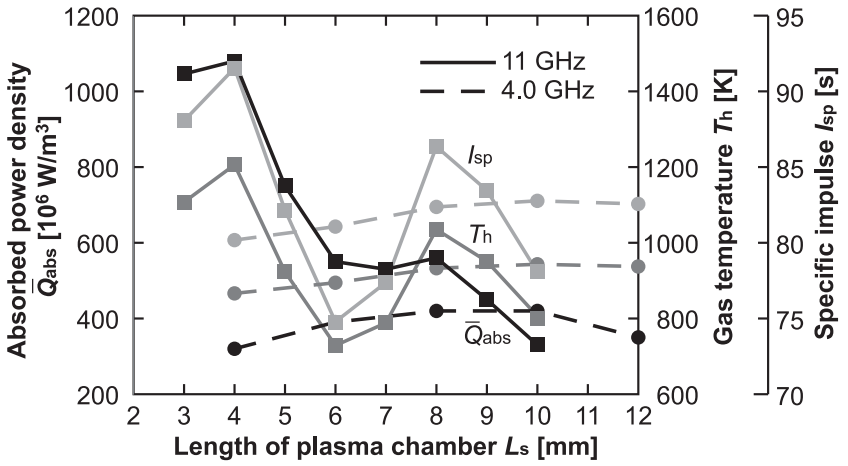

Figure 4.2: Average absorbed power density $\bar{Q}_{\mathrm{abs}}$, specific impulse I_{sp} and gas temperature T_{h} as a function of plasma chamber length L_{s}, calculated for the microwave frequency f = 11 GHz (solid line) and f = 4.0 GHz (dashed line), input power P_{in} = 6.0 W and Ar flow rate $\dot{m}$ = 0.9 mg/s.

antenna length (~ chamber length) is 3.6 mm. It is indicated that the higher-frequency microwaves and shorter plasma chamber can bring us more efficient gas heating and higher thrust performance, compared with our previous 4-GHz microwave-excited microplasma thruster. To improve mechanical strength, the thickness of antenna cover was increased from 0.2 mm to 0.3 mm and the joint section was modified from stepped shape to tapered shape. The microplasma chamber and the micronozzle are unified into a single component made from 6.0-mm-diameter quartz block, eliminating the adhesives connecting the chamber and nozzle. Swagelok Ultra-Torr®union is used for mounting the thruster, since it has sufficient vacuum sealing and ease of adjustment. The separation between the O-ring and the plasma chamber was increased from 0.8 mm to 8 mm, reducing the heat influx to the O-ring. It is expected that continuous operation time at higher power ($\geq$ 6 W) is significantly extended compared with our previous model.

4.4 Numerical model

The calculation area is 1.56 – 3.00 mm in radius and 6.54 – 12.54 mm long, containing the plasma chamber and coaxial cable. The calculation cell is 10×10 μm, and thus the area consists of 156 – 300 cells in the radial direction and 654 – 1254 cells in the axial direction. In addition, the chamber is made of quartz (relative permittivity $\epsilon_r = 3.8$), the envelope of the coaxial cable is made of polytetrafluoroethylene ($\epsilon_r = 2.1$), and all metallic parts are treated as perfect conductor.

The numerical model consisted of an electromagnetic module for microwave propagation interacting with plasmas and a fluid module for plasma flows with two (electron and heavy particle) temperatures. The former employed the finite difference time-domain (FDTD) approximation, being applied to the plasma source region, to analyze the microwave power absorbed in the plasma. The latter employed two-temperature fluid equations, being applied to both the source and the nozzle regions, to analyze the plasma and nozzle flow characteristics. Gas-phase reactions were taken into account in the fluid module, along with plasma-wall interactions in a limited space, and the analysis of the nozzle flow finally gave the thrust performance achieved. The working gas of interest in this simulation was Ar, and the other assumptions in calculation were detailed in Ref. [70].

4.5 Results and discussions

4.5.1 Numerical results

Figures 4.3(a) – 4.3(h) show the spatial distribution of the electron density n_e, electron temperature T_e, gas (heavy particle) temperature T_h, absorbed power density Q_{abs}, pressure p, axial flow velocity u, Ar ground-state density n_g, and Ar metastable state density n_* in the microplasma source, respectively. Here, the diameter and length of the antenna are $d_{an} = 0.48$ mm and $L_{an} = 3.6$ mm (2.5 mm in the plot area and 1.1 mm out of the plot area), respectively; the inner diame-

ter, outer diameter, and length of the dielectric envelope covering the antenna are $d_{\mathrm{d,in}} = d_{\mathrm{an}} = 0.48$ mm, $d_{\mathrm{d,out}} = 1.2$ mm, and $L_d = 3.5$ mm, respectively; the inner diameter, outer diameter, and length of the dielectric chamber of the microplasma source are $d_{\mathrm{s,in}} = 2.04$ mm, $d_{\mathrm{s,out}} = 6.0$ mm, and $L_{\mathrm{s}} = 4.5$ mm, respectively. The calculation conditions are an input power $P_{\mathrm{in}} = 6.0$ W of $f = 11$ GHz microwaves, Ar mass flow rate $\dot{m} = 1.5$ mg/s (flow rate of 50 sccm), and quartz chamber and envelope ($\epsilon_{\mathrm{r}} = 3.8$). The absorbed power calculated in the plasma is $P_{\mathrm{abs}} = 5.1$ W in total, corresponding to the average power density $\bar{Q}_{\mathrm{abs}} = 5.0 \times 10^8$ W/m^3. Note that the microwave power not absorbed in the plasma is reflected and/or passing through the source-nozzle boundaries, to leave the simulation area. The absorption efficiency was $P_{\mathrm{abs}}/P_{\mathrm{in}} \approx 85$ %. The electron density n_{e} exhibits its maximum near the end of the dielectric envelope of the antenna ($n_{\mathrm{e}} \approx 1.2 \times 10^{20}$ m^{-3}), being consistent with the distribution of the absorbed power density Q_{abs}. On the other hand, the gas temperature T_{h} exhibits its maximum in a space between the end of the dielectric envelope and the end wall of the dielectric plasma source chamber ($T_{\mathrm{h}} \approx 960$ K), where the micronozzle is located to achieve the aerodynamic acceleration of high temperature plasmas. In addition, the pressure calculated was almost uniform in the plasma source ($p \approx 35$ kPa), and the flow velocity was increased in the axial direction toward the end of the source region (up to $u \approx 35$ m/s). Also shown in Figs. 4.3(i) and 4.3(j) are snapshots of the distribution of the radial E_r and axial E_z electric fields of microwaves. Moreover, the peak position of the absorbed power density Q_{abs} corresponds to that of E_z (not E_r), implying that the axial E_z is the major component of microwave electric fields that contributes to Q_{abs} and thus to P_{abs}.

Figure 4.4 shows the distribution of plasma characteristics for 4.0-GHz microwaves. The dimensions are the same as Figs. 4.3 and 4.7, except for the axial length of plasma source region. The length of the antenna is $L_{\mathrm{an}} = 9.6$ mm (8.5 mm in the plot area and 1.1 mm out of the plot area), the dielectric envelope covering the antenna $L_{\mathrm{d}} = 9.5$ mm, and the dielectric chamber of the microplasma source $L_{\mathrm{s}} = 10.5$ mm, respectively. The calculation conditions are an input power

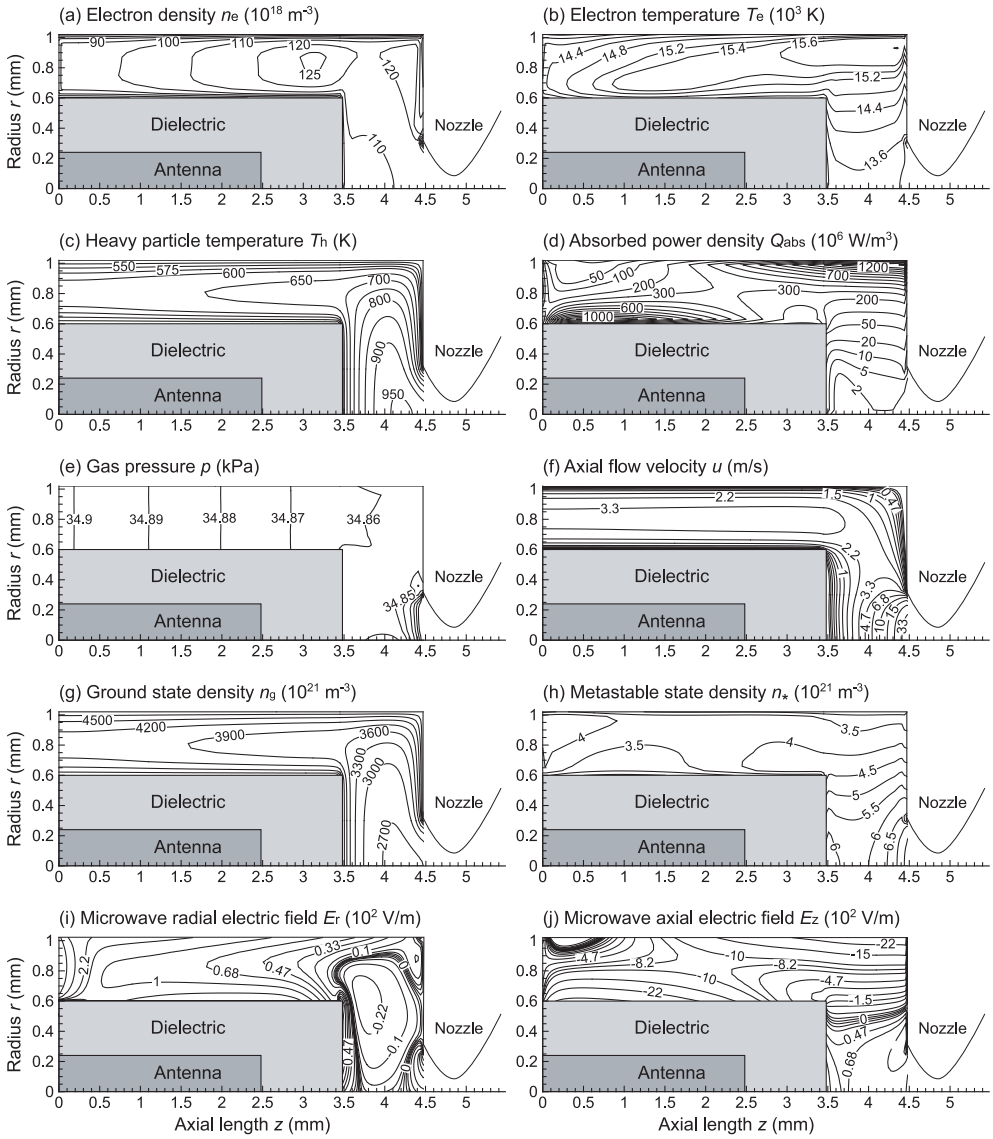

Figure 4.3: Distribution of the (a) electron density n_e, (b) electron temperature T_e, (c) heavy particle temperature T_h, (d) absorbed power density Q_{abs}, (e) gas pressure p, (f) axial flow velocity u, (g) Ar ground-state density n_g, and (h) Ar metastable-state density n_* in the microplasma source, calculated for an input power P_{in} = 6.0 W of f = 11 GHz microwaves, Ar mass flow rate $\dot{m}$ = 1.5 mg/s (flow rate of 50 sccm). Also shown is a snapshot of the distribution of the (i) radial E_r and (j) axial E_z electric fields of the microwaves in the microplasma region.

P_{in} = 6.0 W of f = 4.0 GHz microwaves, Ar mass flow rate $\dot{m}$ = 1.5 mg/s (flow rate of 50 sccm). The absorbed power calculated in the plasma is P_{abs} = 4.5 W in total.

Comparing the results shown in Figs. 4.3 and 4.4, the electron density n_{e} and heavy particle temperature T_{h} are significantly increased. n_{e} for 11-GHz is 1.4 times larger than that of 4-GHz, corresponding to higher absorbed power density Q_{abs}. The reasons for high Q_{abs} are presumed to be following two. First, the volume of plasma source is smaller and the total absorbed power is almost equal, simply thus the Q_{abs} is larger. Second, the higher-frequency microwaves are well absorbed even under dense plasma condition, as well as large-scale microwave plasma source [96, 97]. Also, the gas temperature T_{h} for 11-GHz is $\approx$ 200 K higher than that of 4-GHz, From a viewpoint of electrothermal thruster, higher gas temperature directly leads to better thrust performance, especially specific impulse. The electron temperature T_{e} around the nozzle inlet for 11-GHz is 1000 – 2000 K higher than that of 4-GHz, while the maximum temperature remained almost the same. On the other hand, the flow velocity u make little difference between 11-GHz and 4-GHz.

Figures 4.5 and 4.6 show the distribution of plasma characteristics in non-optimum configurations. The former is with 11-GHz microwaves and long plasma chamber. Since the length of the chamber and the antenna is larger than quarter-wavelength, the injected microwaves are absorbed at two sections. The averaged power density $\bar{Q}_{\mathrm{abs}}$ was lower than that with short chamber (see Fig. 4.3), leading to lower electron density n_{e} and gas temperature T_{h}. The latter is with 4.0-GHz microwaves and short plasma chamber. Since the length of the chamber and the antenna is shorter than quarter-wavelength, the injected microwaves cannot form resonance at the antenna. The total absorbed power P_{abs} was significantly lower than that with long chamber (see Fig. 4.4).

Figures 4.7(a) – 4.7(h) show the distribution of the electron density n_{e}, electron temperature T_{e}, gas (heavy particle) temperature T_{h}, Mach number Ma, pressure p, axial flow velocity u, Ar ground-state density n_{g}, and Ar metastable-state den-

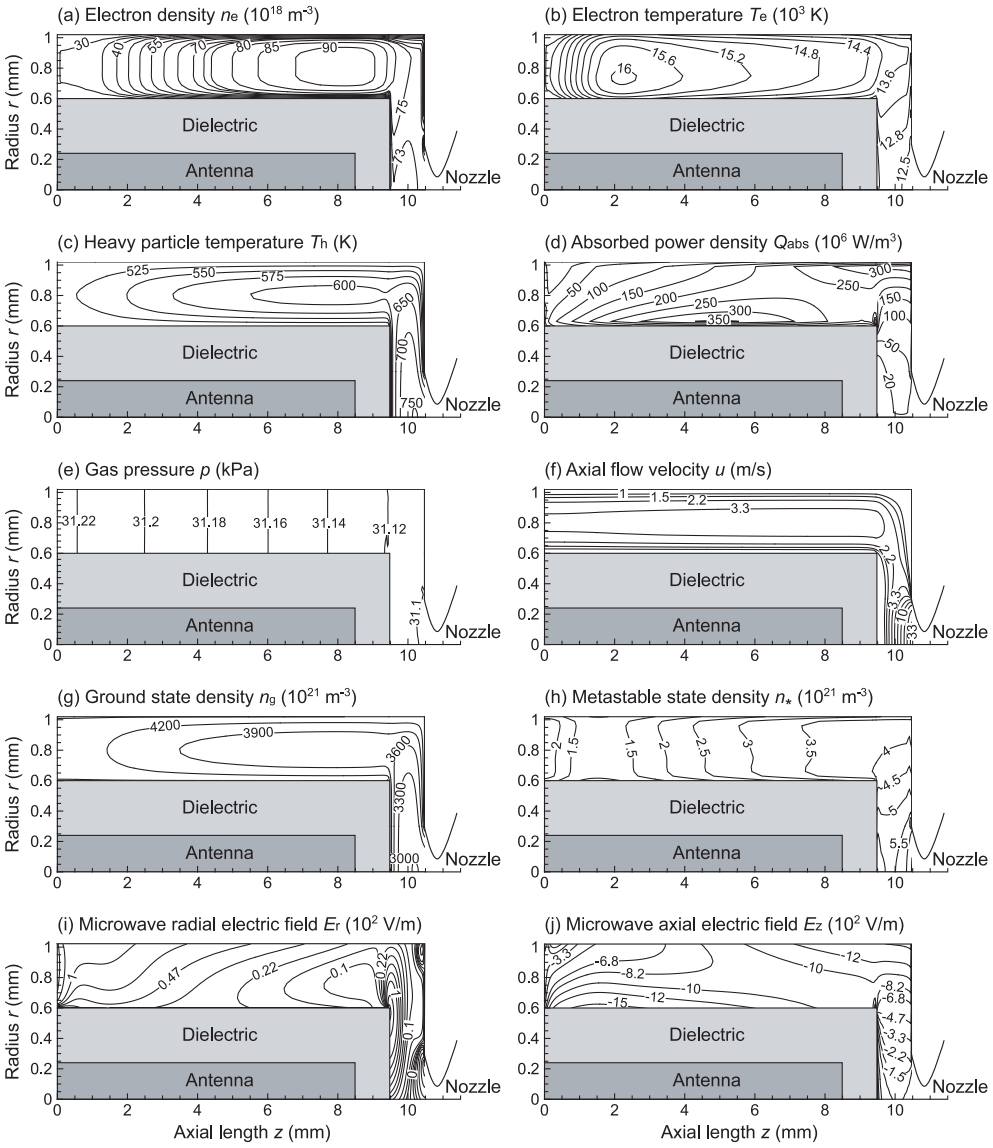

Figure 4.4: Distribution of the (a) electron density n_e, (b) electron temperature T_e, (c) heavy particle temperature T_h, (d) absorbed power density Q_{abs}, (e) gas pressure p, (f) axial flow velocity u, (g) Ar ground-state density n_g, and (h) Ar metastable-state density n_* in the microplasma source, calculated for an input power $P_{in} = 6.0$ W of $f = 4.0$ GHz microwaves, Ar mass flow rate $\dot{m} = 1.5$ mg/s (flow rate of 50 sccm). Also shown is a snapshot of the distribution of the (i) radial E_r and (j) axial E_z electric fields of the microwaves in the microplasma region.

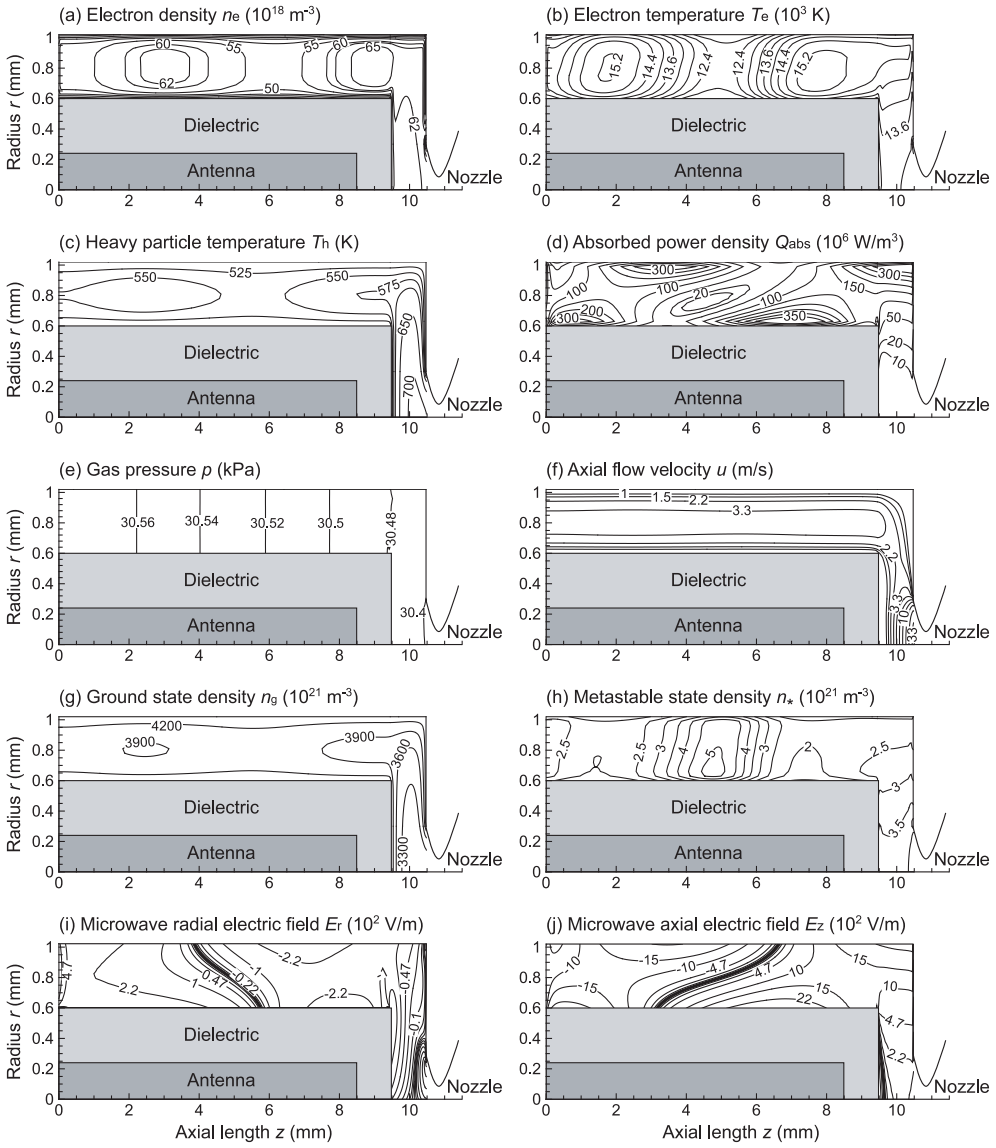

Figure 4.5: Distribution of the (a) electron density n_e, (b) electron temperature T_e, (c) heavy particle temperature T_h, (d) absorbed power density Q_{abs}, (e) gas pressure p, (f) axial flow velocity u, (g) Ar ground-state density n_g, and (h) Ar metastable-state density n_* in the microplasma source, calculated for an input power P_{in} = 6.0 W of f = 11 GHz microwaves, Ar mass flow rate $\dot{m}$ = 1.5 mg/s (flow rate of 50 sccm), using the long plasma chamber for 4.0 GHz. Also shown is a snapshot of the distribution of the (i) radial E_r and (j) axial E_z electric fields of the microwaves in the microplasma region.

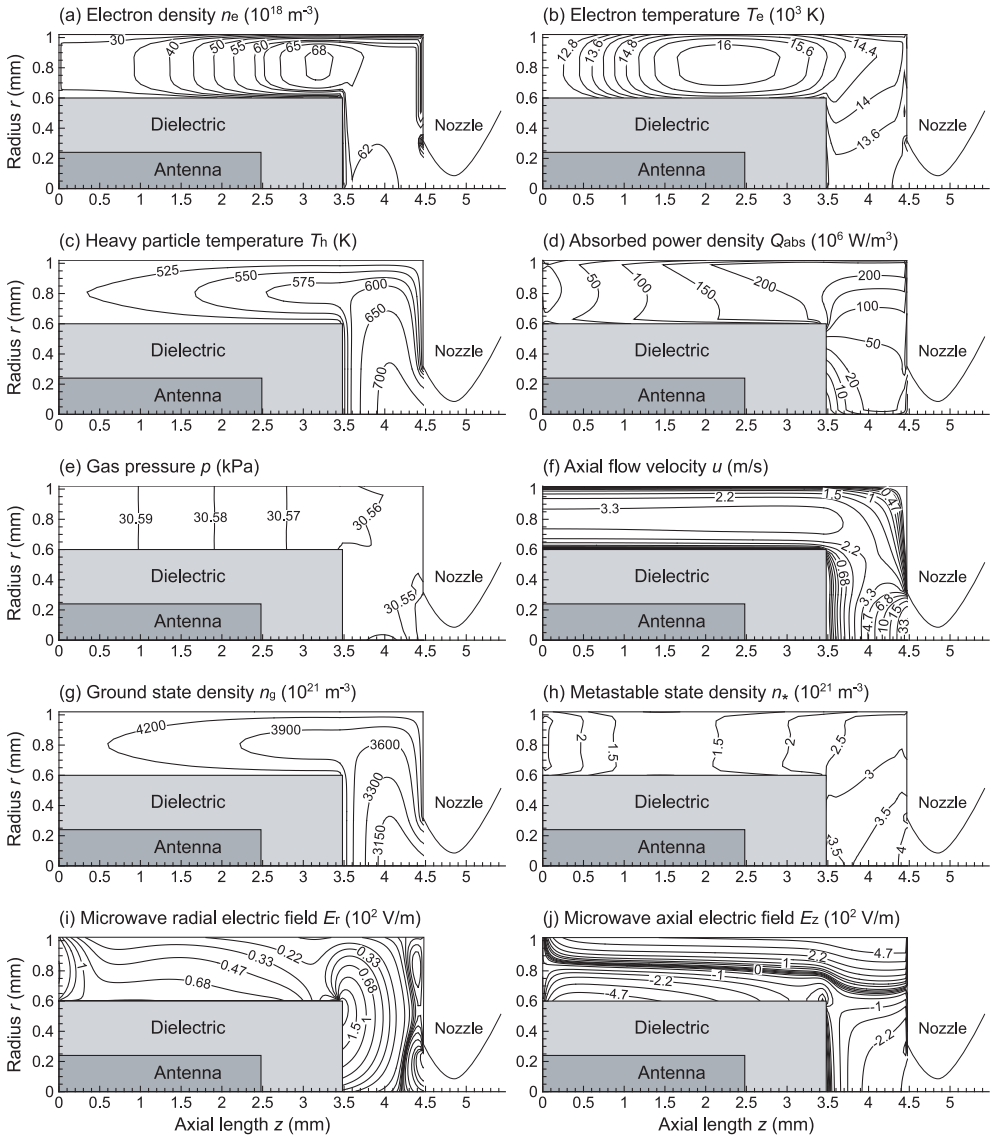

Figure 4.6: Distribution of the (a) electron density n_e, (b) electron temperature T_e, (c) heavy particle temperature T_h, (d) absorbed power density Q_{abs}, (e) gas pressure p, (f) axial flow velocity u, (g) Ar ground-state density n_g, and (h) Ar metastable-state density n_* in the microplasma source, calculated for an input power $P_{in} = 6.0$ W of $f = 4.0$ GHz microwaves, Ar mass flow rate $\dot{m} = 1.5$ mg/s (flow rate of 50 sccm), using the short plasma chamber for 11 GHz. Also shown is a snapshot of the distribution of the (i) radial E_r and (j) axial E_z electric fields of the microwaves in the microplasma region.

sity n_* in the micronozzle, respectively, obtained in the same numerical simulation as Fig. 4.3. Here, the Mach number is given by $Ma = |\mathbf{v}|(\gamma k_B T_h/m_h)^{-1/2}$, where $\gamma = 5/3$ is the specific heat ratio for monoatomic gases. The temperature T_h, Mach number Ma, pressure p, and axial velocity u exhibit a characteristic of the subsonic-supersonic flow in the converging-diverging nozzle: Ma and u increase with increasing axial distance, with $Ma = 1$ being at around the throat, while T_h and p decrease downstream along the nozzle axis.

From the results shown in Figs. 4.7 (for 11-GHz) and 4.8 (for 4.0-GHz), the nozzle flow characteristics are similar between the two. The higher gas temperature T_h at the nozzle inlet for 11-GHz made the axial flow velocity u and pressure p at the nozzle exit 10 – 15 % higher, producing more thrust. More significant boundary layer effects are also observed, where the micronozzle flow is heavily affected by viscous dissipation in boundary layers owing to the high temperature T_h of heavy particles.

The thrust performance is calculated as [61, 69]

$$F_t = 2\pi \int_0^{r_{ex}} (\rho u^2 + p) r dr, \tag{4.1}$$

$$I_{sp} = \frac{F_t}{\dot{m} g}, \tag{4.2}$$

where F_t is the thrust and I_{sp} is the specific impulse. In these equations, r_{ex} denotes the exit radius of the nozzle, ρ the mass density, u the exhaust flow velocity in the axial direction, p the pressure, $\dot{m}$ the mass flow rate, and g the gravitational constant. Note that F_t consists of the momentum and pressure thrust. The pressure thrust is usually neglected owing to its less contribution to the total thrust; however, reducing the size of the nozzle results in under-expanded gas/plasma flows inside the nozzle owing to highly viscous flows therein, so that the pressure thrust should be taken into account in the present micro plasma thruster [42, 45, 70]. The thrust and specific impulse under the conditions of Figs. 4.3 and 4.7 are calculated to be $F_t = 1.21$ mN and $I_{sp} = 83.7$ s, respectively. The thrust performance with 11-GHz microwaves is improved by 10 % compared with that with 4-GHz microwaves ($F_t = 1.10$ mN and $I_{sp} = 76.1$ s).

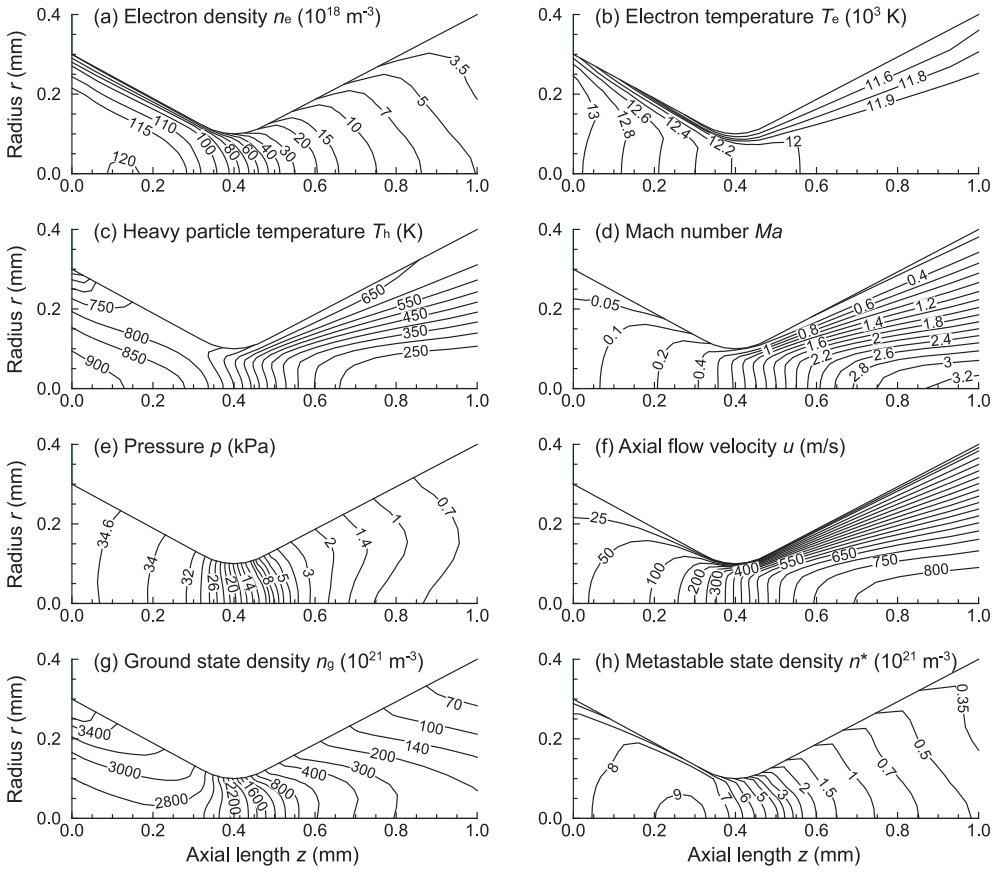

Figure 4.7: Distribution of the (a) electron density n_e, (b) electron temperature T_e, (c) heavy particle temperature T_h, (d) Mach number Ma, (e) pressure p, (f) axial flow velocity u, (g) Ar ground-state density n_g, and (h) Ar metastable-state density n_* in the micronozzle, obtained in the same numerical simulation as Fig. 4.3.

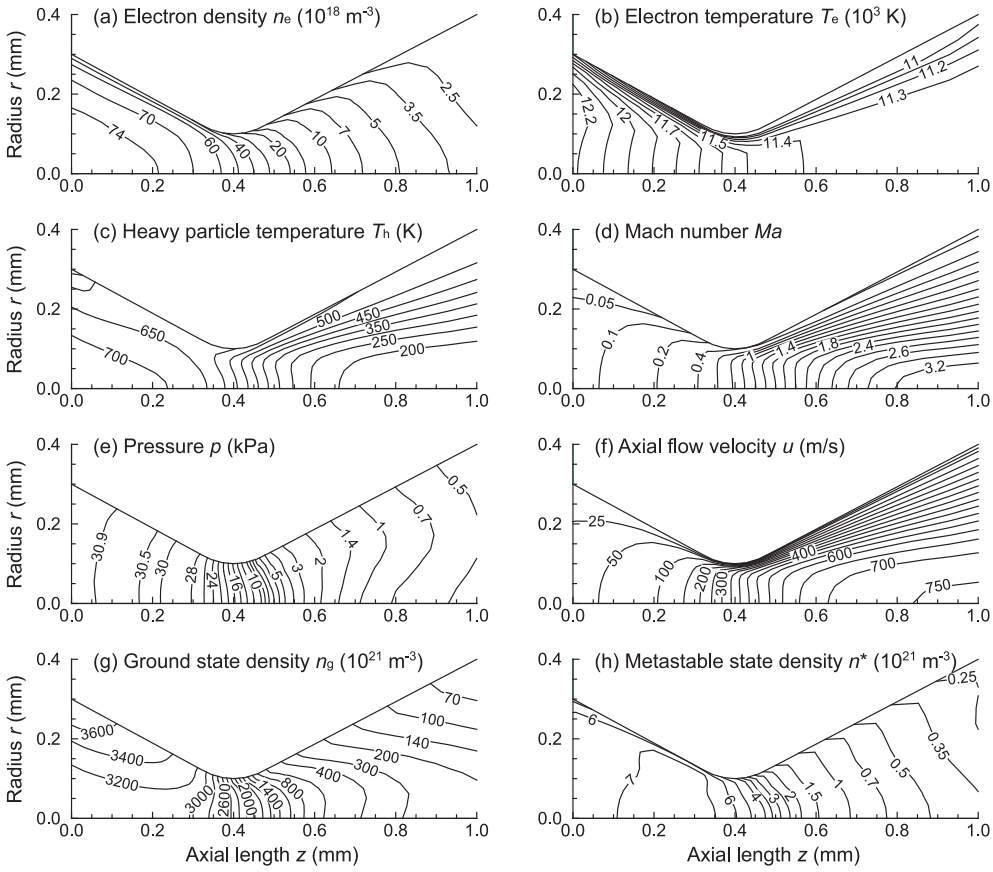

Figure 4.8: Distribution of the (a) electron density n_e, (b) electron temperature T_e, (c) heavy particle temperature T_h, (d) Mach number Ma, (e) pressure p, (f) axial flow velocity u, (g) Ar ground-state density n_g, and (h) Ar metastable-state density n_* in the micronozzle, obtained in the same numerical simulation as Fig. 4.4.

4.5.2 Experiments

The gas flow rate (or mass flow rate $\dot{m}$) and the source pressure p_0 measured with and without plasma discharge were approximately related by the quasi-one dimensional nozzle flow equation for an isentropic flow of perfect gases in a converging-diverging nozzle [60, 61],

$$\dot{m} = \rho u A = p_0 A^* \left[\frac{\gamma}{RT_0} \left(\frac{2}{\gamma + 1} \right)^{(\gamma+1)/(\gamma-1)} \right]^{1/2}, \tag{4.3}$$

as shown in Fig. 4.9. The equation assumes the so-called choked flow, or the sonic velocity at the throat followed by further increase in velocity under supersonic flow conditions in the divergent portion of the nozzle. Here, ρ is the mass density, u the flow velocity, A the cross section of the nozzle, A^* that of the throat, γ the specific heat ratio ($\gamma = 5/3$ for Ar), R the universal gas constant ($R = k_B/m_h$), and T_0 the gas/plasma temperature in the microplasma source. The temperature T_0 was taken to be the room temperature in cold gas operation, and the gas/rotational temperature spectroscopically measured in plasma discharge.

Figures 4.10 and 4.11 show the typical optical emission spectra with 11-GHz and 4-GHz microwaves, respectively. The spectra were obtained with input microwave power of 6.0 W and gas flow rate of 0.30 mg/s (10 sccm), being the intensity maximum. As shown in Fig. 4.10, far more intense emission in the wavelength region of 300 – 600 nm (near-ultraviolet to yellow) was observed for 11-GHz plasma, compared with 4-GHz plasma. These emission lines are owing to excited Ar^+ ions, typically observed in high electron temperature T_e plasmas. Figures 4.12 and 4.13 show the intensity of four spectral lines measured as a function of Ar gas flow rate. The measured spectral lines are shown in Table 4.1 [99]. The intensities of Ar II (Ar^+) lines decrease rapidly with increasing flow rates, corresponding to decrease of high-energy electrons. On the other hand, the intensity of Ar I (Ar neutral) line exhibits a bottom at gas flow rate of 1.2 mg/s (40 sccm). In small flow rates, high energy electrons that have sufficient energy to excite ground state Ar atoms decrease with the flow rate. In large flow rates, the density of low-level excited Ar atom increases almost proportional to the density of ground-state

Table 4.1: Table of measured spectral lines.

Wavelength (nm)	Species	Transition	Lower level (eV)	Upper level (eV)
811.5	Ar I	$4s[1\ ^1/_2]^\circ - 4p[2\ ^1/_2]$	11.55	13.08
763.5	Ar I	$4s[1\ ^1/_2]^\circ - 4p[1\ ^1/_2]$	11.55	13.17
514.5	Ar II	$4s\ ^2P - 4p\ ^4D^\circ$	17.14	19.55
385.1	Ar II	$4s\ ^4P - 4p\ ^4S^\circ$	16.75	19.97
358.8	Ar II	$4p\ ^4D^\circ - 4d\ ^4F$	19.49	22.95

($\approx$ pressure and flow rate). These results indicate that more high-energy electrons exist in 11-GHz plasma compared with 4-GHz plasma, especially in small flow rates.

The microwave spectrum was measured by a magnetic loop probe and a spectrum analyzer (Agilent E4408B). The measurement condition was input microwave power of 6.0 W and gas flow rate 0.30 mg/s (10 sccm). The loop probe was placed at 3 mm from the end of microplasma chamber. There was a sharp peak at 11 GHz, indicating that some microwaves are spilled-off from the microplasma source, while no harmonics frequency was observed.

Since present experimental setup employs a 500-mm flexible coaxial cable for feeding microwaves to the thruster module, the power attenuation is a significant issue. The microwave power was measured by a power meter (HP 437B/8481A) with 30-dB attenuator. When nominal power 6.0W of 11-GHz microwaves was injected into the thruster module, the output power of the amplifier was 8.9 W and thus the transmission loss of coaxial cable reached more than 30%. On the other hand, the transmission loss was only 15% for 4.0-GHz microwaves. Thus, a countermeasure for transmission loss of microwaves, such as shortening the transmission path to the minimum and using waveguides instead of coaxial cables, is required for 11-GHz system.

Figure 4.14 shows the plasma electron density n_e and gas/rotational temperature $T_g \approx T_{rot}$ measured as a function of Ar gas flow rate and microwave power P_{in}. Here, the electron density was measured by adding a small amount (< 1 %) of H_2 and analyzing the Stark broadening of the H Balmer-β spectral line at 486.1

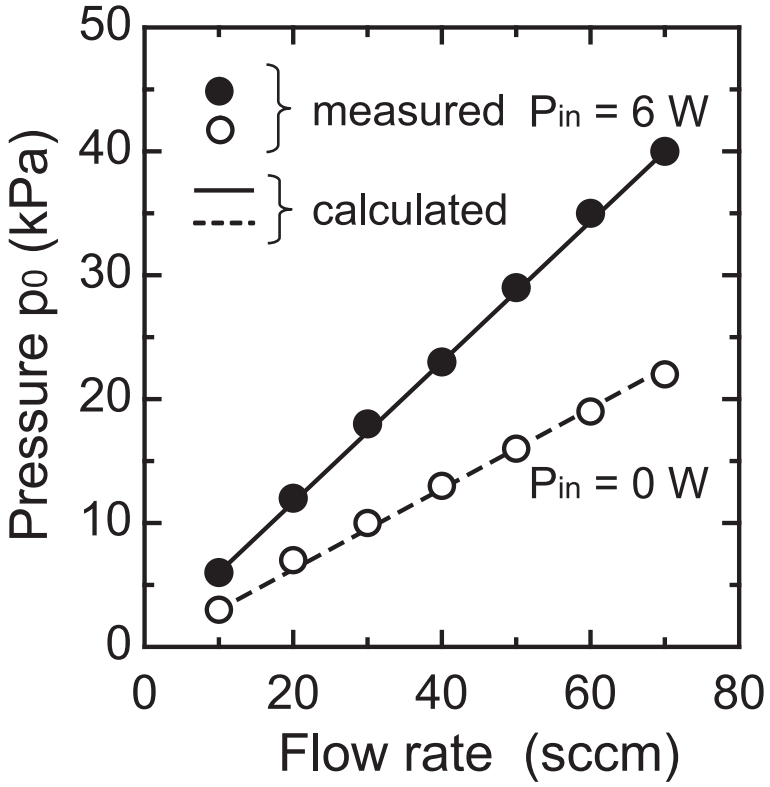

Figure 4.9: Source pressure p_0 measured as a function of gas flow rate (or mass flow rate $\dot{m}$) with and without plasma discharge (f = 11 GHz, P_{in} = 6 W, $\epsilon_{\text{d}} \approx 3.8$). Also shown are the curves calculated based on the quasi-one dimensional nozzle flow equation for an isentropic flow of perfect gases in a converging-diverging nozzle, assuming the so-called choked flow condition at the throat. Here, the gas/plasma temperature T_0 in the microplasma source was taken to be the room temperature in cold gas operation, and the gas/rotational temperature spectroscopically measured in plasma discharge (as will be shown in Fig. 4.14).

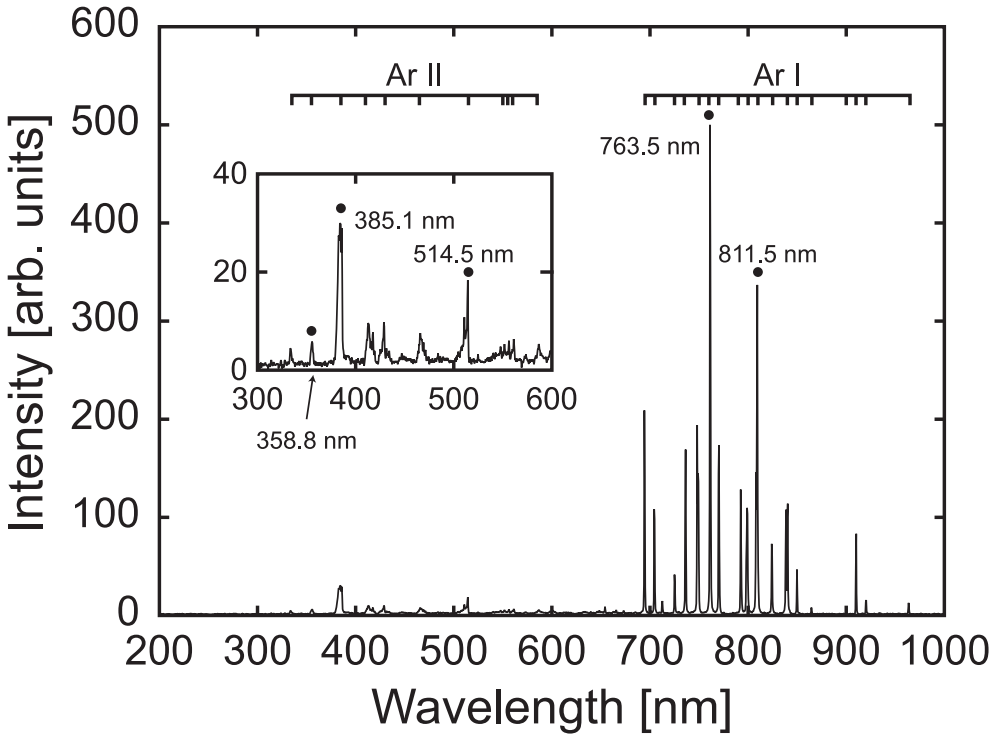

Figure 4.10: Typical optical emission spectrum with 11-GHz microwaves. The input microwave power and gas flow rate were 6.0 W and 0.30 mg/s (10 sccm), respectively.

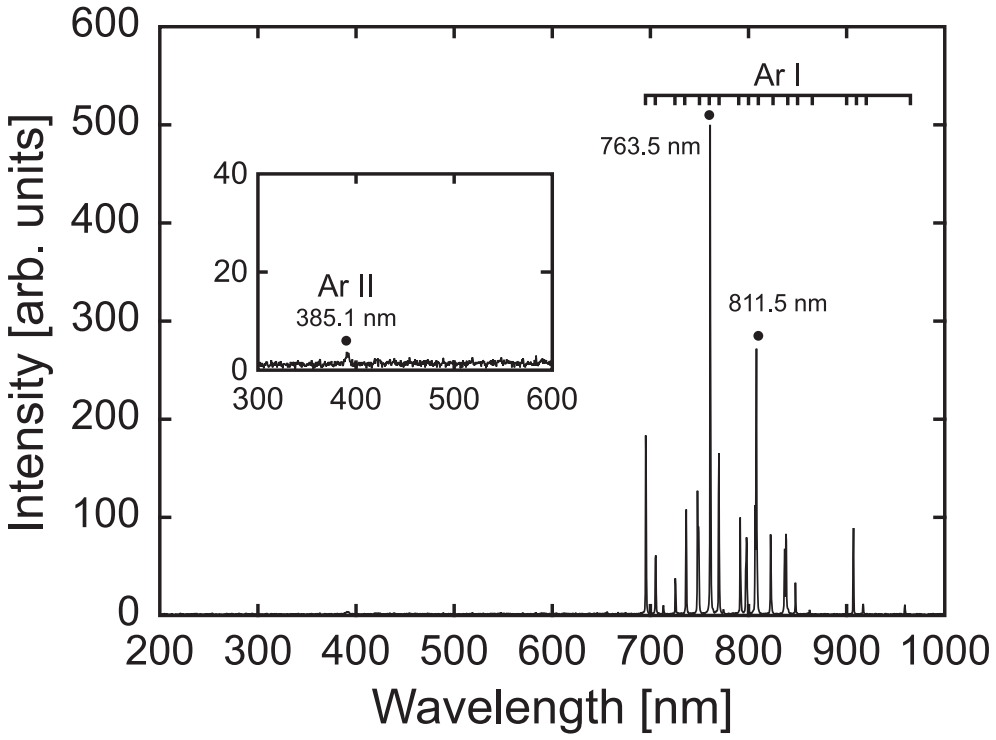

Figure 4.11: Typical optical emission spectrum with 4.0-GHz microwaves. The input microwave power and gas flow rate were 6.0 W and 0.30 mg/s (10 sccm), respectively.

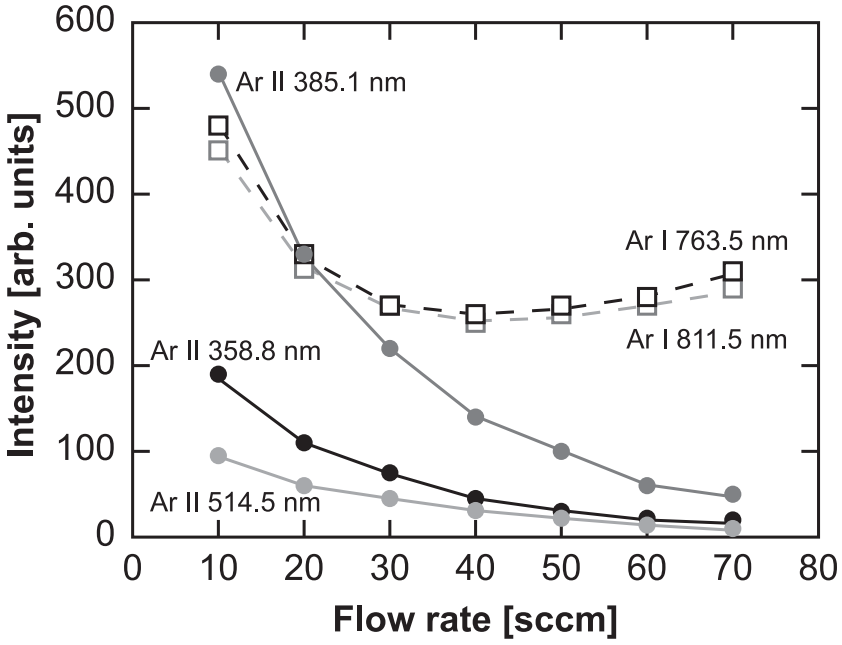

Figure 4.12: Optical emission intensity measured as a function of Ar gas flow rate. These data were taken under conditions of $f = 11$ GHz and microwave power of $P_{\text{in}} = 6.0$ W.

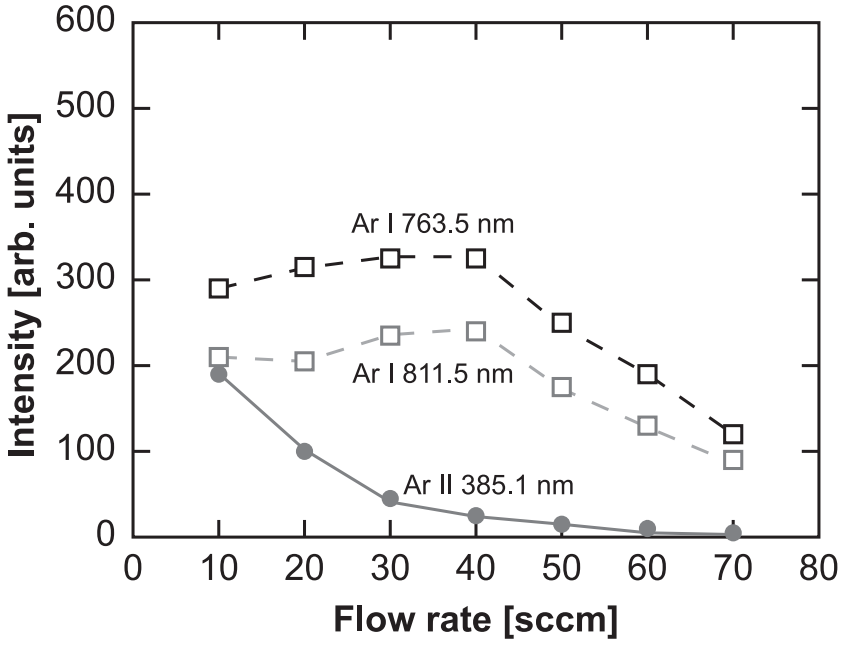

Figure 4.13: Optical emission intensity measured as a function of Ar gas flow rate. These data were taken under conditions of $f = 4.0$ GHz and microwave power of $P_{\text{in}} = 6.0$ W.

nm. The H_β line broadening is generally appreciated to consist of the instrumentation $\Delta\lambda_{\rm instrum}$, Doppler $\Delta\lambda_{\rm Doppler}$ (depending on $T_{\rm g}$), pressure $\Delta\lambda_{\rm pressure}$ (depending on $T_{\rm g}$ and p_0) and Stark $\Delta\lambda_{\rm Stark}$ broadening (depending on $n_{\rm e}$ and $T_{\rm e}$) [63, 65, 70]; the former two are given by the Gaussian profile and the latter two by the Lorenzian profile, which are then approximated by the Voigt function in total with a full width at half maximum (FWHM) of $\Delta\lambda_{\rm V}$ (typically, $\Delta\lambda_{\rm V} \approx 0.04 - 0.07$ nm in the present experiments). It should be noted that the accuracy of the electron density determined from the Stark broadening relies on the spectral resolution of the measurement system and also on the assumption of analysis of the spectral line broadening; in practice, the present accuracy was estimated to be about ±20 %, primarily owing to the resolution $\Delta\lambda_{\rm instrum} \approx 0.025$ nm of the spectrometer system employed. Moreover, the gas/rotational temperature was measured by adding small amount (< 1 %) of N_2 and analyzing the vibronic spectrum of the N_2 2nd positive (0,2) band at 380.4 nm.

As shown in fig. 4.14, the electron density was in the range $n_{\rm e} \approx (4-14)\times10^{19}$ m^{-3}, and the gas temperature was in the range $T_{\rm g} \approx T_{\rm rot} \approx 700 - 1100$ K with Ar discharge using 11-GHz microwaves. Also shown in the figure are the curves of $n_{\rm e}$ and $T_{\rm g}$ (= $T_{\rm h}$) numerically simulated as in Sec. 4.5.1, where the data are those line-averaged in the radial direction between the end of the microwave antenna or dielectric envelope and the inlet of the nozzle. The gas temperature $T_{\rm g} \approx T_{\rm rot}$ and the electron density $n_{\rm e}$ was observed to increase with increasing $P_{\rm in}$. $T_{\rm g}$ decreased with increasing flow rate (or with increasing p_0 or $n_{\rm g}$ in the plasma source), being in good agreement between the numerical and experimental results. Compared with the results with 4-GHz microwaves shown in Fig. 4.15, $T_{\rm g}$ is significantly higher (≈ 200 K) than that with 4-GHz microwaves. $n_{\rm e}$ was also 20 – 50 % larger than that with 4-GHz microwaves.

Figures 4.16 shows the thrust performance (thrust $F_{\rm t}$, specific impulse $I_{\rm sp}$) measured and calculated as a function of Ar gas flow rate for different microwave input powers $P_{\rm in}$, where $P_{\rm in}$ = 0 W corresponds to the cold-gas operation without plasma discharge. The measurements with Ar propellant showed that the thrust

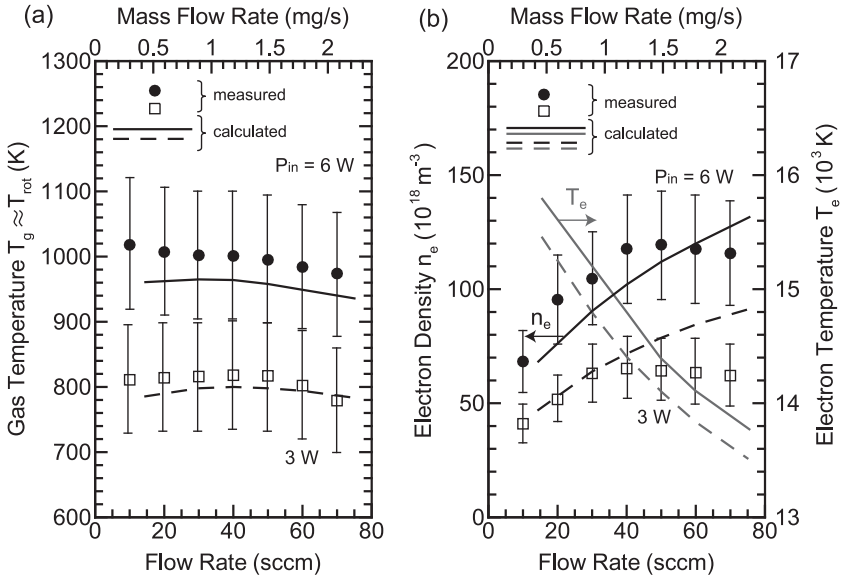

Figure 4.14: (a) Gas temperature $T_g \approx T_{rot}$ and (b) plasma electron density n_e measured as a function of Ar gas flow rate for different microwave powers P_{in}. These data were taken under conditions of f = 11 GHz and $\epsilon_d \approx 3.8$, with a small amount (0.05 sccm) of additive gases of H_2 and N_2. Also shown in the figure are the curves of $T_g (= T_h)$, n_e and electron temperature T_e numerically simulated.

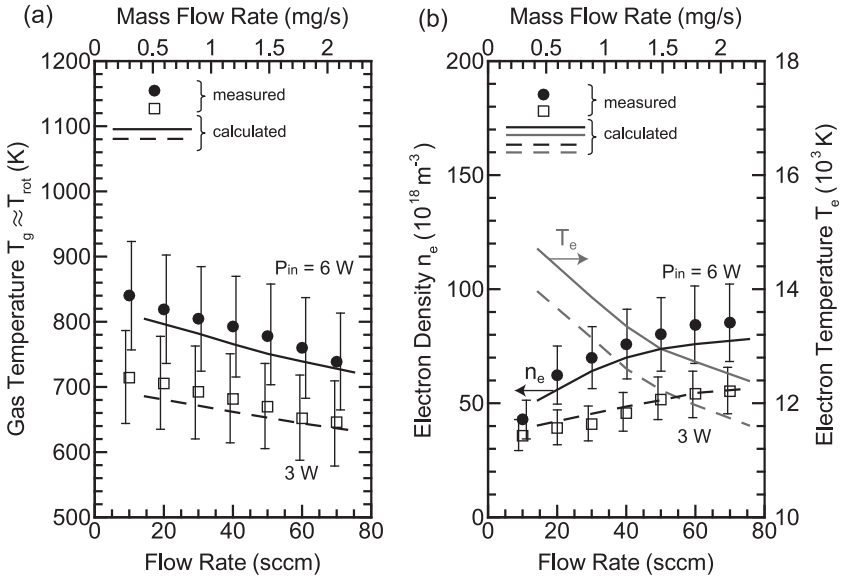

Figure 4.15: (a) Gas temperature $T_g \approx T_{rot}$ and (b) plasma electron density n_e measured as a function of Ar gas flow rate for different microwave powers P_{in}. These data were taken under conditions of $f = 4.0$ GHz and $\epsilon_d \approx 3.8$, with a small amount (0.05 sccm) of additive gases of H_2 and N_2. Also shown in the figure are the curves of $T_g (= T_h)$, n_e and electron temperature T_e numerically simulated.

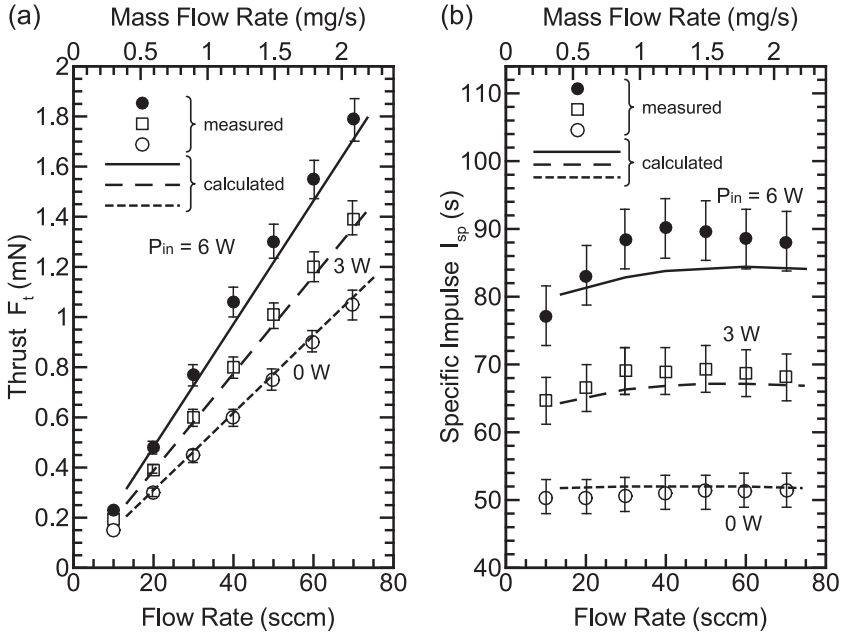

Figure 4.16: Thrust performance [(a) thrust F_t and (b) specific impulse I_{sp}] measured as a function of Ar gas flow rate for different microwave powers P_{in} under the same conditions as in Fig. 4.14 (11-GHz). Also shown in the figure are the curves of F_t and I_{sp} calculated from the numerical analysis.

performance was enhanced with the discharge on and with increasing P_{in}, and that the thrust and specific impulse were typically $F_t \approx 1.8$ mN and $I_{sp} \approx 90$ s, respectively, at $P_{in} = 6$ W and a Ar flow rate of 70 sccm (2.1 mg/s). A good agreement was obtained between the experiments and numerical analysis, giving $F_t \approx 0.2 - 1.8$ mN and $I_{sp} \approx 60 - 90$ s at $P_{in} \leq 3 - 6$ W and Ar gas flow rates of 10 – 70 sccm. Compared with Fig. 4.17, the thrust F_t and specific impulse I_{sp} with 11-GHz microwaves were 10 – 15 % improved from the results with 4.0-GHz microwaves, corresponding to the higher gas temperature T_h.

4.6 Conclusions

In this work, we have investigated 11-GHz (X-band) microwave-excited micro plasma thruster, numerically and experimentally. The propellant gas employed

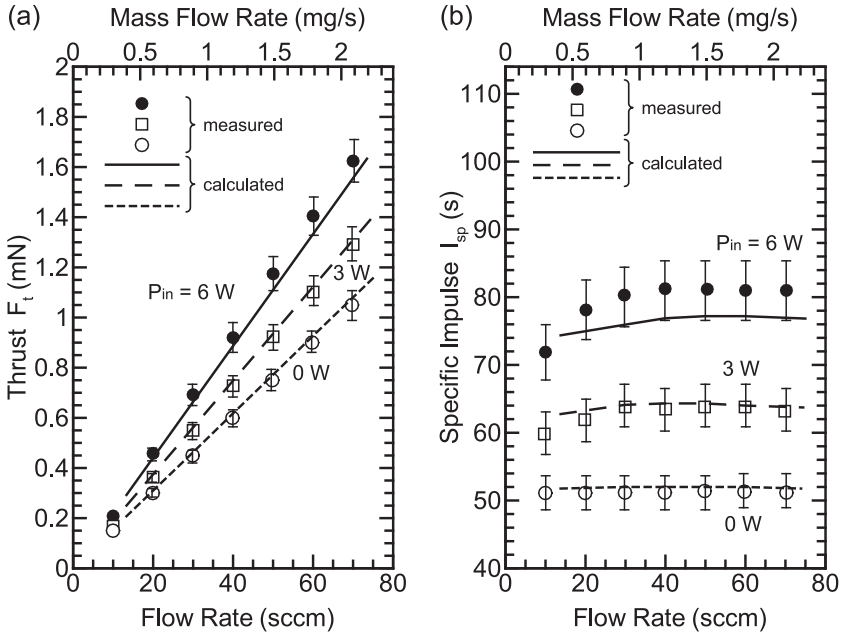

Figure 4.17: Thrust performance [(a) thrust F_t and (b) specific impulse I_{sp}] measured as a function of Ar gas flow rate for different microwave powers P_{in} under the same conditions as in Fig. 4.15 (4.0-GHz). Also shown in the figure are the curves of F_t and I_{sp} calculated from the numerical analysis.

was Ar at pressures of 10 – 50 kPa with flow rates of 10 – 70 sccm, and the surface wave-excited plasmas were established by 11 GHz microwaves at input powers of $P_{\mathrm{in}} \leq 6$ W. From the results of optical emission spectroscopy (OES), the Ar II (Ar^+) spectral lines were observed unlike the S-band microplasma, indicating the presence of electrons that have high enough energy to excite Ar^+ ions. The gas (heavy particle) temperature T_{g} and electron density n_{e} were measured by optical emission spectroscopy (OES), indicating that $n_{\mathrm{e}} \approx (4 - 14) \times 10^{19}$ m^{-3} and $T_{\mathrm{g}} \approx 700 - 1100$ K. The thrust F_{t} and specific impulse I_{sp} were measured by target-type thrust stand, indicating that $F_{\mathrm{t}} \approx 0.2 - 1.8$ mN and $I_{\mathrm{sp}} \approx 60 - 90$ s. These experimental results were also in agreement with numerical simulation using electromagnetic module and two-temperature fluid module. The thrust performance improved by 10 – 15 % compared with our previous work [70] using 4-GHz microwaves, corresponding to better plasma characteristics (higher gas temperature and electron density). Thus, 11-GHz microwaves were confirmed to bring potentialities of supporting more compact design and higher performance at the same time.

Chapter 5

Conclusions

5.1 Concluding remarks

In this study, a microarcjet thruster using microwave-excited microplasma is investigated numerically and experimentally, to improve thrust performance. This thruster consists of a microplasma source and a micronozzle. The microplasma source was made of a dielectric chamber 1.5 – 2.0 mm in diameter and 3.6 – 10 mm long covered with a metal grounded, having a metal rod antenna on axis covered with a dielectric envelope. Propellant gas of Ar, He, H_2 and microwaves are injected into the chamber, generating a plasma discharge. The gas is heated by the discharge up to $\sim 600 - 1000$ K, and aerodynamically accelerated through the micronozzle, to finally produce the thrust of $\sim 0.1 - 1$ mN and specific impulse of $\sim 70 - 450$ s.

In Chap. 2, a micro plasma thruster of electrothermal type using azimuthally symmetric microwave-excited microplasmas, which consisted of a microplasma source and micronozzle, has been investigated. The feed or propellant gas employed was Ar at pressures of 10 – 50 kPa with flow rates of 10 – 70 sccm, and the surface wave-excited plasmas were established by 4.0 GHz microwaves at input powers of $P_{\rm in} \leq 6$ W. Numerical analysis was made for the plasma and flow properties in the microplasma source and micronozzle by developing a self-consistent numerical model, where a two-temperature fluid model was applied to the entire region through the plasma source to nozzle. Numerical results re-

vealed the spatially nonuniform distribution of plasma and flow parameters in the microplasma source: the absorbed power density, plasma density, and gas temperature are maximum at around the end of the microwave antenna or dielectric envelope (just upstream of the inlet of the micronozzle), which is preferred for a thruster of electrothermal type using the converging-diverging nozzle. Optical emission spectroscopy was employed with a small amount of additive gases of H_2 and N_2, to measure the plasma electron density and gas temperature in the microplasma source at around the end of the antenna or dielectric envelope. The electron density was in the range $n_e \approx (3-12)\times 10^{19}$ m^{-3} and the gas or rotational temperature was in the range $T_g \approx T_{rot} \approx 700-1000$ K. The thrust performance was also measured by a micro thrust stand with a combination of target and pendulum methods, giving a thrust in the range $F_t \approx 0.2-1.4$ mN, a specific impulse in the range $I_{sp} \approx 50-80$ s, and a thrust efficiency in the range $\eta_t \approx 2-12$ %. The thrust performance was found to increase with the discharge on and with increasing microwave power. These experimental results were consistent with those of numerical analysis. The micro plasma thruster presently developed would be applicable to attitude-control and station-keeping maneuver for microspacecraft of < 10 kg.

In Chap. 3, a microplasma thruster has been investigated with feed or propellant gases of He and H_2 to achieve higher specific impulse. The plasmas were established by 4.0-GHz microwaves at powers of $P_{in} \leq 6$ W, with the source pressure in the range 2 – 13 kPa at flow rates of 5 – 70 sccm. The microplasma generation, micronozzle flow, and thrust performance with He was numerically analyzed by using a previously constructed model detailed in Chap. 2. The numerical results indicated that in the micronozzle, viscous boundary layers next to the nozzle walls impede the flow expansion, especially at reduced flow rates, where the supersonic flow is heavily decelerated to subsonic downstream along the axis in the diverging portion of the nozzle. In experiments, the plasma electron density and gas temperature in the microplasma source were measured by optical emission spectroscopy. In the case of He propellant, the electron density

was in the range $n_e \approx (2-5) \times 10^{19}$ m^{-3} and the gas temperature was in the range $T_g \approx T_{rot} \approx 600-700$ K. The thrust performance was also measured, giving a thrust in the range $F_t \approx 0.04-0.51$ mN, a specific impulse in the range $I_{sp} \approx 150-270$ s, and a thrust efficiency in the range $\eta_t \approx 2-12\%$. Similar plasma characteristics and thrust performance were obtained with H_2 propellant, where the specific impulse I_{sp} (≤ 450 s) was more than 1.5 times higher than that with He, owing to a difference in mass between He and H_2. A comparison with previous numerical and experimental studies with Ar propellant in Chap. 2 indicated that the plasma electron density n_e was about three times lower in He and H_2 than in Ar; however, the gas temperature $T_g \approx T_{rot}$ was remained a little lower in He and H_2, and the specific impulse I_{sp} was found to be enhanced by about 3 – 5 times with light-mass He and H_2, as has been known for large-scale propulsion systems. Moreover, the axial flow velocity u calculated was more than two times larger in He than that in Ar in the microplasma source as well as micronozzle regions owing to the higher sonic speed a of He, because u is governed primarily by the choking ($Ma = u/a = 1$) at the nozzle throat. Thus, in contrast to general assumptions, it follows that in the microplasma thruster of electrothermal type, the high surface-to-volume ratio of microplasma sources and the high diffusivity and thermal conductivity of light-mass propellants do not lead to a deterioration of the thrust performance. This is attributed primarily to a more significant thermal energy gain due to elastic collisions between electrons and heavy particles in He and H_2 as compared to that in Ar, which tends to offset a more significant thermal energy loss due to the high diffusivity and thermal conductivity of He and H_2 in the microplasma source of high surface-to-volume ratios.

In Chap. 4, an 11-GHz (X-band) microwave-excited microplasma source has been employed instead of 4.0-GHz (S-band) in previous works, and an investigation of the plasma characteristics and the thrust performance has been carried out, for the potentialities of more compact design and higher performance. Since X-band microwave-excited microplasma is a novel frontier for plasma science and technology field, we have focused on the fundamental characteristics of X-

band microplasma, as well as an application to microplasma thruster. The propellant gas employed was Ar at pressures of 10 – 50 kPa with flow rates of 10 – 70 sccm, and the surface wave-excited plasmas were established by 11 GHz microwaves at input powers of $P_{\mathrm{in}} \leq 6$ W. From the results of optical emission spectroscopy (OES), the Ar II (Ar^+) spectral lines were observed unlike the S-band microplasma, indicating the presence of electrons that have high enough energy to excite Ar^+ ions. The gas (heavy particle) temperature T_{g} and electron density n_{e} were measured by optical emission spectroscopy (OES), indicating that $n_{\mathrm{e}} \approx (4-14)\times 10^{19}$ m^{-3} and $T_{\mathrm{g}} \approx 700-1100$ K. The thrust F_{t} and specific impulse I_{sp} were measured by target-type thrust stand, indicating that $F_{\mathrm{t}} \approx 0.2-1.8$ mN and $I_{\mathrm{sp}} \approx 60-90$ s. These experimental results were also in agreement with numerical simulation using electromagnetic module and two-temperature fluid module. The thrust performance improved by 10 – 15 % compared with the results using 4-GHz microwaves, corresponding to better plasma characteristics (higher gas temperature and electron density). Thus, 11-GHz microwaves were confirmed to bring potentialities of supporting more compact design and higher performance at the same time.

5.2 Future work

Throughout this thesis, we have focused on a microarcjet, that is a purely electrothermal type microthruster. The most significant advantage is simple structure, because of no need of neutralizers or magnets. However, it is found that this could be a serious limitation of thrust performance, especially in small-scale. The viscous loss of micronozzle will become more notable with the reduction of throat diameter, because the thickness of boundary layer remains almost unchanged with the nozzle dimensions. With using external electric and magnetic field, there will be some room for more performance improvement brought by ion beam extraction and magnetic plasma confinement. Moreover, the present microplasma thruster has some difficulties in operating with molecular propellants, such as H_2 and N_2.

Molecular propellants will be good candidates when stable plasma generation are established, especially in the aspect of propellant storage.

From the viewpoint of plasma physics, X-band microwave-excited microplasma is an interesting subject of research. In Chap. 4, we have revealed the simple difference in optical emission between X-band and S-band microplasma. Since the microplasma source in this work is designed for a microthruster, it is not very suitable for plasma diagnostics to investigate the fundamental characteristics. There will be a lot of novel finding through a plasma diagnostics of X-band microplasma.

Bibliography

[1] E. Y. Robinson, H. Helvajian, and S. W. Janson, Aerospace America **Oct**, 38 (1996).

[2] H. Helvajian and S. W. Janson, *Microengineering Aerospace Systems*, edited by H. Helvajian (AIAA, Reston, 1999), Chap. 2.

[3] C. Sabol, R. Burns, and C. A. McLaughlin, *J. Spacecraft Rockets* **38** (2001) 270.

[4] S. Nakasuka, N. Sako, H. Sahara, Y. Nakamura, T. Eishima, and M. Komatsu, *Acta Astronaut.* **66** (2010) 1099.

[5] M. Nohmi, T. Yamamoto, A. Andatsu, Y. Takagi, Y. Nishikawa, T. Kaneko, and D. Kunitomi, *Trans. Jpn. Soc. Aero. Space Sci., Space Technol. Jpn.* **7**(ists26), Tu_7.

[6] K. Yoshida, Y. Takahashi, Y. Sakamoto, E. Ujiie, K. Takiuchi, Y. Nakazato, T. Sawakami, T. Sakanoi, Y. Kasaba, S. Kondo, K. Yamashita, S. Ueda, T. Takashima, K. Nakazawa, T. Mitani, T. Enoto, M. Sato, U. Inan, I. Linscott, F. Bruhn, and Y. Masumoto, *Proc. The 27th International Symposium on Space Technology and Science*, Tsukuba, Japan, 2009, Paper 2009-m-05.

[7] M. Nishio and Kagoshima Satellite Development Group, 第 *54* 回宇宙科学技術連合講演会講演集 *(in Japanese)*, Shizuoka, Japan, 2010, Paper JSASS-2010-4056.

[8] K. Ono, M. Ueda, T. Yamada, K. Kaneko, S. Uratsuji, T. Miura, A. Oniduka, Y. Maeda, K. Myowa, H. Yoshiga, T. Monai, S. Kodama, and S. Kuroki, 第*54*回宇宙科学技術連合講演会講演集*(in Japanese)*, Shizuoka, Japan, 2010, JSASS-2010-4175.

[9] T. Totani, UNITEC-1 Developers, M. Wakita, and H. Nagata, 第 *54* 回宇宙科学技術連合講演会講演集 *(in Japanese)*, Shizuoka, Japan, 2010, Paper JSASS-2010-4244.

[10] H. Takagi, T. Yamamoto, Y. Ishii, and H. Tahara, *Proc. The 27th International Symposium on Space Technology and Science*, Tsukuba, Japan, 2009, Paper 2009-b-16.

[11] R. G. Jahn, *Physics of Electric Propulsion* (McGraw-Hill, New York, 1968), Chaps. 6–9.

[12] J. Mueller, *Micropropulsion for Small Spacecraft*, edited by M. M. Micci and A. D. Ketsdever (AIAA, Reston, 2000), Chap. 3.

[13] J. R. Wilson, Aerospace America **Feb**, 34 (2003).

[14] M. Tajmar, *Advanced Space Propulsion Systems* (Springer, Vienna, 2004), Chap. 2.

[15] J. Sethian, *MEMS and Microstructures in Aerospace Applications*, edited by R. Osiander, M. A. G. Darrin and J. L. Champion (CRC Press, Boca Raton, 2005), Chap. 11.

[16] H. Horisawa, K. Onodera, T. Noda and I. Kimura, Vacuum **80**, 1244 (2006).

[17] H. Horisawa, F. Sawada, S. Hagiwara, and I. Funaki, Vacuum **85**, 574 (2010).

[18] H. Okamoto and M. Nishida, Trans. Jpn. Soc. Aero. Space Sci. **48**, 187 (2006).

[19] T. Deconinck, S. Mahadevan, and L. L. Raja, IEEE Trans. Plasma Sci. **36**, 1200 (2008).

[20] P. S. Kothnur and L. L. Raja, J. Appl. Phys. **97**, 043305 (2005).

[21] P. S. Kothnur and L. L. Raja, Contrib. Plasma Phys. **47**, 9 (2007).

[22] T. Ito and M. A. Cappelli, Appl. Phys. Lett. **89**, 061501 (2006).

[23] T. Ito, N. Gascon, W. S. Crawford, and M. A. Cappelli, J. Propul. Power **23**, 1068 (2007).

[24] H. Kataharada, Y. Takao, N. Yamamoto, H. Ijiri, and H. Nakashima, Thin Solid Films **506**–**507**, 605 (2006).

[25] N. Yamamoto, S. Kondo, T. Chikaoka, H. Nakashima, and H. Masui, J. Appl. Phys. **102**, 123304 (2007).

[26] N. Yamamoto, K. Tomita, N. Yamasaki, T. Tsuru, T. Ezaki, Y. Kotani, K. Uchino, and H. Nakashima, Plasma Sources Sci. Technol. **19**, 045009 (2010).

[27] H. Koizumi and H. Kuninaka, J. Propul. Power **26**, 601 (2010).

[28] M. A. Kemp and S. D. Kovaleski, J. Appl. Phys. **100**, 113306 (2006).

[29] M. A. Kemp and S. D. Kovaleski, IEEE Trans. Plasma Sci. **36**, 356 (2008).

[30] S. Kitanishi, Y. Takao, K. Eriguchi, and K. Ono, 平成 *22* 年度宇宙輸送シンポジウム講演集 *(in Japanese)*, Sagamihara, Japan, 2011, Paper STEP-2010-052.

[31] A. Dunaevsky, Y. Raitses, and N. J. Fisch, Appl. Phys. Lett. **88**, 251502 (2006).

[32] M. Tajmar, A. Genovese, and W. Steiger, J. Propul. Power **20**, 211 (2004).

[33] S. Castro and R. Bocanegra, Appl. Phys. Lett. **88**, 123105 (2006).

[34] J. Schein, N. Qi, R. Binder, M. Krishnan, J. K. Ziemer, J. E. Polk, and A. Anders, Rev. Sci. Instrum. **73**, 925 (2002).

[35] T. Moeller and Y. K. Chang, Aerospace Sci. and Technol. **11**, 481 (2007).

[36] M. Keidar, I. D. Boyd, J. Luke, and C. Phipps, J. Appl. Phys. **96**, 49 (2004).

[37] J. Aoyagi,M. Mukai, Y. Kamishima, T. Sasaki, K. Shintani, H. Takegahara, T. Wakizono, and M. Sugiki, Vacuum **83**, 72 (2008).

[38] E. L. Antonsen, R. L. Burton, G. A. Reed, and G. G. Spanjers, Rev. Sci. Instrum. **77**, 103107 (2006).

[39] S. C. Kim, J. Spacecraft Rockets **31**, 259 (1994).

[40] A. D. Ketsdever, R. H. Lee, and T. C. Lilly, J. Micromech. Microeng. **15**, 2254 (2005).

[41] Z. Ahmed, S. F. Giemelshein, and A. D. Ketsdever, J. Propul. Power **22**, 749 (2006).

[42] Y. Takao and K. Ono, Plasma Sources Sci. Technol. **15**, 211 (2006).

[43] Y. Takao, K. Ono, K. Takahashi, and Y. Setsuhara, Thin Solid Films **506**–**507**, 592 (2006).

[44] Y. Takao, K. Ono, K. Takahashi, and K. Eriguchi, Jpn. J. Appl. Phys. **45**, 8235 (2006).

[45] Y. Takao, K. Eriguchi, and K. Ono, J. Appl. Phys. **101**, 123307 (2007).

[46] T. Takahashi, Y. Takao, K. Eriguchi, and K. Ono, *Proc. 30th International Electric Propulsion Conference, Florence, Italy, Sep. 2007*, Paper IEPC-2007-29.

[47] Y. Takao, T. Takahashi, K. Eriguchi, and K. Ono, Pure Appl. Chem. **80**, 2013 (2008).

[48] T. Takahashi, Y. Takao, K. Eriguchi, and K. Ono, J. Phys. D: Appl. Phys. **41**, 194005 (2008).

[49] M. Tuda and K. Ono, J. Vac. Sci. Technol. A **16**, 2832 (1998).

[50] M. Tuda, K. Ono, H. Ootera, M. Tsuchihashi, M. Hanazaki, and T. Komemura, J. Vac. Sci. Technol. A **18**, 840 (2000).

[51] H. Kousaka and K. Ono, Jpn. J. Appl. Phys. **41**, 2199 (2002).

[52] H. Kousaka and K. Ono, Plasma Sources Sci. Technol. **12**, 273 (2003).

[53] J. T. Gudmundsson and E. G. Thorsteinsson, Plasma Sources Sci. Technol. **16**, 399 (2007).

[54] M. A. Lieberman and A. J. Lichtenberg, *Principles of Plasma Discharges and Materials Processing, 2nd Edition* (Wiley, New York, 2005), Chap. 3.

[55] K. Tachibana, Phys. Rev. A **34**, 1007 (1986).

[56] F. Kannari, M. Obara, and T. Fujioka, J. Appl. Phys. **57**, 4309 (1985).

[57] L. M. Biberman, V. S. Vorob'ev, and I. T. Yakubov, *Kinetics of Nonequilibrium Low-Temperature Plasmas* (Consultants Bureau, New York, 1987), Chap. 2.

[58] S. Yoon and A. Jameson, AIAA J. **26**, 1025 (1988).

[59] D. R. Miller, *Atomic and Molecular Beam Methods Volume 1*, edited by D. Scoles, D. Bassi, U. Buck, and D. Laine (Oxford Univ. Press, New York, 1988), Chap. 2.

[60] H. W. Liepmann and A. Roshko, *Elements of Gas Dynamics* (Wiley, New York, 1957), Chap. 2.

[61] G. P. Sutton and O. Biblarz, *Rocket Propulsion Elements* (Wiley, New York, 2001), Chap. 3.

[62] H. R. Griem, *Plasma Spectroscopy* (McGraw-Hill, New York, 1964), Chap. 4.

[63] H. R. Griem, *Spectral Line Broadening by Plasmas* (Academic Press, New York, 1974), Chap. III and Appendix I.

[64] H. R. Griem, *Principles of Plasma Spectroscopy* (Cambridge University Press, Cambridge, 1997), Chaps. 4 and 10.

[65] Q. Wang, I. Koleva, Y. M. Donnelly, and D. J. Economou, J. Phys. D: Appl. Phys. **38**, 1690 (2005).

[66] J. Mitroy and M. W. Bromley, Phys. Rev. A **68**, 5201 (2003).

[67] M. A. Gigosos and V. Gardenoso, J. Phys. B: At. Mol. Opt. Phys. **29**, 4795 (1996).

[68] J. M. Luque, M. D. Calzada, and M. Saez, J. Phys. B: At. Mol. Opt. Phys. **36**, 1573 (2003).

[69] G. Wirsig, *Space Propulsion Analysis and Design*, edited by R. W. Humble, G. N. Henry, and W. J. Larson (McGraw-Hill, New York, 1995), Chap. 3.

[70] T. Takahashi, Y. Takao, K. Eriguchi, and K. Ono, Phys. Plasmas **16**, 083505 (2009).

[71] M. A. Kurtz, T. Gölz, H. Habiger, F. Hammer, H, Kurtz, M. Riehle, and C. Sleziona, J. Propul. Power **14**, 764 (1998).

[72] W. A. Hargus Jr., J. H. Schilling, Q. E. Walker, and M. A. Cappelli, J. Spacecraft and Rockets **41**, 1016 (2004).

[73] K. Kinefuchi, I. Funaki, and K. Toki, J. Propul. Power **22**, 1085 (2006).

[74] NIST Standard Database 134, "*Database of the Thermophysical Properties of Gases Used in the Semiconductor Industry*" (http://www.nist.gov/pml/process/fluid/srd_134_gasesindex.cfm)

[75] G. A. Bird, *Molecular Gas Dynamics and the Direct Simulation of Gas Flows* (Clarendon Press, Oxford, UK, 1994), Chap. 3, p. 69.

[76] J. Jonkers, L. J. M. Selen, J. A. M. van der Mullen, E. A. H. Timmermans, and D. C. Schram, Plasma Sources Sci. Technol. **6**, 533 (1997).

[77] R. W. Crompton, M. T. Elford, and A. G. Robertson, Aust. J. Phys. **23**, 667 (1970).

[78] Y. Sakai, Appl. Surf. Sci. **192**, 327 (2002).

[79] J. W. Shon and M. J. Kushner, J. Appl. Phys. **75**, 1883 (1994).

[80] X. Yuan and L. L. Raja, IEEE Trans. Plasma Sci. **31**, 495 (2003).

[81] T. Belmonte, R. P. Cardoso, G. Henrion, and F. Kosior, J. Phys. D: Appl. Phys. **40**, 7343 (2007).

[82] D. Ton-That, S. T. Manson, and M. R. Flannery, J. Phys. B: Atom. Mol. Phys. **4**, 621 (1977).

[83] D. Ton-That and M. R. Flannery, Phys. Rev. A **15**, 517 (1977).

[84] D. Margreiter, H. Deutsch, and T. D. Mark, Contrib. Plasma Phys. **30**, 487 (1990).

[85] K. H. Becker, K. H. Schoenbach, and J. G. Eden, J. Phys. D: Appl. Phys. **39**, R55 (2006).

[86] B. N. Sismanoglu, K. G. Grigorov, R. A. Santos, R. Caetano, M. V. O. Rezende, Y. D. Hoyer, and V. W. Ribas, Eur. Phys. J. D **60**, 479 (2010).

[87] L. G. Meng, Z. J. Lin, J. P. Xing, Z. H. Liang, and C. L. Liu, Eur. Phys. J. D **60**, 575 (2010).

[88] B. Hrycak, M. Jasiński, and J. Mizeraczyk, Eur. Phys. J. D **60**, 609 (2010).

[89] J. Gregório, L. L. Alves, O. Leroy, P. Leprince, and C. Boisse-Laporte, Eur. Phys. J. D **60**, 627 (2010).

[90] O. Sakai, T. Naito, T. Shimomura, and K. Tachibana, Thin Solid Films **518**, 3444 (2010).

[91] N. Miura and J. Hopwood, J. Appl. Phys. **109**, 013304 (2011).

[92] Y. Shimizu, K. Kawaguchi, T. Sasaki, and N. Koshizaki, Appl. Phys. Lett. **94**, 191504 (2009).

[93] D. Mariotti and R. M. Sankaran, J. Phys. D: Appl. Phys. **43**, 323001 (2010).

[94] R. Pothiraja, N. Bibinov, and P. Awakowicz, J. Phys. D: Appl. Phys. **43**, 495201 (2010).

[95] Y. Takao, N. Kusaba, K. Eriguchi, and K. Ono, J. Appl. Phys. **108**, 093309 (2010).

[96] M. Schlapp, R. Trassl, E. Salzborn, R. W. McCullough, T. K. McLaughlin, and H. B. Gilbody, Nucl. Instrum. Methods Phys. Res., Sect. B **98**, 525 (1995).

[97] P. Grübling, J. Hollandt, and G. Ulm, Nucl. Instrum. Methods Phys. Res., Sect. A **437**, 152 (1999).

[98] R. Yanagi and I. Kimura, J. Spacecr. Rockets **19**, 246 (1982).

[99] A. R. Striganov and N. S. Sventitskii, *Tables of Spectral Lines of Neutral and Ionized Atoms* (IFI/Plenum, New York, 1968).

List of publications

Journals

1. Y. Takao, T. Takahashi, K. Eriguchi, and K. Ono, "Microplasma thruster for ultra-small satellites: Plasma chemical and aerodynamical aspects", Pure Appl. Chem. **80**, 2013 [11 pages] (2008).

2. T. Takahashi, Y. Takao, K. Eriguchi, and K. Ono, "Microwave-excited microplasma thruster: a numerical and experimental study of the plasma generation and micronozzle flow", J. Phys. D: Appl. Phys. **41**, 194005 [6 pages] (2008).

3. T. Takahashi, Y. Takao, K. Eriguchi, and K. Ono, "Numerical and experimental study of microwave-excited microplasma and micronozzle flow for a microplasma thruster", Phys. Plasmas **16**, 083505 [14 pages] (2009).

4. T. Takahashi, Y. Ichida, Y. Takao, K. Eriguchi, and K. Ono, "Numerical simulation of a microwave-excited microplasma thruster", Trans. Japan Soc. Aero. Space Sci., Space Technol. Japan **7** ists26 Pb_135 [6 pages] (2009).

5. T. Takahashi, Y. Takao, Y. Ichida, K. Eriguchi, and K. Ono, "Microwave-excited microplasma thruster with helium and hydrogen propellants", Phys. Plasmas **18**, 063505 [12 pages] (2011).

6. T. Takahashi, Y. Takao, K. Eriguchi, and K. Ono, "X-band microwave-excited microplasma: Fundamentals and application to electrothermal mi-

croplasma thruster", J. Appl. Phys. (To be submitted).

International conferences

1. T. Takahashi, Y. Takao, K. Eriguchi, and K. Ono, "Numerical analysis and optical diagnostics of a microwave-excited plasma source for microthrusters", Proc. 18th International Symposium on Plasma Chemistry (ISPC-18), Kyoto, Japan, 2007, Paper 28P-123.

2. T. Takahashi, Y. Takao, K. Eriguchi, and K. Ono, "Numerical Analysis and Experiments of a Microwave-excited Microplasma Thruster", Proc. 30th International Electric Propulsion Conference (IEPC 2007), Florence, Italy, 2007, Paper IEPC-2007-29.

3. T. Takahashi, Y. Ichida, Y. Takao, K. Eriguchi, and K. Ono, "Numerical Simulation of a Microwave-Excited Microplasma Thruster", Proc. 26th International Symposium on Space Technology and Science (ISTS 2008), Hamamatsu, Japan, 2008, Paper 2008-b-17.

4. Y. Ichida, T. Takahashi, Y. Takao, K. Eriguchi, and K. Ono, "Analysis of Microwave-excited Plasma Thrusters with Hydrogen Propellant", Proc. 26th International Symposium on Space Technology and Science (ISTS 2008), Hamamatsu, Japan, 2008, Paper 2008-b-20.

5. T. Takahashi, Y. Ichida, S. Kitanishi, K. Eriguchi, and K. Ono, "Microwave-Excited Microplasma Thruster: Design of Improved Model Aiming for Flight", Proc. 27th International Symposium on Space Technology and Science (ISTS 2009), Tsukuba, Japan, 2009, Paper 2009-b-21.

6. T. Takahashi, S. Kitanishi, Y. Takao, K. Eriguchi, and K. Ono, "Microwave-Excited Microplasma Thruster: Design Improvement for Implemantation to Satellite", 31st International Electric Propulsion Conference (IEPC 2009), Ann Arbor, USA, 2009, Paper IEPC-2009-190.

7. T. Takahashi, Y. Takao, K. Eriguchi, and K. Ono, "Numerical Simulation of Microwave-Excited Microplasma Thruster with Helium Propellant", 61st International Astronautical Congress (IAC), Prague, Czech Republic, 2010, Paper IAC-10.C4.4.13.

8. T. Takahashi, Y. Takao, K. Eriguchi, and K. Ono, "11-GHz Microwave-Excited Microplasma Source for Electrothermal Thruster", 63rd Gaseous Electronics Conference (GEC) and 7th International Conference on Reactive Plasmas (ICRP), Paris, France, 2010, Paper DTP.00228. Bull. Am. Phys. Soc. 55(7), 2010, p. 97.